



**NAVAL
POSTGRADUATE
SCHOOL**

MONTEREY, CALIFORNIA

DISSERTATION

**OBSERVATIONS AND MODELING OF UPPER OCEAN
HYDROGRAPHY IN THE WESTERN ARCTIC WITH
IMPLICATIONS FOR ACOUSTIC PROPAGATION**

by

Dominic F. DiMaggio

December 2016

Dissertation Supervisors:

Wieslaw Maslowski
John Colosi

Approved for public release. Distribution is unlimited.

THIS PAGE INTENTIONALLY LEFT BLANK

| REPORT DOCUMENTATION PAGE | | | Form Approved OMB No. 0704-0188 |
|--|--|---|-------------------------------------|
| <p>Public reporting burden for this collection of information is estimated to average 1 hour per response, including the time for reviewing instruction, searching existing data sources, gathering and maintaining the data needed, and completing and reviewing the collection of information. Send comments regarding this burden estimate or any other aspect of this collection of information, including suggestions for reducing this burden, to Washington Headquarters Services, Directorate for Information Operations and Reports, 1215 Jefferson Davis Highway, Suite 1204, Arlington, VA 22202-4302, and to the Office of Management and Budget, Paperwork Reduction Project (0704-0188) Washington, DC 20503.</p> | | | |
| 1. AGENCY USE ONLY (Leave blank) | 2. REPORT DATE December 2016 | 3. REPORT TYPE AND DATES COVERED Dissertation | |
| 4. TITLE AND SUBTITLE OBSERVATIONS AND MODELING OF UPPER OCEAN HYDROGRAPHY IN THE WESTERN ARCTIC WITH IMPLICATIONS FOR ACOUSTIC PROPAGATION | | 5. FUNDING NUMBERS | |
| 6. AUTHOR(S) Dominic F. DiMaggio | | | |
| 7. PERFORMING ORGANIZATION NAME(S) AND ADDRESS(ES) Naval Postgraduate School Monterey, CA 93943-5000 | | 8. PERFORMING ORGANIZATION REPORT NUMBER | |
| 9. SPONSORING /MONITORING AGENCY NAME(S) AND ADDRESS(ES) N/A | | 10. SPONSORING / MONITORING AGENCY REPORT NUMBER | |
| 11. SUPPLEMENTARY NOTES The views expressed in this thesis are those of the author and do not reflect the official policy or position of the Department of Defense or the U.S. Government. IRB number <u>N/A</u> . | | | |
| 12a. DISTRIBUTION / AVAILABILITY STATEMENT Approved for public release. Distribution is unlimited. | | 12b. DISTRIBUTION CODE | |
| <p>13. ABSTRACT (maximum 200 words)</p> <p>Observational and modeling studies are conducted to explore the changing physical environment of the western Arctic Ocean and its significance to upper-ocean hydrography and acoustic energy propagation. In-situ observations of temperature and salinity were made as part of the Canada Basin Acoustic Propagation Experiment (CANAPE) pilot study in summer 2015. Sound-speed fluctuations due to internal waves and spice were analyzed to describe spatio-temporal variability. Internal-wave frequency spectra show a spectral slope lower than the Garrett-Munk (GM) model, and the energy level is 4% of the standard GM value. Frequency spectra of spice show a form similar to the internal-wave spectra but with a steeper spectral slope. Several global climate models were evaluated against historical and recent hydrographic observations and found to inadequately represent key upper-ocean hydrographic features. The Regional Arctic System Model (RASM) was used to investigate sensitivity of the simulated upper ocean to various configurations and showed that sub-grid scale brine rejection parameterization, appropriately tuned surface momentum coupling, and increased vertical and horizontal resolution improved model simulation. In both observational and model data sets, a near-surface sound channel is present, the significance and variability of which warrant further in-situ investigations and model improvements.</p> | | | |
| 14. SUBJECT TERMS Arctic Ocean, oceanography, acoustics, Canada Basin, climate system model | | | 15. NUMBER OF PAGES 143 |
| | | | 16. PRICE CODE |
| 17. SECURITY CLASSIFICATION OF REPORT Unclassified | 18. SECURITY CLASSIFICATION OF THIS PAGE Unclassified | 19. SECURITY CLASSIFICATION OF ABSTRACT Unclassified | 20. LIMITATION OF ABSTRACT UU |

THIS PAGE INTENTIONALLY LEFT BLANK

Approved for public release. Distribution is unlimited.

**OBSERVATIONS AND MODELING OF UPPER OCEAN
HYDROGRAPHY IN THE WESTERN ARCTIC WITH IMPLICATIONS
FOR ACOUSTIC PROPAGATION**

Dominic F. DiMaggio
Lieutenant Commander, United States Navy
B.S., University of Arkansas, 2004
M.S., Naval Postgraduate School, 2012

Submitted in partial fulfillment of the
requirements for the degree of

DOCTOR OF PHILOSOPHY IN PHYSICAL OCEANOGRAPHY

from the

NAVAL POSTGRADUATE SCHOOL
December 2016

Approved by:

Wieslaw Maslowski
Research Professor of Oceanography
Dissertation Co-Supervisor

John Colosi
Professor of Oceanography
Dissertation Co-Supervisor

Andrew Roberts
Research Assistant Professor of Oceanography

John Joseph
Research Associate of Oceanography

Peter Guest
Research Professor of Meteorology

Peter Worcester
Research Oceanographer Emeritus
Scripps Institution of Oceanography

Approved by: Peter Chu, Chair, Department of Oceanography

Approved by: Douglas Moses, Vice Provost of Academic Affairs

THIS PAGE INTENTIONALLY LEFT BLANK

ABSTRACT

Observational and modeling studies are conducted to explore the changing physical environment of the western Arctic Ocean and its significance to upper-ocean hydrography and acoustic energy propagation. *In-situ* observations of temperature and salinity were made as part of the Canada Basin Acoustic Propagation Experiment (CANAPE) pilot study in summer 2015. Sound-speed fluctuations due to internal waves and spice were analyzed to describe spatio-temporal variability. Internal-wave frequency spectra show a spectral slope lower than the Garrett-Munk (GM) model, and the energy level is 4% of the standard GM value. Frequency spectra of spice show a form similar to the internal-wave spectra but with a steeper spectral slope. Several global climate models were evaluated against historical and recent hydrographic observations and found to inadequately represent key upper-ocean hydrographic features. The Regional Arctic System Model (RASM) was used to investigate sensitivity of the simulated upper ocean to various configurations and showed that sub-grid scale brine rejection parameterization, appropriately tuned surface momentum coupling, and increased vertical and horizontal resolution improved model simulation. In both observational and model data sets, a near-surface sound channel is present, the significance and variability of which warrant further *in-situ* investigations and model improvements.

THIS PAGE INTENTIONALLY LEFT BLANK

TABLE OF CONTENTS

| | | |
|-------------|---|-----------|
| I. | INTRODUCTION..... | 1 |
| A. | MOTIVATION | 1 |
| 1. | Arctic Sea Ice..... | 1 |
| 2. | Human Activity in the Arctic..... | 4 |
| 3. | U.S. Arctic Strategy | 8 |
| B. | RESEARCH GOALS | 9 |
| C. | STRUCTURE OF THIS DISSERTATION..... | 10 |
| D. | ARCTIC PHYSICAL OCEANOGRAPHY AND ACOUSTICS | 10 |
| 1. | Physical Oceanography of the Arctic..... | 10 |
| 2. | Underwater Propagation of Sound in the Arctic Ocean | 17 |
| II. | OBSERVATIONS OF THERMOHALINE SOUND-SPEED STRUCTURE INDUCED BY INTERNAL WAVES AND SPICE IN THE SUMMER 2015 CANADA BASIN MARGINAL ICE ZONE | 23 |
| A. | INTRODUCTION..... | 23 |
| B. | THE EXPERIMENT | 26 |
| 1. | Observations..... | 26 |
| 2. | Displacement and Spice Analysis | 33 |
| C. | FREQUENCY SPECTRA AND ANALYSIS OF VARIANCE..... | 38 |
| 1. | Internal Waves | 39 |
| 2. | Spice | 42 |
| D. | VERTICAL SCALES OF VARIABILITY | 45 |
| 1. | Internal Waves | 45 |
| 2. | Spice | 47 |
| E. | SUMMARY AND CONCLUSIONS | 48 |
| F. | ACKNOWLEDGMENTS | 49 |
| III. | EVALUATION AND SENSITIVITY OF CLIMATE MODEL SKILL AT REPRESENTING UPPER ARCTIC OCEAN HYDROGRAPHY | 51 |
| A. | INTRODUCTION..... | 51 |
| B. | MODEL DESCRIPTIONS | 54 |
| 1. | Climate Models..... | 54 |
| 2. | Regional Arctic System Model Experiments | 55 |
| 3. | Observational Data for Comparison: PHC and ITP | 57 |
| 4. | Region of Study | 58 |
| C. | CLIMATE MODEL SKILL | 58 |
| 1. | Profiles | 58 |

| | | |
|--|---|------------|
| 2. | T-S Diagrams..... | 62 |
| 3. | Bulk Property Time Series..... | 63 |
| 4. | Taylor Diagrams and Skill Scores..... | 68 |
| D. | SENSITIVITY EXPERIMENTS WITH RASM | 75 |
| 1. | Profiles | 76 |
| 2. | T-S Diagrams..... | 86 |
| 3. | Bulk Property Time Series..... | 88 |
| 4. | Taylor Diagrams and Skill Scores..... | 91 |
| E. | SUMMARY AND CONCLUSIONS | 94 |
| F. | ACKNOWLEDGEMENTS | 95 |
| IV. | CONCLUSIONS | 97 |
| A. | SUMMARY OF RESEARCH | 97 |
| B. | IMPLICATIONS FOR ACOUSTIC PROPAGATION..... | 98 |
| C. | RECOMMENDATIONS..... | 106 |
| LIST OF REFERENCES | | 107 |
| INITIAL DISTRIBUTION LIST | | 121 |

LIST OF FIGURES

| | | |
|-------------|---|----|
| Figure 1.1. | Arctic Sea Ice Concentrations. Adapted from Cryosphere Today 2016..... | 2 |
| Figure 1.2. | Ice Age from 1985 to 2015. Source: Perovich et al. 2015..... | 3 |
| Figure 1.3. | Anticipated Arctic Transit Routes with Consensus-Projected Sea Ice Extent Minima. Source: Task Force Climate Change 2014. | 5 |
| Figure 1.4. | Maritime Jurisdiction and Boundaries in the Arctic Region. Source: IBRU, Durham University 2016. | 7 |
| Figure 1.5. | Annotated Map of Arctic Bathymetry and Topography Region. Adapted from Jakobsson et al. 2012..... | 11 |
| Figure 1.6. | Schematic Diagram of General Oceanic Circulation in and Around the Arctic Ocean. Source: WHOI 2014. | 13 |
| Figure 1.7. | Schematic Representation of the General Layers in the Arctic Ocean in Cross Section from the Bering Strait to the Fram Strait. Adapted from DiMaggio 2012. | 14 |
| Figure 1.8. | Schematic Diagram of a Generic Deep-Ocean Temperature Profile ($T(z)$) and Resulting Sound Speed Profile ($c(z)$)..... | 18 |
| Figure 1.9. | Typical Acoustic Conditions in the Arctic. Source: Mikhalevsky 2001..... | 19 |
| Figure 2.1. | Region of the CANAPE Pilot Study. Adapted from University of Illinois 2016. | 24 |
| Figure 2.2. | Depth-Time Series of Potential Density and Temperature. | 29 |
| Figure 2.3. | Mean Profiles of Temperature, Salinity, Sound Speed, Buoyancy Frequency, Potential Density, and Potential Sound Speed Gradient. | 31 |
| Figure 2.4. | Potential Temperature Plotted as a Function of Salinity as Measured by the DVLA Mooring (left) and Ship CTDs (right)..... | 33 |
| Figure 2.5. | Depth of 45 Tracked Isopycnals as a Function of Time in the Upper 550 m at the DVLA Mooring..... | 34 |
| Figure 2.6. | Root Mean Square Error in Tracking Isopycnal Density (left) and Depth (right)..... | 37 |

| | | |
|--------------|---|----|
| Figure 2.7. | Depth-Time Series of Spicy Isopycnal Sound Speed Anomalies..... | 38 |
| Figure 2.8. | Frequency Spectra of Displacement Averaged in Three Depth Bands..... | 40 |
| Figure 2.9. | RMS Displacement of Isopycnals Versus Depth. Sound Speed Variability and Spice..... | 41 |
| Figure 2.10. | Root Mean Square Sound Speed Fluctuations Versus Depth..... | 43 |
| Figure 2.11. | Frequency Spectra of Sound Speed Fluctuations along Isopycnals (Spice) Averaged Over Three Depth Bands. | 44 |
| Figure 2.12. | Normalized Covariance Matrix for the Internal Wave Displacements (Top), and Depth-Averaged Correlation Function as a Function of WKB Depth Lag (Bottom)..... | 46 |
| Figure 2.13. | Vertical Wavenumber Spectrum..... | 47 |
| Figure 2.14. | Normalized Covariance Matrix for Spicy Sound Speed Fluctuations (Top), and Average Correlation Function as a Function of Depth Lag (Bottom). | 48 |
| Figure 3.1. | Water Mass Structure of the Canada Basin as Characterized by (a) Temperature, (b) Salinity, and (c) Brunt-Väisälä Frequency Profiles. Source: Jackson et al. 2010)..... | 53 |
| Figure 3.2. | RASM Domain (a) and Region of Study (b). | 56 |
| Figure 3.3. | Potential Temperature (Blue) and Salinity (Green) of the Upper 700 m from PHC and Modeled by RASM, CESM, GFDL, HadGEM, and MPI. | 60 |
| Figure 3.4. | Potential Temperature as a Function of Salinity of Water Mass Properties from PHC, RASM, and CMs..... | 63 |
| Figure 3.5. | Mean Annual Cycles of Fifteen Bulk Water Mass Properties from PHC and Modeled by RASM, and CMs..... | 65 |
| Figure 3.6. | Example Taylor Diagrams with Overlaid Contours of Taylor Skill Score. Adapted from Taylor 2001. | 70 |
| Figure 3.7. | RASM and PHC Temperature as a Function of Model Level. | 72 |
| Figure 3.8. | Taylor Diagrams of Upper 300 m Ocean Potential Temperature (a.) and Salinity (b.) from RASM and Four Climate Models..... | 73 |
| Figure 3.9. | Taylor Skill Scores for RASM and CMs Evaluated Against PHC. | 74 |

| | | |
|---------------|---|-----|
| Figure 3.10 | Monthly Regional Mean Profiles of Potential Temperature (Blue) and Salinity (Green) from ITP Observations, PHC Climatology, and Seven RASM Experiments..... | 77 |
| Figure 3.11a. | Evolution of Temperature Profile After Model Initialization for Several RASM Experiments..... | 83 |
| Figure 3.11b. | Evolution of Salinity Profile After Model Initialization for Several RASM Experiments..... | 84 |
| Figure 3.12. | T-S Diagrams of the Upper 700 m as Found in ITP, PHC, and RASM Experiments | 88 |
| Figure 3.13. | Time Series of RASM Experiments Water Mass Properties Compared to ITP Observations Between August 2005 and June 2009..... | 90 |
| Figure 3.14. | Taylor Diagrams For Upper Ocean Potential Temperature (a.) and Salinity (b.) of RASM Experiments Evaluated Against ITPs..... | 92 |
| Figure 3.15. | Skill Scores for RASM Experiments and PHC Evaluated Against ITPs for August 2005 to June 2009. | 94 |
| Figure 4.1a. | Profiles of CANAPE Temperature (top left), Salinity (top middle), and Sound Speed (top right) and Their Standard Deviations (bottom row). | 100 |
| Figure 4.1b. | Profiles of ICEX Temperature (top left), Salinity (top middle), and Sound Speed (top right) and Their Standard Deviations (bottom row)... | 101 |
| Figure 4.2. | Modeled Transmission Loss for a 1000 Hz Acoustic Source at 150 m Depth During CANAPE using CTD Observations..... | 102 |
| Figure 4.3. | Modeled Transmission Loss for a 1000 Hz Acoustic Source at 150 m Depth During CANAPE using RASM output. | 103 |
| Figure 4.4. | Modeled Transmission Loss for a 1000 Hz Acoustic Source at 150 m Depth During ICEX using CTD Observations. | 103 |
| Figure 4.5. | Modeled Transmission Loss for a 1000 Hz Acoustic Source at 150 m Depth During ICEX using RASM Output. | 104 |
| Figure 4.6. | Modeled Transmission Loss for Same RASM Output (CANAPE) as Figure 4.3 but with the Source at 35 m..... | 104 |
| Figure 4.7. | Modeled Transmission Loss for Same RASM Data (ICEX) as Figure 4.5 but with the Source at 75 m. | 105 |

THIS PAGE INTENTIONALLY LEFT BLANK

LIST OF TABLES

| | | |
|------------|---|----|
| Table 2.1. | Oceanographic Instrumentation for the DVLA Mooring with Approximate Depth of Each Instrument..... | 28 |
| Table 2.2. | Observed Isopycnal Statistics for Tracked Isopycnals ¹ | 36 |
| Table 3.1. | Earth System and Global Climate Models Compared in this Study..... | 55 |
| Table 3.2. | RASM Experiments Compared in This Study..... | 57 |

THIS PAGE INTENTIONALLY LEFT BLANK

LIST OF ACRONYMS AND ABBREVIATIONS

| | |
|------------|--|
| AGP | Arctic and Global Prediction |
| ARCSS | Arctic System Science |
| AW | Atlantic Water |
| C | sound speed |
| CANAPE | Canada Basin Acoustic Propagation Experiment |
| CCB | Central Canada Basin |
| CESM | Community Earth System Model |
| CESM-LE | CESM - Large Ensemble |
| CICE | the Los Alamos Sea Ice Model |
| CM | Climate Model |
| CMIP5 | Coupled Model Intercomparison Project, 5 th phase |
| CORE2 | Common Ocean Reference Experiment version 2 |
| cpd | cycles per day |
| cph | cycles per hour |
| CTD | conductivity, temperature, and depth |
| DOD | Department of Defense |
| EEZ | Economic Exclusion Zone |
| ESM | Earth-system model |
| FWC | freshwater content |
| g | gravitational acceleration |
| GCM | global climate model |
| GFDL | Geophysical Fluid Dynamics Laboratory |
| GFDL-CM3 | GFDL Climate Model version 3 |
| HadGEM | Hadley Center Global Environmental Model |
| HadGEM2-CC | HadGEM version 2 - Carbon Cycle |
| HC | heat content |
| HD | halocline depth |
| HPCMP | High Performance Computing Modernization Program |
| IBRU | International Boundaries Research Unit, Durham University |
| ICEX | Ice Exercise |

| | |
|------------|---|
| IPCC | Intergovernmental Panel on Climate Change |
| ITP | Ice-tethered profiler |
| J | Joule |
| JCOMM | Joint World Meteorological Organization-Intergovernmental Oceanographic Commission Technical Commission for Oceanography and Marine Meteorology |
| K | degrees Kelvin |
| kg | kilogram |
| LANL | Los Alamos National Laboratory |
| m | meter |
| MLD | mixed layer depth |
| MPI | Max Plank Institute for Meteorology |
| MPI-ESM-MR | MPI Earth System Model - medium resolution |
| N | Brunt-Väisälä frequency |
| NCAR | National Center for Atmospheric Research |
| NOAA | National Oceanic and Atmospheric Administration |
| NSIDC | National Snow and Ice Data Center |
| NSR | Northern Sea Route |
| NSRIO | Northern Sea Route Information Office |
| NSTM | near-surface temperature maximum |
| NWP | Northwest Passage |
| OSD | Office of the Secretary of Defense |
| PHC | Polar Science Center Hydrographic Climatology |
| POP | Parallel Ocean Program |
| psu | practical salinity units |
| PSW | Pacific Summer Water |
| PWW | Pacific Winter Water |
| RASM | Regional Arctic System Model |
| RGCM | Regional and Global Climate Modeling |
| RMS | Root Mean Square |
| S | salinity |
| T | temperature |

| | |
|----------|-----------------------------------|
| TFCC | Task Force Climate Change |
| TPR | Trans-Polar Route |
| USGS | United States Geological Survey |
| VIC | Variable Infiltration Capacity |
| WHOI | Woods Hole Oceanography Institute |
| WRF | Weather Research and Forecasting |
| z | depth |
| °C | degrees Celsius |
| ρ | density |
| θ | potential temperature |

THIS PAGE INTENTIONALLY LEFT BLANK

ACKNOWLEDGMENTS

I would like to acknowledge the great deal of support I have received during these past several years while pursuing graduate studies. First, I thank my advisors, Wieslaw Maslowski and John Colosi. They agreed to support and guide me on a path that had not yet been blazed in our department and gave me freedom to explore ideas that, at first, seemed too disparate to bring together. I would also like to thank my committee members for taking time out of their busy schedules to work with me and provide feedback along the way. In particular, I want to thank John Joseph for spearheading our involvement in ICEX and always asking the tough science questions. Andrew Roberts also deserves my deepest gratitude for continuing to push me along my journey, ensuring I met the highest rigors of scrutiny. I also appreciate Peter Guest's participation and feedback. Finally, I owe a great debt of gratitude to Peter Worcester. Not only did he come out of retirement to serve on my committee, but he also agreed to let me take a large role in the execution and analysis of the Canada Basin Acoustic Propagation Experiment.

There are many members of the Naval Postgraduate School faculty and staff that have provided the highest quality instruction and mentorship. Outside NPS, I have received substantial help from collaborators, colleagues, and mentors. I would especially like to thank Dr. Robert Osinski, Mike Cook, Dr. Gay Stewart, Commander Paula Travis, Commander Bill Sommer (Retired), Captain Tony Miller (Retired), and Captain Nick Vincent for all of their advice, mentorship, and support. I would also like to thank the U.S. Navy and my METOC. I am grateful they recognize the value of higher education, and have provided officers like myself this amazing opportunity.

Finally, I am dearly grateful for my family and friends. Thank you to the members of the Unitarian Universalist Church of the Monterey Peninsula for giving me a loving, supportive, and enriching home. My mother and father, and my brothers and sisters, have all been an inspiration to me. They have set the bar high with their actions, and motivate me to achieve beyond my own expectations. All of my hard work and effort has been not only for my country, but also for my children. Michael, Ivy, and Willow, you are my guiding stars, and I will love you always.

THIS PAGE INTENTIONALLY LEFT BLANK

I. INTRODUCTION

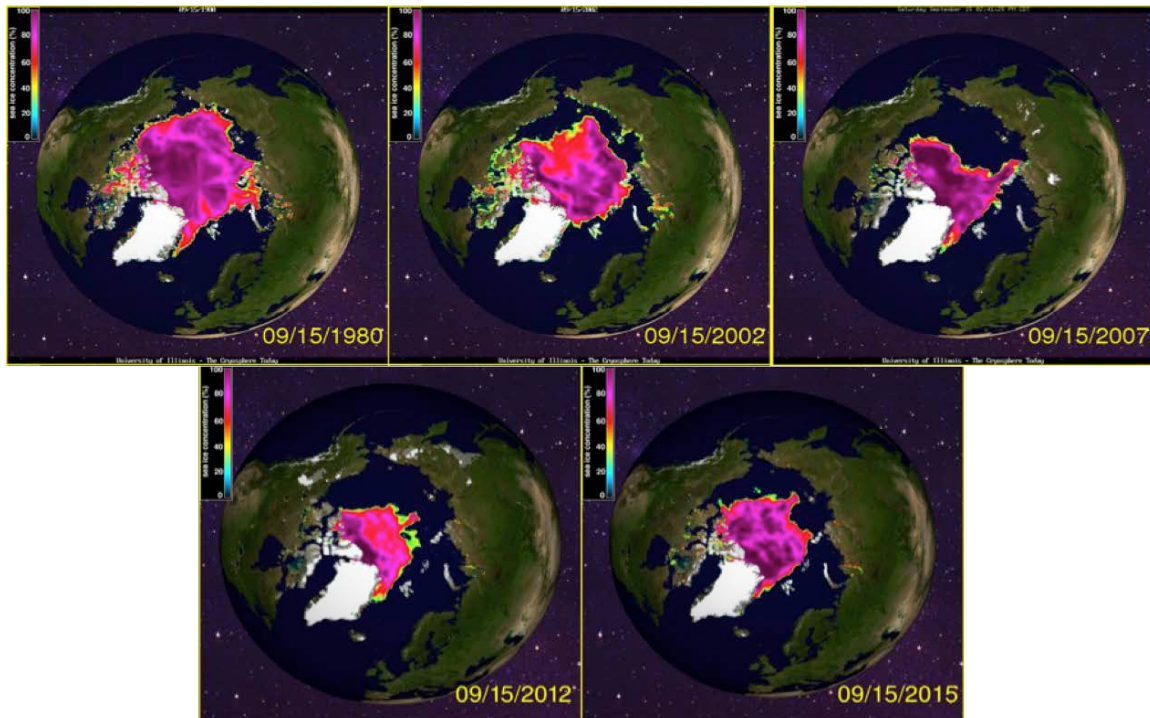
A. MOTIVATION

The global climate system is undergoing a rapid transformation due to anthropogenic factors. According to the Intergovernmental Panel on Climate Change (IPCC) ample evidence shows that a number of climate indicators are experiencing significant change (IPCC 2013). Since the 1850s, the average global surface temperature has increased by about 1°C. Between 1971 and 2010 the world's oceans have stored an additional 17×10^{22} J of heat content which has contributed to a sea level rise of 0.19 m (IPCC 2013). Due to feedbacks associated with sea ice and snow cover, in particular those related to surface albedo, changes in the net radiation balance produces a larger change in temperature in the polar regions. As a result of this so-called polar amplification, the increase in surface air temperature in the Arctic region has been almost twice the increase as observed at mid-latitudes, and even more than twice as much in some locations. Since the 1990s, the ice sheets of Greenland and Antarctica have lost tens of gigatons of mass per year, and the area covered by snow in the Northern Hemisphere has decreased by as much as 11.7 percent per decade in the last sixty years (IPCC 2013).

1. Arctic Sea Ice

The most immediate and obvious change in the Arctic has been the dramatic loss of sea ice cover and volume. Sea ice is defined as ocean water that has frozen; glaciers, ice sheets, and other land-based sources of ice are governed by other processes and are not considered sea ice. The thickness and extent of Arctic sea ice varies seasonally due to atmospheric and oceanic forcing. In general, sea ice is thickest during the winter. However, a multi-year trend has emerged. Limited observations from submarines and satellites show that the thickness of Arctic sea ice has decreased by an average of 1.8 m between 1979 and 2000 (e.g., Wadhams and Davis 2000; Kwok and Rothrock 2009). Since observations from satellite have been available starting in 1979, Arctic sea ice extent, defined as the ocean area with ice concentration greater than or equal to 15%, has

typically reached a maximum in March of about 14 to 16 million square kilometers and a minimum of about 6 million square kilometers in September, though much less in recent years (NSIDC 2016). Since 1979 the Arctic summer minimum ice extent has decreased by 13.3% per decade; a record minimum extent of only 3.6 million square kilometers was reached in 2012 (Stroeve et al. 2012; IPCC 2013; NSIDC 2016). Since the late 1990s, sea ice extent has repeatedly reached record minima with the latest record minimum in 2012 and the second lowest all-time extent recorded in 2016. The September minimum sea-ice extent for every year in the past decade has been more than 2 standard deviations below the 1981–2010 mean (NSIDC 2016). Figure 1.1 shows the decline in September sea ice concentration since 1980.

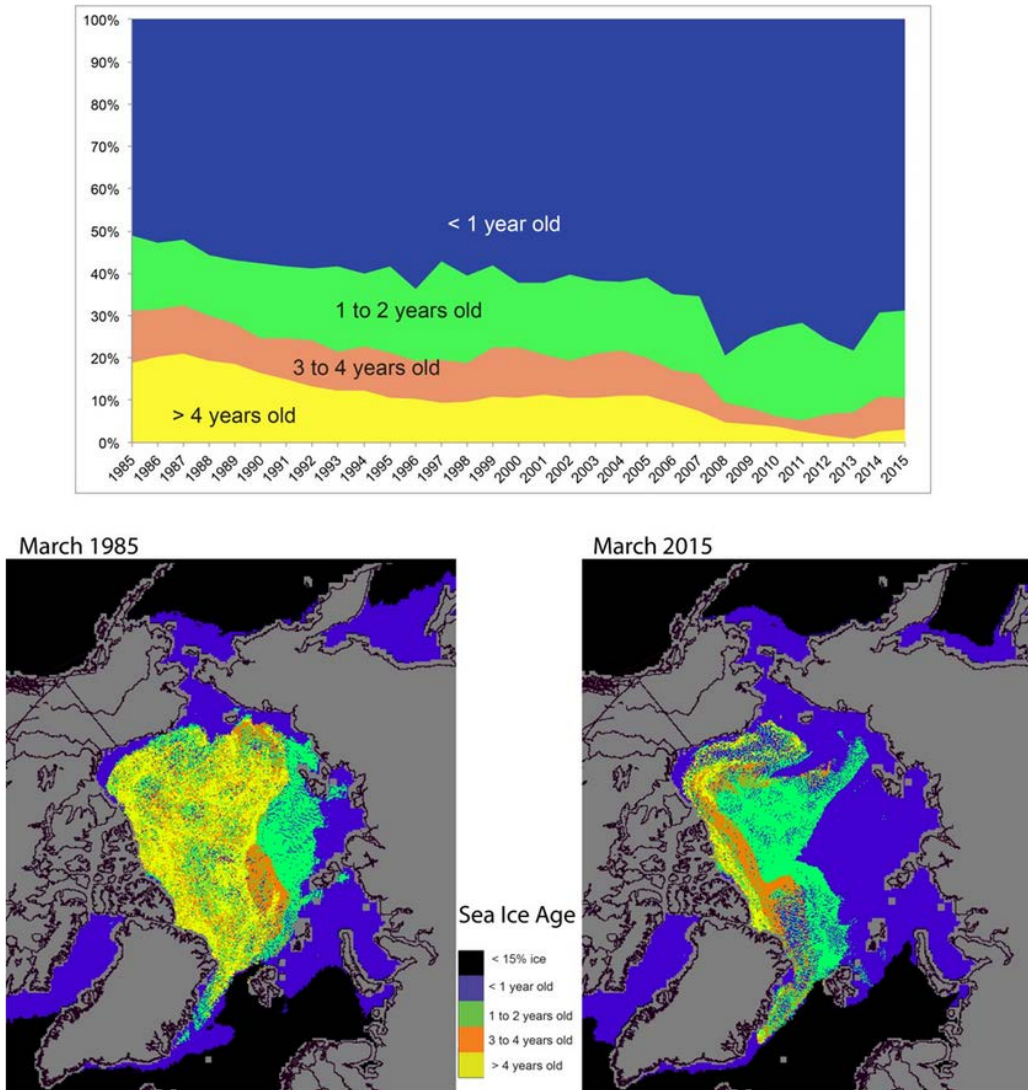


Sea ice concentrations are from September 15, 1980, 2002, 2007, 2012, and 2015 as measured by SSM/I

Figure 1.1. Arctic Sea Ice Concentrations. Adapted from Cryosphere Today 2016.

Another striking change has been the reduction in sea-ice age. When sea ice is first formed, it is considered “first-year” ice. First-year ice that survives the following

summer becomes second-year, and so on. Most of the oldest ice accumulates along the north coast of Canada and Greenland, but multi-year ice can be found throughout the central Arctic. Recently, the amount of wintertime multi-year ice has declined, and first-year ice now comprises roughly 70% of the Arctic ice pack, up from only 50% in the 1980s (Figure 1.2; Perovich et al. 2015).



A time series of ice age in March from 1985 to 2015 (top), and maps of sea ice age in March 1985 (bottom left) and March 2015 (bottom right).

Figure 1.2. Ice Age from 1985 to 2015. Source: Perovich et al. 2015.

First-year ice, due to its lower strength and thickness, is more sensitive to changes in atmospheric and oceanic forcing, and also has different acoustic and mechanical properties. A younger, thinner Arctic ice cover will have profound consequences for both physical change, and human activities such as ice-breaking and underwater acoustics.

2. Human Activity in the Arctic

As the sea ice retreats, the Arctic Ocean becomes much more accessible to human activity, both commercial and military. Maritime transits, extraction of natural resources, recreational activities, and local communities are all transforming as a response to climate change with global political and military consequences. As the extent of Arctic retreats north, a larger fraction of ocean becomes open water. The Joint World Meteorological Organization-Intergovernmental Oceanographic Commission Technical Commission for Oceanography and Marine Meteorology (JCOMM), defines “open water” as ocean with sea-ice concentrations below 10% (JCOMM 2016). Figure 1.3 depicts the anticipated Arctic transit routes as described by the Navy’s Task Force Climate Change (TFCC). Wintertime transit through the Arctic will always be blocked by sea ice, but the recent summertime minimum ice extents have been low enough to allow limited transit through the Northern Sea Route (NSR) and the Northwest Passage (NWP) in recent years (TFCC 2014). According to the Northern Sea Route Information Office (NSRIO), ice conditions have been sufficiently open since 2012 to permit an average of 39 ships per year to transit the NSR (NSRIO 2016). The NSR passes through Russian territorial waters, and Russia has claimed navigational jurisdiction over this route (Ostreng 2012). Since 2012, about 20–30 ships per year have been able to transit the NWP, 66% of which were not icebreakers (Department of Environment and Natural Resources 2016). However, because the NWP transits many straits and narrow passages, which are often inhibited by ice, regular commercial transit remains difficult (Arctic Council 2009). Remarkably, though, a commercial cruise line has already completed one transit of the NWP, and is planning to take over a thousand more adventure tourists through this route again next year (Crystal Cruises 2016). Although the Trans-Polar Route (TPR) is not yet open, it is projected to be navigable as soon as 2025 (TFCC 2014). The TPR, once reliably navigable, would offer a distance savings of 41% over the

traditional routes between East Asia and Europe via the Straits of Malacca and the Suez Canal (Humpert and Raspotnik 2012). The Arctic routes are not only shorter in distance, but also avoid the highly congested regions of the South China and Arabian Seas. These regions are also under constant threat of terrorism, piracy, and other anthropogenic threats. Alternative routes are understandably attractive to commercial investors. (Humpert and Raspotnik 2012).

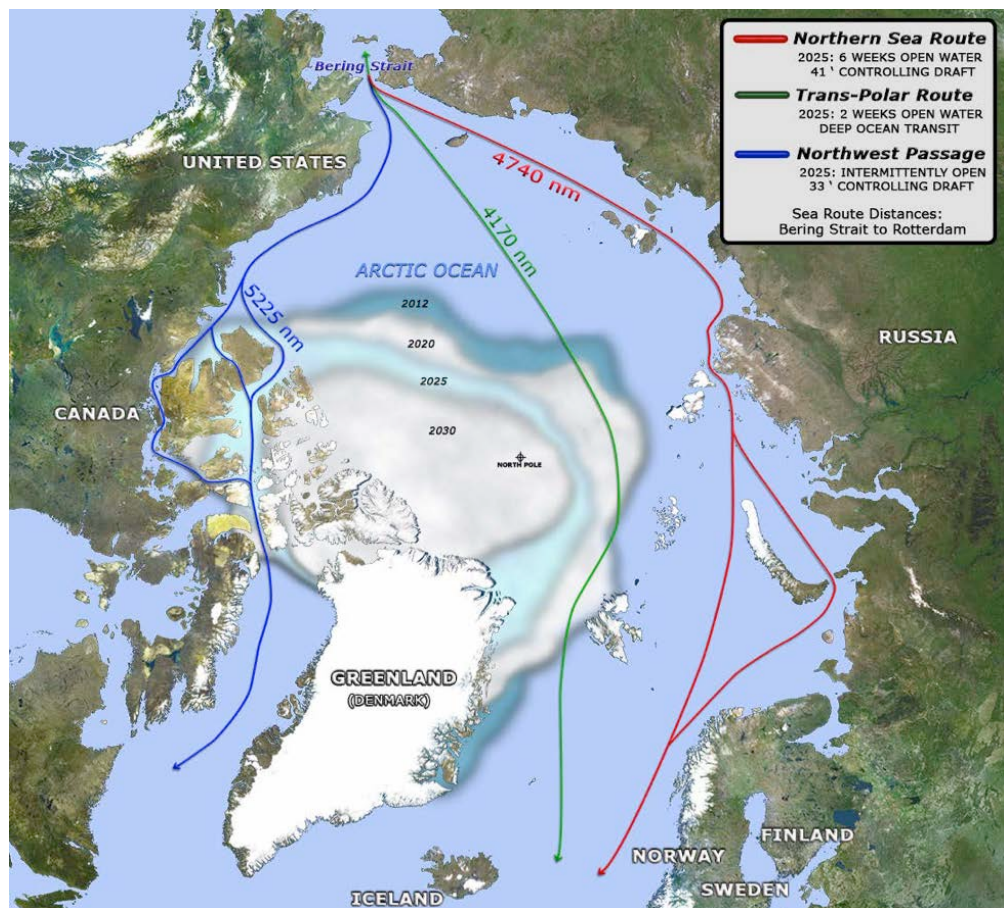


Figure 1.3. Anticipated Arctic Transit Routes with Consensus-Projected Sea Ice Extent Minima. Source: Task Force Climate Change 2014.

Whether for recreation, scientific research, or economic gain, any Arctic traveler will be faced with significant hazards throughout the year. Winter will always bring darkness, extreme cold, and sea ice every year. The timing of freeze-up will depend strongly on local weather conditions, which remain a challenge to predict in this

observationally data-poor region of the globe. Similarly, spring melt is often interrupted by cold snaps, making the start of the navigable season a challenge to predict as well. These so-called “shoulder seasons” will present a serious risk to those who wish to maximize their time in the Arctic (TFCC 2014). To mitigate this risk, governments must be prepared to respond to emergencies, both human and environmental, in the harsh and remote Arctic.

Currently, there are several different agreements, treaties, and other sources of authority that influence international activities in the Arctic. Some of these authorities overlap or conflict, leaving some uncertainty (Berkman and Young 2009; Koivurova and Molenaar 2009). A report by the United States Geological Survey (USGS) estimated that substantial reserves of fossil fuels are present in the Arctic region. That estimate includes 90 billion barrels of oil, 44 billion barrels of liquid natural gas, and 1669 trillion cubic feet of natural gas (USGS 2008). It is safe to assume that economic interests in the region will only grow. Also, as cold-water species of fish move north (Sigler 2009; Logerwell 2008), the global fishing economy is also making plans for the future. As a result of these economic interests, a land-grab of sorts has begun in the Arctic. The United Nations Convention on the Law of the Sea (UNCLOS) spells out the process by which nations ratifying the treaty may claim an Economic Exclusion Zone (EEZ), a region where use of seabed activities is authorized only for the nation claiming it (United Nations 2016). The EEZ may be extended to the edge of a continental shelf; current and potential disputes over which are depicted in Figure 1.4.

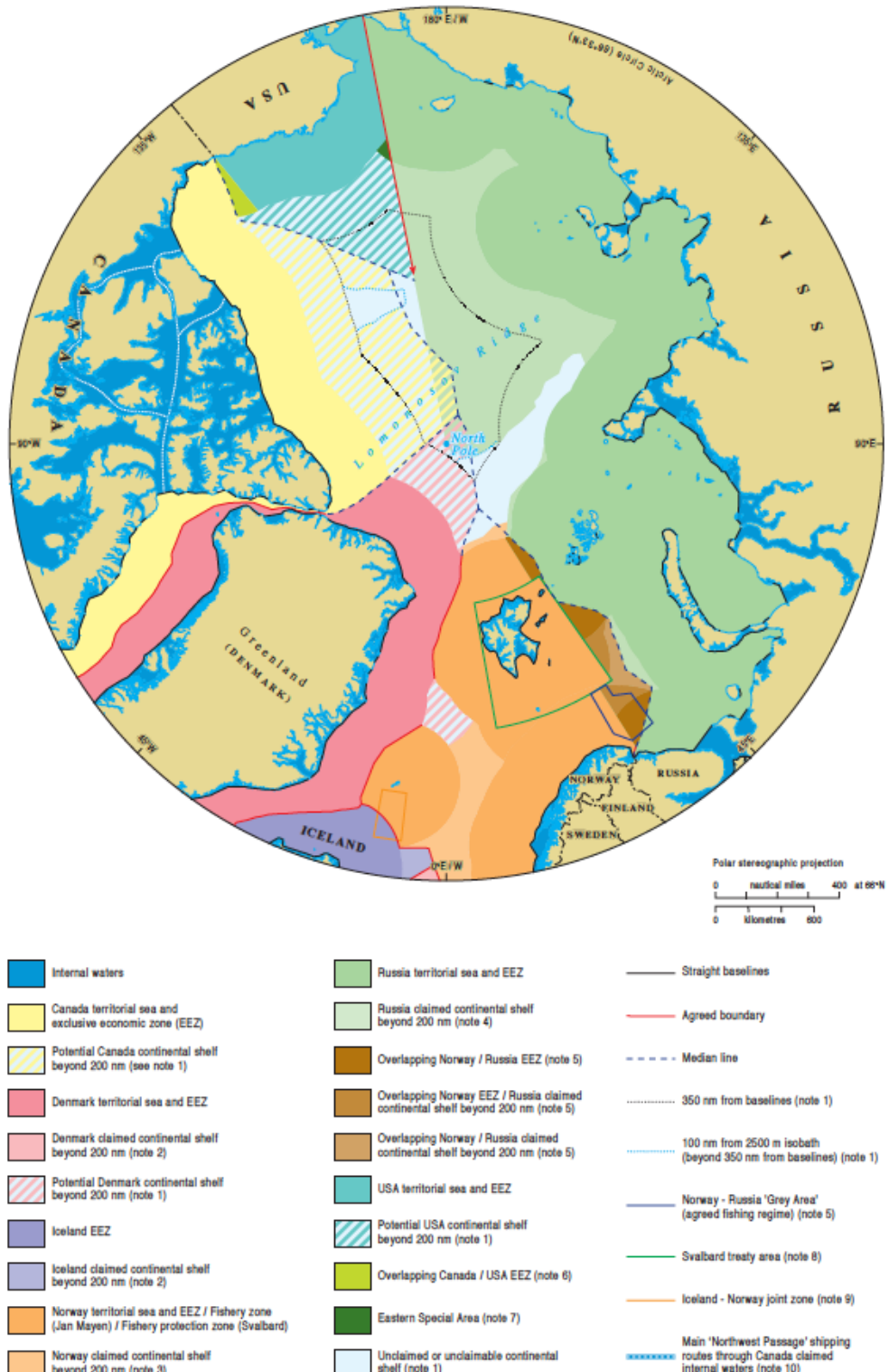


Figure 1.4. Maritime Jurisdiction and Boundaries in the Arctic Region.
Source: IBRU, Durham University 2016.

3. U.S. Arctic Strategy

In addition to the risk of conflict over competing territorial claims, an increased human presence in the Arctic results in an increased risk of humanitarian and environmental disasters (Executive Intelligence Review 2016, National Intelligence Council 2016). The United States must, therefore, consider its responsibilities with respect to the Arctic. The U.S.’s foundational strategic document, the *National Security Strategy*, states that the “United States is an Arctic Nation with broad and fundamental interests in the Arctic region” (White House 2010). In 2015, the *National Security Strategy* was updated to include the U.S.’s commitment to combatting climate change and working with the international community to prevent conflict in the Arctic (White House 2015). The subsequent *National Strategy for the Arctic Region*, released in 2013, lists three lines of effort:

- Advance United States Security Interests
- Pursue Responsible Arctic Region Stewardship
- Strengthen International Cooperation

The Strategy further listed guiding principles for these efforts:

- Safeguard Peace and Stability
- Make Decisions Using the Best Available Information
- Pursue Innovative Arrangements
- Consult and Coordinate with Alaska Natives (White House 2013)

Along with the *Implementation Plan for the National Strategy for the Arctic Region* (White House 2014), the *National Strategy for the Arctic Region* addresses broad national goals. In 2013, the Office of the Secretary of Defense (OSD) issued its *Department of Defense (DOD) Arctic Strategy*, which defines the desired end-state in the Arctic as “a secure and stable region where U.S. national interests are safeguarded, the U.S. homeland is protected, and nations work cooperatively to address challenges” (OSD 2013). These goals are supported by ensuring security, supporting safety, promoting defense cooperation, and preparing to “respond to a wide range of challenges and contingencies” (OSD 2013). Presently and in the near future, the Navy’s physical presence and operational requirements are met by the use of submarines, whose safety

and mission sets require a thorough understanding of the physical and acoustical ocean environment. To support the U.S.’s national goals and operating forces, the DOD “will leverage work done by the scientific and academic communities and seek opportunities to contribute to the observation and modeling of the atmosphere, ocean, and sea ice conditions … to enhance military environmental forecasting capabilities” (OSD 2013).

The Navy’s Task Force Climate Change (TFCC) was created in 2009 (four years before the *National Strategy for the Arctic Region* had been written) with the explicit purpose of “recommending policy, strategy, roadmaps, force structure, and investments for the Navy regarding the Arctic and Climate Change” (Department of the Navy 2009). The *U.S. Navy Arctic Roadmap*, issued in 2009 and updated in 2014, states that although the threat of armed conflict in the Arctic is currently low, the U.S. does have important security responsibilities. One of these responsibilities is to improve domain awareness in the Arctic region; a task the Navy hopes to achieve with the help of public and private sector partners (TFCC 2014). Part of this domain awareness includes ability to predict the Arctic physical environment, especially sea ice extent, ice and snow thickness, ice-sea-air interaction physics, and other processes in the ocean. The Navy encourages research into and development of comprehensive Arctic System Models (TFCC 2014).

B. RESEARCH GOALS

To support the U.S. and DOD strategies and objectives for the Arctic, the research conducted for this dissertation focused on observing and modeling the physical oceanography of the upper Arctic Ocean with an emphasis on the implications of climate change on acoustic operations in the western Arctic. There are two major research goals with several supporting science questions:

- 1. To characterize the present Arctic Ocean hydrography and resulting sound-speed structure**
 - What is the current mean state of the Arctic sound speed field?
 - How does the current sound speed field compare to that of previous decades?
 - What small-scale variations are present in the sound speed field and what causes them?

2. **To evaluate and guide improved model representation of Arctic Ocean hydrography and sound-speed structure.**
 - How well do models represent the past and current hydrography and sound speed field?
 - What model physics, parameterizations, and configurations allow improved representation of hydrography and sound speed field?
 - Are climate models suitable for making projections of future hydrography, especially with respect to heat content, feedbacks, and the mean sound-speed field?

C. STRUCTURE OF THIS DISSERTATION

Following an introduction to the geography and oceanography of the region of study, the research completed for this dissertation will be presented in the form of two research journal articles that have been submitted for peer-review and publication. The first paper, “Observations of the Upper Ocean Thermohaline Structure and Variations in the Canada Basin, Summer 2015” (DiMaggio et al. 2016a) addresses the first research question by discussing the observational work that set out to explore current acoustic conditions in the Canada Basin. The second paper, “Evaluation and Sensitivity of Climate Model Skill at Representing Upper Arctic Ocean Hydrography” (DiMaggio et al. 2016b) investigates the second research question by directly examining global climate models and the Regional Arctic System Model (RASM). The final chapter of this dissertation will tie together results from these two studies to offer some conclusions and recommendations for acoustic operations and future research.

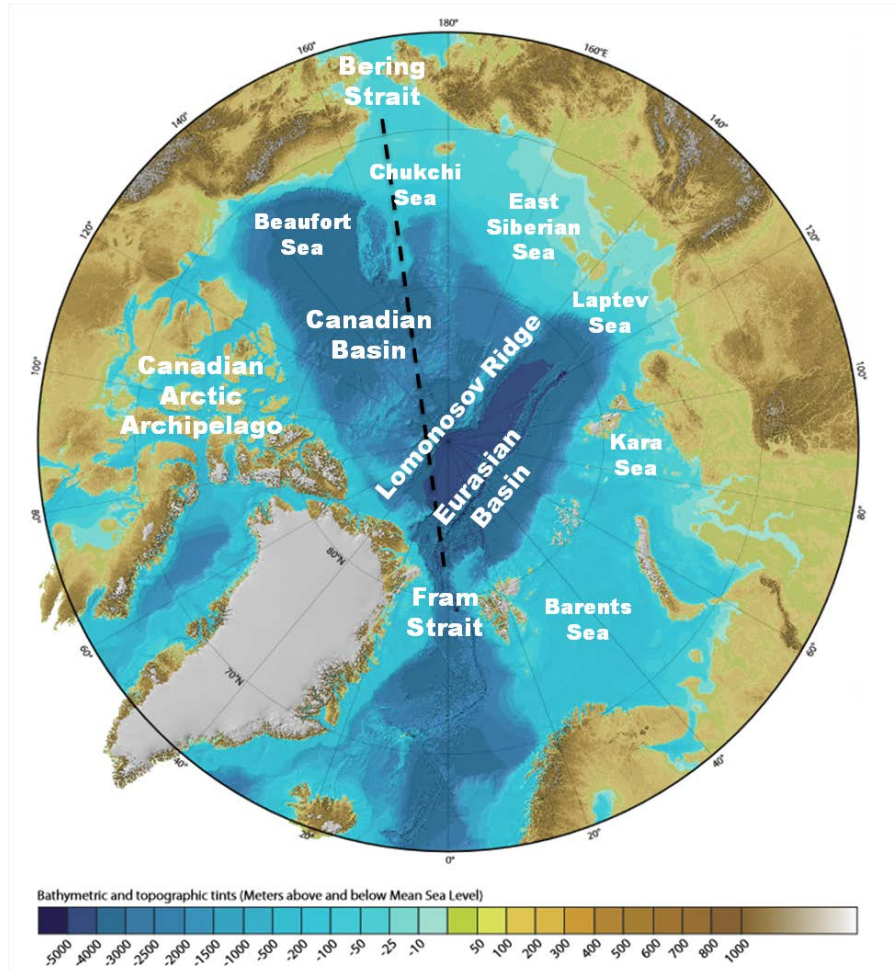
D. ARCTIC PHYSICAL OCEANOGRAPHY AND ACOUSTICS

1. Physical Oceanography of the Arctic

a. Water masses and circulation

The Arctic Ocean is different from other oceans in that it is both mediterranean, surrounded on all sides by land with limited physical connections to the Atlantic and Pacific (Figure 1.5), and it undergoes an extreme seasonal cycle of solar radiative forcing. The properties of this ocean are dictated by the influence of the Pacific and Atlantic

oceans, sea ice, precipitation, winds, solar and infrared radiation, and the seasonal land hydrology (e.g., river runoff).



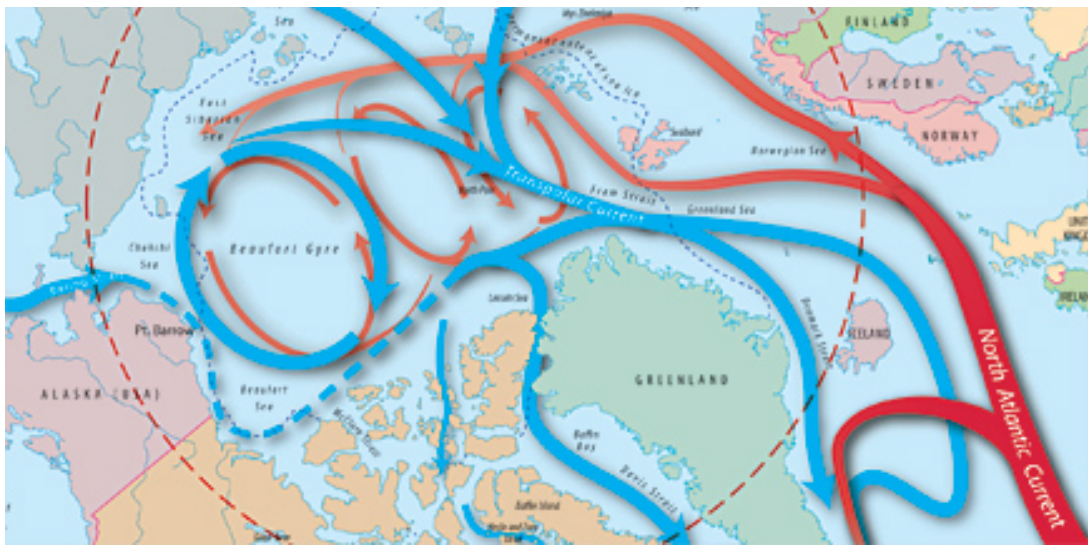
The dashed black line indicates the approximate location of the cross section depicted in Figure 1.7

Figure 1.5. Annotated Map of Arctic Bathymetry and Topography Region.
Adapted from Jakobsson et al. 2012.

The surface mixed layer varies seasonally under the influence of atmospheric forcing and seasonally varying sea ice growth and melt. During the winter months, the surface mixed layer is maintained at approximately 30 to 40 m by negative buoyancy fluxes caused by negative heat fluxes from the atmosphere and positive salt fluxes from ice formation. At the onset of the melt season, the influx of low-salinity water from

melting sea ice and increased river runoff causes the mixed layer to shoal rapidly to less than 20 m. A strong summer pycnocline is setup between the new summer mixed layer and the remnant mixed layer from the previous winter, significantly limiting vertical mixing (Toole et al. 2010). The circulation of surface waters is driven primarily by wind forcing, and modulated by sea-ice drift. A climatological high-pressure cell above the Beaufort Sea creates an anti-cyclonic gyre in the sea-ice circulation, commonly referred to as the Beaufort Gyre. The northernmost branch of the Beaufort Gyre feeds the Transpolar Drift, which transports sea ice and surface waters from the East Siberian and Laptev Seas toward Fram Strait (Rudels 2001).

Beneath the mixed layer lie water masses that originated in either the Pacific or Atlantic Oceans. Warm and salty Atlantic water enters the Arctic Ocean via the Fram Strait and the Barents Sea (Figure 1.6). Cooling at the surface increases the density of Atlantic water, which submerges below the fresher and more buoyant surface mixed layer. This Atlantic Layer, also sometimes called Arctic Intermediate Water, is relatively warm ($> 0^{\circ}\text{C}$) and salty ($> 34.5 \text{ psu}$), and can be found throughout the central Arctic basin (Steele et al. 1998; Rudels et al. 2004; Rudels 2012). The Atlantic water generally circulates as a boundary current, guided by the bathymetry of continental slope. This boundary current gets split off due to bathymetric features, and as yet not well-understood processes (e.g., mesoscale eddies) distribute this water throughout the deep basins (Rudels 2001). In the eastern Arctic Ocean, a strong temperature and salinity gradient exists between the surface waters and the Atlantic Layer. In the western Arctic, however, waters originating in the Pacific Ocean complicate the vertical water-mass structure.

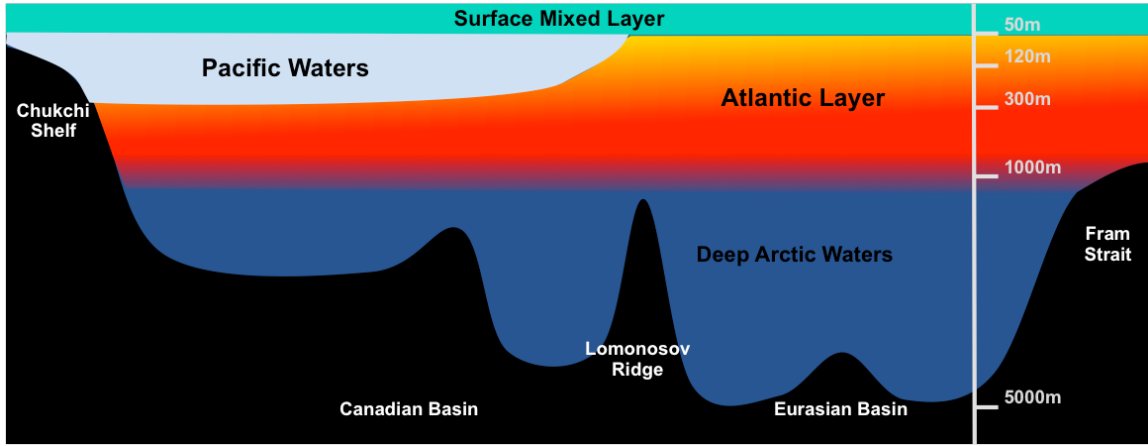


Red arrows indicate relatively warm Atlantic waters which lie at intermediate depths in the Arctic Ocean; blue arrows indicate relatively cool surface and Pacific waters

Figure 1.6. Schematic Diagram of General Oceanic Circulation in and Around the Arctic Ocean. Source: WHOI 2014.

b. Hydrography of the Canada Basin

The Canada Basin is the deep basin of the western Arctic Ocean adjacent to the Alaskan coast. Thanks largely to the observational record collected by the Ice-Tethered Profile (ITP) program of the Woods Hole Oceanography Institute (WHOI 2016), and the ship-based observations compiled in the Polar Science Center Hydrographic Climatology (Steele et al. 2001), the hydrography of the Canada Basin is fairly well known. Water from the Pacific enters the Arctic via the narrow and shallow Bering Strait. Once it reaches the Canada Basin, this water is cooler and fresher than the Atlantic Layer, but is saltier than the surface mixed layer. The result is a layering of the water masses (Figure 1.7).



The approximate location of this cross section is depicted in Figure 1.5. Features are not drawn to scale; the near-surface depths are exaggerated. The Lomonosov Ridge divides the Arctic into two basins, the Canadian Basin in the west, and the Eurasian Basin in the east. The shallowest layer is the surface mixed layer, which extends from the surface to approximately 50m. Below this lie the Pacific waters and the Atlantic Layer. The Atlantic Layer reaches to a shallower depth in the east, where it enters the Arctic via the Fram Strait.

Figure 1.7. Schematic Representation of the General Layers in the Arctic Ocean in Cross Section from the Bering Strait to the Fram Strait. Adapted from DiMaggio 2012.

The Pacific waters are modified over the Bering and Chukchi shelves by seasonally varying atmospheric and sea-ice conditions, resulting in two distinct water masses that Coachman and Barnes (1961) named the Pacific summer water (PSW) and Pacific winter water (PWW). PSW has a temperature of approximately -1.0°C (Steele et al. 2004) and salinities ranging between 31 psu and 33 psu (Shimada et al. 2006; Steele et al. 2004). PWW is cooler (near freezing) and has salinity above 33 psu; therefore, it is situated below PSW (Coachman and Barnes 1961). The net result of these layered water masses is a highly stratified upper ocean, with strong density gradients, especially at the base of the mixed layer and the top of the Atlantic Layer.

There has been a measurable change to the hydrography of the Canada Basin in recent years. A near-surface temperature maximum (NSTM) has been observed between the surface mixed layer and the PSW, and has been expanding in lateral extent and heat content in recent years due to increased solar radiation absorption through decreased ice cover (Jackson et al. 2010, Jackson et al. 2011, Steele et al. 2011, Gallaher et al. 2016).

Timmermans et al. (2014) found that the PSW has increased in heat content and freshwater content in recent years, which likely results in increased vertical heat fluxes. Many local and advective processes govern the properties of, and therefore the changes to, the NSTM and PSW. Surface heat fluxes from the atmosphere, sea ice, and solar insolation dictate the properties of the NSTM, both directly and indirectly through turbulent mixing (Steele et al. 2011). These processes also affect the source water for the PSW, as do the advective processes of lateral eddy flux, boundary currents, shelf-basin exchange, and general circulation (Pickart et al. 2005, Spall et al. 2008, Watanabe et al. 2009, Maslowski et al. 2014, Timmermans et al. 2014). Each of these processes is the focus of active research in the Arctic region, in both observational and modeling studies. Understanding these processes, associated feedbacks, and how to incorporate them in coupled climate models will be critical to making projections of future climate states.

c. Internal Waves

In an ocean layered with water masses of different densities, there is the potential for internal gravity waves. In deep basins internal waves are ubiquitous, and generally follow the Garrett-Munk (GM) model spectra (Garrett and Munk 1971), and the internal wave field energy in the Arctic is an order of magnitude or more below that found at lower latitudes (Levine et al. 1985, Levine et al. 1987). A seasonal cycle exists in the Canada Basin internal wave field, with a maximum energy in the summer when sea ice coverage is at a minimum (Dosser and Rainville 2016). As the sea ice retreats, increased momentum fluxes from the atmosphere have increased the internal wave energy levels and variability in the Canada Basin (Dosser and Rainville 2016); however, there has been no associated rise in internal wave mixing, possibly due to increased stratification (Guthrie et al. 2013). Internal waves provide an avenue for wind energy to penetrate through the water column, inducing diapycnal mixing and water mass modification (Munk and Wunsch 1998). In the Arctic, a changing internal wave field could have an impact on the stratification and distribution of heat content; a more energetic internal wave field could allow for the heat of the PSW to reach the surface, and would have significant impacts to acoustic propagation.

d. Global and regional modeling

There is a large multinational effort using computer simulations to better understand how and why the Arctic is changing, and how the Arctic influences and is influenced by the global climate system. These modeling efforts span various temporal and spatial scales. Presently there are no models that can resolve important processes at all relevant scales. Small-scale processes, such as turbulent mixing which acts on scales on the order of one meter and one minute (McPhee 2008), and the large-scale dynamics of basin- to global-scale feedbacks and forcings, such as greenhouse gases and meridional overturning circulation, are not resolved at the same time in models. Therefore, models are generally designed to represent a limited range of scales. Global climate models (GCM), and Earth system models (ESM), focus on large spatial scales and can often be run for long time scales in order to investigate such processes as climate change. The length of simulation and spatial scale comes at a high computational cost, and most GCMs and ESMs run at relatively coarse resolution. The Community Climate System Model (CCSM), for example, uses a relatively coarse resolution of 1° in both ocean and atmospheric components. This means that CCSM grid points are roughly 111 km apart (Stevens et al. 2012). Similarly, the model used by the Max Plank Institute for Meteorology has an atmospheric component grid spaced at 1.8° (~ 200 km) and an oceanic component grid spaced at 1.5° (~ 167 km) (Stevens et al. 2012). However, models with much higher resolutions, but lower than 10 km, will still misrepresent or even completely exclude mesoscale processes such as eddies, buoyancy-driven coastal and boundary currents, sea-ice drift, sea-ice thickness distribution, sea-ice concentration, sea-ice deformation, and air-sea-ice interactions (DuVivier and Cassano 2013; Maslowski et al. 2008; Maslowski et al. 2012).

Upper Arctic Ocean hydrography, in particular, has been insufficiently represented in current global and Arctic regional models. Many models tend to produce a continuously stratified upper layer, rather than the layered water masses observed in the western Arctic, which suggests that missing model physics may be related to vertical mixing or shelf-basin exchanges (Holloway et al. 2007). Deficiencies may be present in not just the ocean model, but also in the sea ice and atmospheric models or in how they

are coupled. Poor resolution in both time and space may be underrepresenting the significance of small-scale processes.

This dissertation aims to identify the existing model limitations and provide guidance on what model improvements can be made in representing upper Arctic Ocean hydrography in order to enhance our understanding of the important processes that create and maintain the thermohaline structure, as well as the fate of this structure under climate change.

2. Underwater Propagation of Sound in the Arctic Ocean

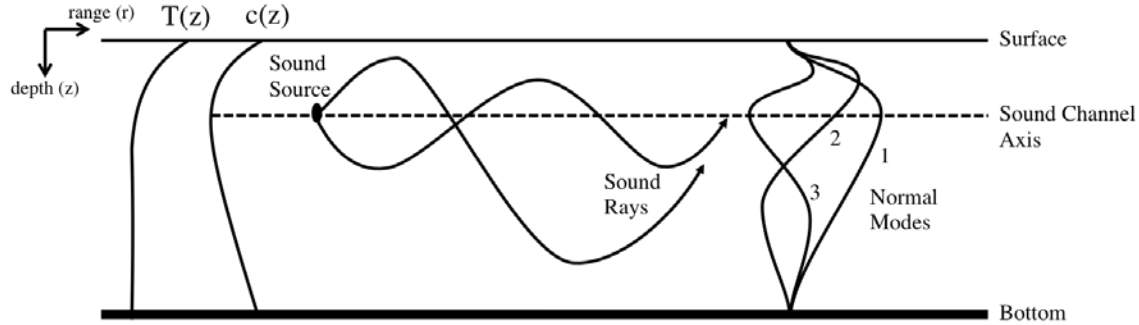
a. *Basics of sound propagation*

Because seawater attenuates electromagnetic energy rapidly, yet permits acoustic energy to propagate to very long distances, sound is the primary long-range method for naval forces to navigate, communicate, and observe in the undersea environment. The propagation of sound in water is controlled by the speed of sound in water and how that sound speed changes in space and time, as well as the surface and bottom boundary conditions. Sound speed (c) in seawater depends primarily on temperature (T), salinity (S), and pressure, or depth (z) since pressure increases linearly with depth. An increase in T , S , or z will increase c . Across operationally relevant ranges, the largest variability in c is in depth, so c is primarily a function of z . The solutions to the acoustic wave equation in seawater result in two models of visualizing sound propagation: ray theory and normal mode theory. In ray theory, the propagation of acoustic energy is said to travel along paths that curve according to the varying sound-speed properties of seawater. As sound propagates from a source, a vertically varying c will cause sound rays to refract, or bend, according to Snell's Law:

$$\frac{\cos \theta(z)}{c(z)} = \text{constant} \quad 1.1$$

where θ represents the angle of the sound ray with respect to the horizontal. The result of Snell's Law is that sound refracts away from higher sound speed, or that sound bends towards low sound speed regions. If a sound-speed minimum exists, some rays will oscillate about that minimum, creating a channel in which sound may propagate for long

distances without interacting with the surface or bottom (Figure 1.8). Surface and bottom interactions will result in energy loss due to the conversion of sound energy into heat through absorption, or the scattering of sound energy out of the ray path (Kuperman 2001). In cases where sound is trapped in a sound channel, normal mode theory is helpful. Normal mode theory arises from the fact that solutions to the acoustic wave equations of a bound system can be broken into a vertically varying component, and a radially varying component. The vertical solutions define distinct “modes” of alternating high- and low-intensity sound regions, much like modes of vibrations on a taut string or modes of probability of locating a quantum particle in a bound state (Figure 1.8).



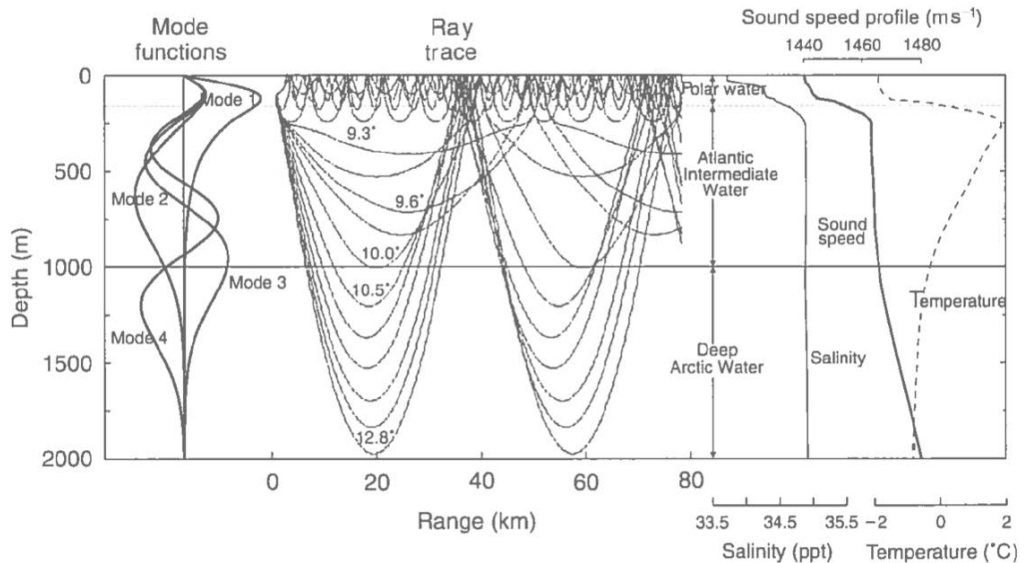
The presence of a sound-speed minimum creates a sound channel about which sound rays will oscillate. The first three normal modes of trapped sound energy are also depicted.

Figure 1.8. Schematic Diagram of a Generic Deep-Ocean Temperature Profile ($T(z)$) and Resulting Sound Speed Profile ($c(z)$).

The sound-speed structure, however, does not remain constant in time and space, so we must update this model of sound propagation. Coherent acoustic transmissions, especially those used in communication and undersea warfare, are subject to acoustic variability, which is induced by perturbations of the sound-speed field at various scales. Mesoscale eddies (Cornuelle et al. 1995; Wolfson and Tappert 2000), internal tides (Dushaw et al. 1995, Dushaw et al. 2011), random internal waves (Colosi 2016), and spicily thermohaline structure (Dzieciuch et al. 2004) will all cause distortions to the transmitted sound signal, often necessitating a stochastic approach to making predictions.

b. The Arctic acoustic environment

The hydrography of the Arctic Ocean results in a sound-speed structure that is not found in other deep-ocean basins. As temperature and salinity increase from the surface to the core of the Atlantic Layer (~500m), sound speed also increases rapidly (Figure 1.9). Below this depth, pressure effects begin to dominate and sound speed continues to increase, despite temperature decreasing slightly. Therefore, the resulting full-depth sound-speed profile is monotonically increasing, creating a sound channel with axis near the surface supporting strong first and second modes of propagation (Kutschale 1961). Acoustic energy is therefore repeatedly refracted upwards and reflected off the sea ice, and so the ice-ocean interface plays a significant role in the attenuation of sound. The acoustical properties of sea ice, and sea ice's effects on underwater acoustic propagation are complex and not yet fully understood (e.g. Yew and Weng 1987; Rajan 1993, Alexander et al. 2013), yet the net result is that high frequency signals are greatly attenuated by sea ice and only low frequency (below 30 Hz) propagate to long distances (Kutschale 1961; Buck and Greene 1964, Mikhalevsky 2001).



Ocean. Included are modal structure, ray traces, and profiles of salinity, temperature, and sound speed.

Figure 1.9. Typical Acoustic Conditions in the Arctic. Source: Mikhalevsky 2001.

As Arctic sea ice becomes younger and thinner and as the summer ice extent becomes smaller, acoustic propagation conditions are likely changing. Previous studies were mainly concerned with long-range propagation of low frequencies under pack ice (Kutschale 1961, Marsh and Mellen 1962, DiNapoli and Mellen 1985, Mikhalevsky et al. 1999). As the mean state of Arctic hydrography is evolving, the results of these long-range propagation experiments may no longer be valid. Also, the scattering of sound by sea ice is dependent on the thickness, age, and roughness of the ice, all of which are changing. Several recent and current research efforts are aimed at updating our knowledge of the Arctic acoustic environment, including the Transarctic Acoustic Propagation experiment (Mikhalevsky et al. 1999), the Arctic Climate Observations using Underwater Sound experiment (Gavrilov and Mikhalevsky 2002; Gavrilov and Mikhalevsky 2006), the Thin-ice Arctic Acoustic Window experiment and the Canada Basin Acoustic Propagation Experiment. Much of this work is being done to understand how the changing sea-ice conditions and overall warming of the Arctic Ocean are affecting acoustic propagation on seasonal to interannual timescales.

There are several key issues associated with Arctic acoustics that should be investigated. First, the mean sound speed field, its fluctuations, and the main physical processes driving them are still not well understood, especially on seasonal and interannual time scales. In particular, the increasing temperature of the Pacific Summer Water has the potential to create a sound speed maximum at that depth, possibly changing the acoustic modal structure and limiting the attenuating affects of sea ice reflection. Second, the relative contributions of eddies, internal waves, and spice variability to the sound speed fluctuation field, and their dependence depth and season are not well understood. Third, the space and time scales of the sound speed fluctuations need to be well understood in order to adequately model these processes, either stochastically or deterministically. Finally, the affects of these ocean fluctuations on sound propagation should be explored. How do these fluctuations affect different acoustic frequencies; are there optimal frequencies for different applications? For coherent signals, in what cases would one expect unsaturated, partially saturated or fully saturated signal propagation? This dissertation supports these research efforts by focusing on

smaller spatial and temporal scales, especially the acoustical implications of internal waves and spice, as well as evaluating and improving the modeling of ocean hydrography and sound-speed structure.

THIS PAGE INTENTIONALLY LEFT BLANK

II. OBSERVATIONS OF THERMOHALINE SOUND-SPEED STRUCTURE INDUCED BY INTERNAL WAVES AND SPICE IN THE SUMMER 2015 CANADA BASIN MARGINAL ICE ZONE

This chapter was submitted to *Elementa: Science of the Anthropocene* for publication. Except for the figure numbering, the formatting has been retained as submitted. As the main author of the work, I made the major contributions to the research and writing. Co-authors include J. Colosi¹, P. Worcester², M. Dzieciuch², J. Joseph¹, and Annalise Pearson¹.

A. INTRODUCTION

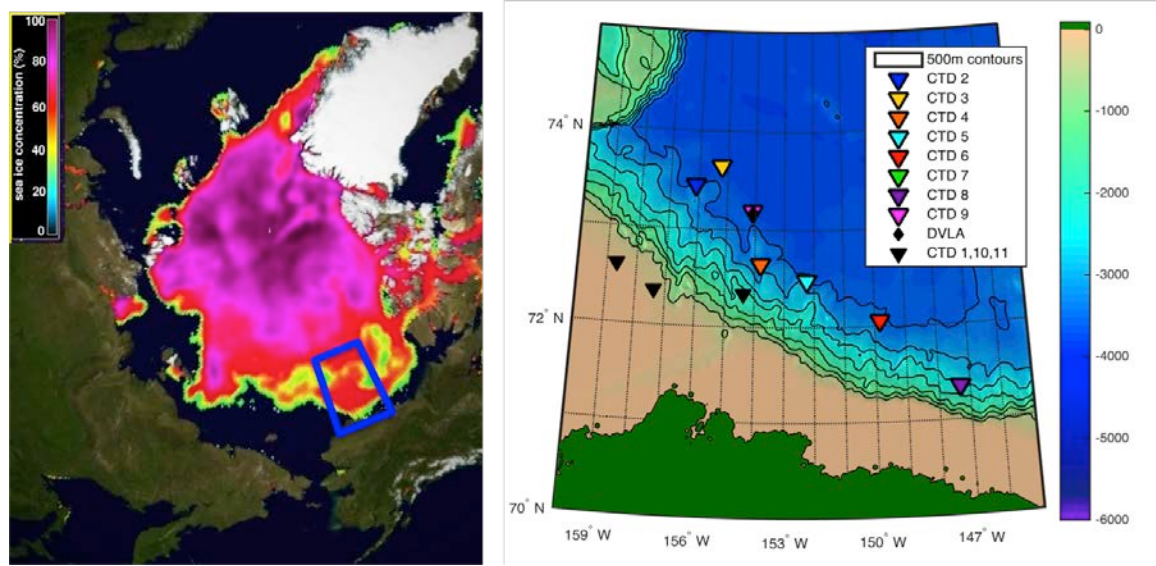
In the past few decades there have been substantial changes in the Arctic region including a rapid decline in summer sea ice extent (Stroeve et al. 2012), as well as changes in ocean freshwater content (Rabe et al. 2014) and ocean heat content (Lique and Steele 2013). These changes have attracted not just scientific interest, but also the attention of commercial organizations, governments, and militaries. Under the sea there are many potential activities that would rely on sound, including communication, acoustic tomography, seismic exploration, and sonar. Each of these applications requires a good understanding of the structure and variability of the ocean acoustic conditions, conditions which appear to be in a state of transition.

The Canada Basin Acoustic Propagation Experiment (CANAPE) is just such an effort to assess present ocean acoustic conditions with a focus on physical oceanographic processes that impact sound propagation on time scales from minutes to months. CANAPE consists of a yearlong experiment in the Canada Basin of the Arctic Ocean during 2016–2017 as well as a month-long pilot study conducted during the summer of 2015. The purpose of the pilot study was to test equipment, observe transmission loss for designing the main experiment acoustic array, and to quantify oceanographic and acoustic variability. This paper describes the observations of thermohaline structure and

¹Department of Oceanography, Naval Postgraduate School

²Scripps Institution of Oceanography, University of California, San Diego

variability collected during the CANAPE pilot study, which was carried out in the Beaufort Sea close to the continental slope off Alaska (Figure 2.1). Due to the short duration, the focus of the pilot was on internal waves and spice.



Left panel: sea ice concentration for 30 July 2015, with the approximate region of study outlined in blue. Right panel: expanded view of the region of study with observation locations indicated. Bathymetry shading is in meters, with 500 m depth contours overlaid.

Figure 2.1. Region of the CANAPE Pilot Study. Adapted from University of Illinois 2016.

The Canada Basin is a deep-water basin north of Alaska and west of the Canadian Arctic Archipelago. To the west of the Canada Basin lies the broad and relatively shallow Chukchi Shelf, which provides input of relatively warm Pacific waters into the Canada Basin. Prevailing winds drive the anticyclonic Beaufort Gyre, which transports sea ice and upper ocean water masses from the central Arctic Ocean in a clockwise direction around the basin. Between 1983 and 2014 sea ice concentration in the Beaufort Sea has decreased at a rate up to 15 % per decade, and the annual duration of open water has increased as much as three weeks (Galley et al. 2016). Of significant acoustical consequence, these changes have resulted in the emergence of a large-scale summer marginal ice zone (MIZ) in the Canada Basin, thus changing the dominant processes

governing acoustic/ice interactions, air/sea interactions, and changing thermohaline sound-speed structure.

Changes in the sound speed structure in the upper few hundred meters of the ocean have been striking. Below the surface waters around 100 m depth, a temperature maximum has emerged that appears to be increasing in intensity and lateral extent (Jackson et al. 2010; Steele et al. 2011). One consequence of this feature is a new subsurface acoustic duct that can allow long-range acoustic propagation with little energy loss. These waters are of Pacific origin and fill the upper to intermediate depths of the Canada Basin. Coachman and Barnes (1961) named these layers Pacific summer water (PSW) and Pacific winter water (PWW). PSW is characterized as having a temperature maximum greater than -1.0°C (Steele et al. 2004) with salinities of 31–33 psu (Shimada et al. 2001; Steele et al. 2004). Timmermans et al. (2014) have shown that the PSW has increased in heat content and freshwater content in recent years, with potential impacts to stratification and vertical heat fluxes. Below PSW is the PWW that is generally found below 150 m and can be identified by a temperature minimum and salinities greater than 33 psu (Coachman and Barnes, 1961). PWW is believed to be formed by ice formation on the Chukchi Shelf during winter months (Pisareva et al. 2015). Although this water mass seems to be fairly consistent in its properties, Steele et al. (1998) found that its lateral extent may be variable in time. Below the PWW a strong halocline and thermocline marks the transition to water of Atlantic origin, simply called Atlantic Water (AW), which is characterized as warm ($T > 0^{\circ}\text{C}$) and salty ($S > 34.5$ psu; Rudels et al. 2004). The cumulative effect of these layered water masses is a highly stratified upper ocean, with strong density gradients and high buoyancy frequencies, especially at the transitions between water masses. Changes in these water masses on time scales from interannual to buoyancy period are of fundamental interest to a broad spectrum of Arctic scientists, including acousticians.

Deep-water sound propagation can be used for many practical applications including remote sensing, navigation, and communication. Of fundamental importance are the features of the water masses (e.g., the sound channel) and their inherent variability due to ocean processes (Colosi 2016). This variability may be caused by eddies

(Cornuelle et al. 1985; Wolfson and Tappert 2000), internal tides (Dushaw et al. 1995; Dushaw et al. 2011), internal waves (Colosi 2016; Flatté et al. 1979), and spicy thermohaline structure (Colosi et al. 2013; Dzieciuch et al. 2004). Ocean variability translates into acoustic variability, and for any given acoustic system there is a complex relationship between signal stability and randomization and the space/time scales of the ocean (Colosi 2016). To make progress on this problem requires both deterministic and stochastic ocean models that can then be interfaced with acoustic models. An important example of a stochastic model is the Garrett-Munk internal wave spectrum (Garrett and Munk 1971). The goal of this study is to examine two processes that can be considered stochastic, internal waves and spice, and to quantify their space/time scales and contributions to sound-speed variations in the MIZ.

The organization of this paper is as follows. Section B describes the CANAPE experiment and the observations. Frequency spectra of internal waves and sound speed variability are presented in Section C, while vertical scales of variability are addressed in Section D. Section E concludes with a summary and discussion.

B. THE EXPERIMENT

In the summer of 2015, field program was carried out in the southern Beaufort Sea to study long-range acoustic propagation and ambient noise in the deep basin. The fieldwork, carried out on the *R/V Sikuliaq*, was conducted as a pilot study for the Canada Basin Acoustic Propagation Experiment (CANAPE) to be done in 2016 and 2017 in the same region. As part of the 2015 pilot study, ocean features such as eddies, internal tides, random internal waves, and spicy thermohaline structure were observed as part of the time-evolving and spatially-variable ocean sound-speed field. Using these detailed mooring data, acoustic transmission data could then be interpreted. This experiment is similar to those conducted by Colosi et al. (2012) and Colosi et al. (2013).

1. Observations

In the CANAPE pilot study, a 60-hydrophone vertical acoustic receiver array termed the Distributed Vertical Line Array (DVLA) was instrumented with 24 Sea-Bird Electronics models SBE 37-SMP and SBE 37-SM MicroCAT conductivity, temperature,

depth (CTD) instruments and two Teledyne RDI ADCPs. This mooring collected acoustic and oceanographic data from 30 July through 16 August 2015. The DVLA was located at $73^{\circ} 10.6691'N$, $154^{\circ} 06.0565'W$, and the water depth was 3853 m. The CTD instrumentation on the DVLA (Table 2.1) were densely arranged in the depth range between 85 and 550m and made measurements every 30 seconds. The pumped instruments in the upper part of the water column provided the highest quality data. These observations were used to track isopycnal vertical displacements that we denote by the symbol $\xi(\vec{r},t)$. Vertical displacements perturb the background ocean sound-speed field according to the relation

$$\delta c(\vec{r},t) = \xi(\vec{r},t) \left(\frac{dc}{dz} \right)_p (z) \quad (2.1)$$

where the potential sound speed gradient, $(dc/dz)_p$, is the important quantity due to the adiabaticity of most ocean processes, including internal waves (Colosi 2016; Flatte et al. 1979). Variations in T and S *along* isopycnals, called spice, create fluctuations in the sound speed, since density-compensating anomalies in T and S are reinforcing in sound speed (Dzieciuch et al. 2004).

In addition to the CTD sensors, two ADCPs were included on the DVLA mooring (Table 2.1). These were both placed at approximately 630 m, one looking up and the other looking down, giving an observation depth range of roughly 100 to 900 m. The ADCPs resolved horizontal currents induced by eddies, inertial waves, and internal tides. Because of the weakness of the internal wave field, the ADCP observations were too noisy to be useful and therefore will not be analyzed here.

Table 2.1. Oceanographic Instrumentation for the DVLA Mooring with Approximate Depth of Each Instrument

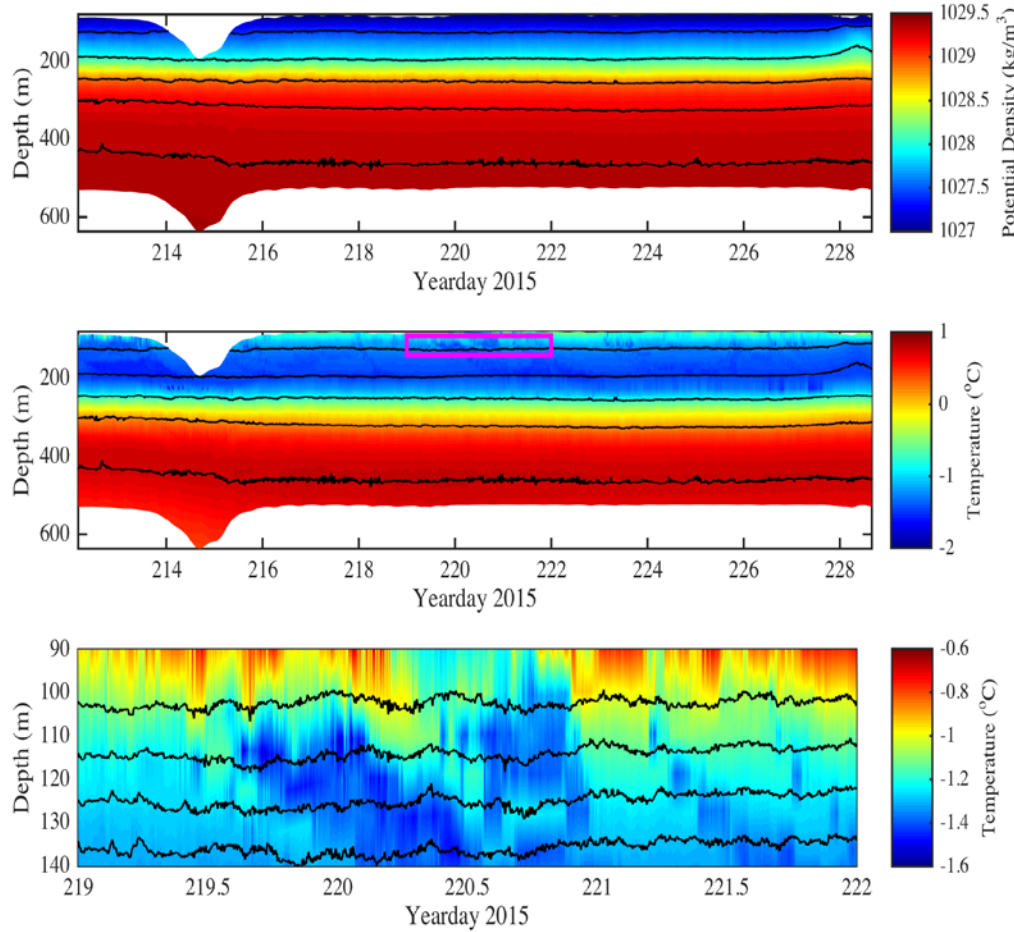
| Depth (m) | Instrument ¹ |
|-----------|---|
| 82 | SBE 37-SMP |
| 102 | SBE 37-SMP |
| 111 | SBE 37-SMP |
| 120 | SBE 37-SMP |
| 129 | SBE 37-SMP |
| 138 | SBE 37-SMP |
| 147 | SBE 37-SMP |
| 156 | SBE 37-SMP |
| 165 | SBE 37-SMP |
| 175 | SBE 37-SMP |
| 183 | SBE 37-SMP |
| 192 | SBE 37-SMP |
| 210 | SBE 37-SMP |
| 228 | SBE 37-SMP |
| 247 | SBE 37-SMP |
| 265 | SBE 37-SMP |
| 292 | SBE 37-SMP |
| 320 | SBE 37-SMP |
| 347 | SBE 37-SMP |
| 381 | SBE 37-SM |
| 418 | SBE 37-SM |
| 452 | SBE 37-SM |
| 489 | SBE 37-SM |
| 525 | SBE 37-SM |
| 628 | Teledyne RDI 75 kHz ADCP upward looking ² |
| 641 | Teledyne RDI 150 kHz ADCP downward looking ² |

¹The primary instruments are Sea-Bird Electronics models SBE37-SM and SBE37-SMP (pumped) MicroCAT CTD instruments. The SBE instruments sampled the ocean at 30 sec intervals.

²The Teledyne RDI 75 kHz ADCP was deployed in the up looking direction and the Teledyne RDI 150 kHz ADCP was deployed in the down looking direction.

Depth time series of potential density referenced to the 300 dbar level and potential temperature are displayed in Figure 2.2, showing the variability observed over the whole two weeks of the experiment. A striking feature of this display is the large

mooring “pull-down” event between 01 and 03 August that is likely due to a strong eddy moving over the mooring.¹ Another eddy event of a different nature is seen towards the end of the observation period. Because this study is not concerned with eddies, the analysis focuses on the time period 04–15 August (yearday 216 to 228).

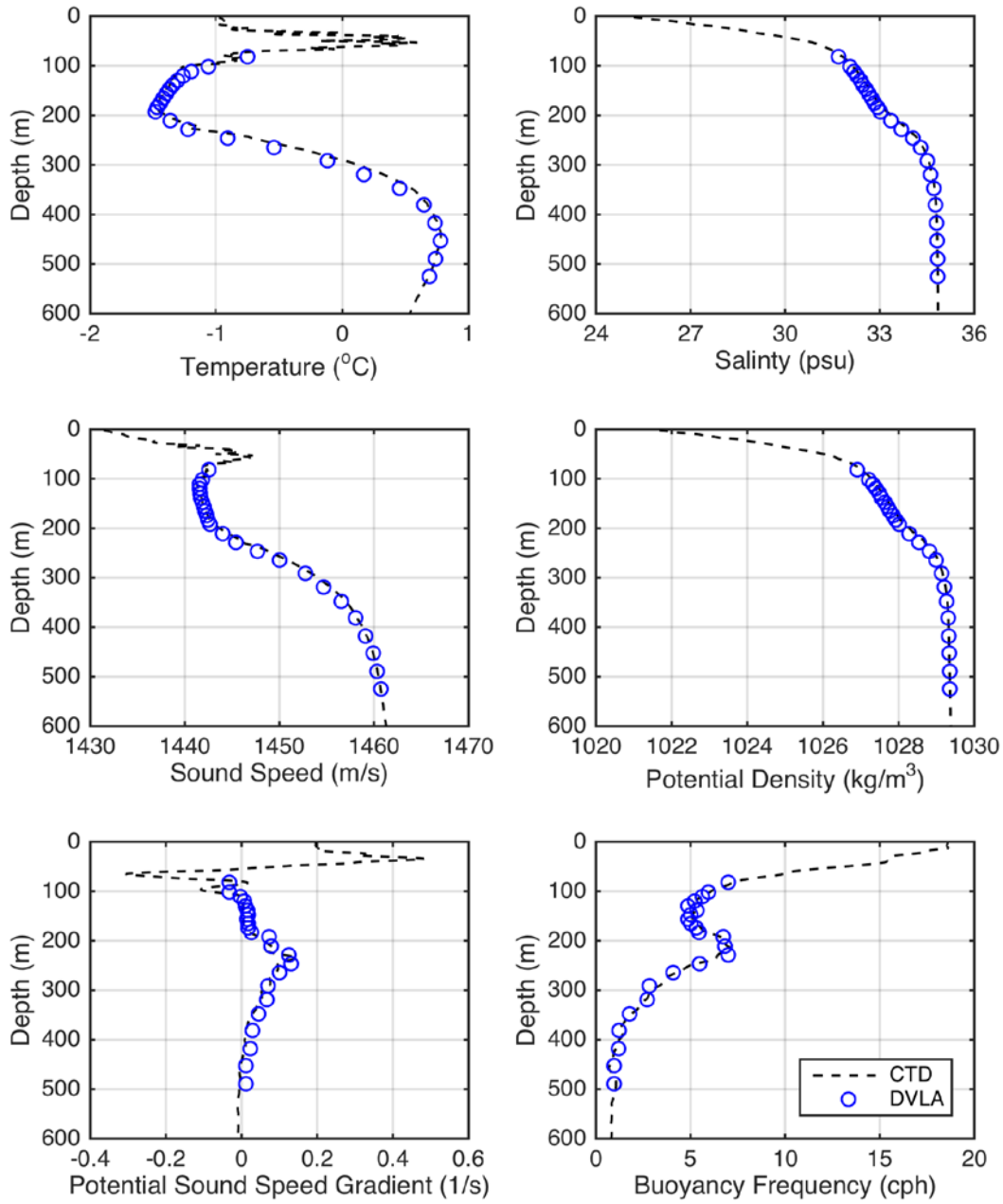


Potential density in kg/m^3 (top) and temperature in degrees Celsius (middle and bottom) as a function of depth (m) and time (yearday), measured at the DVLA mooring. Lines of constant potential density (isopycnals) are overlaid in black. The bottom panel shows an expanded view of the area highlighted in the middle panel.

Figure 2.2. Depth-Time Series of Potential Density and Temperature.

¹ The eddy is clearly seen in the ADCP observations with currents of +/- 20 cm/s, and is located in the Atlantic layer.

Figure 2.3 shows mean profiles over this shortened timeframe for several quantities of oceanographic and acoustical interest, including T, S, sound speed, potential sound speed gradient, potential density, and buoyancy frequency. These mean profiles were derived from the moored observations and three shipboard CTD casts taken within 75 km of the DVLA. In the upper 600 m there are four distinct water masses. The upper 40 m is characterized by low salinity with values less than 30 psu, and a temperature near -1°C . Below this surface layer is the PSW, a thin layer (about 30 m thick) with salinities between 30 and 32 psu and relatively warm temperatures between 0 and 1°C . Between 100 and 200 m the PWW is cooler with temperatures below -1°C and salinities between 32 and 33 psu. Below 200 m a thermocline and halocline separate the Pacific-origin waters from Atlantic-origin waters, the core of which is found below 300 m. The Atlantic Water (AW) has a much higher temperature ($> 0^{\circ}\text{C}$) than the overlying Pacific waters, but its high salinity of about 34.8 psu results in a relatively high density. These water masses are highly stratified, with buoyancy frequencies of around 15 cycles per hour (cph) in the upper 100 m and 7 cph at 250 m. These depths correspond to the upper limit of PSW and lower limit of PWW.



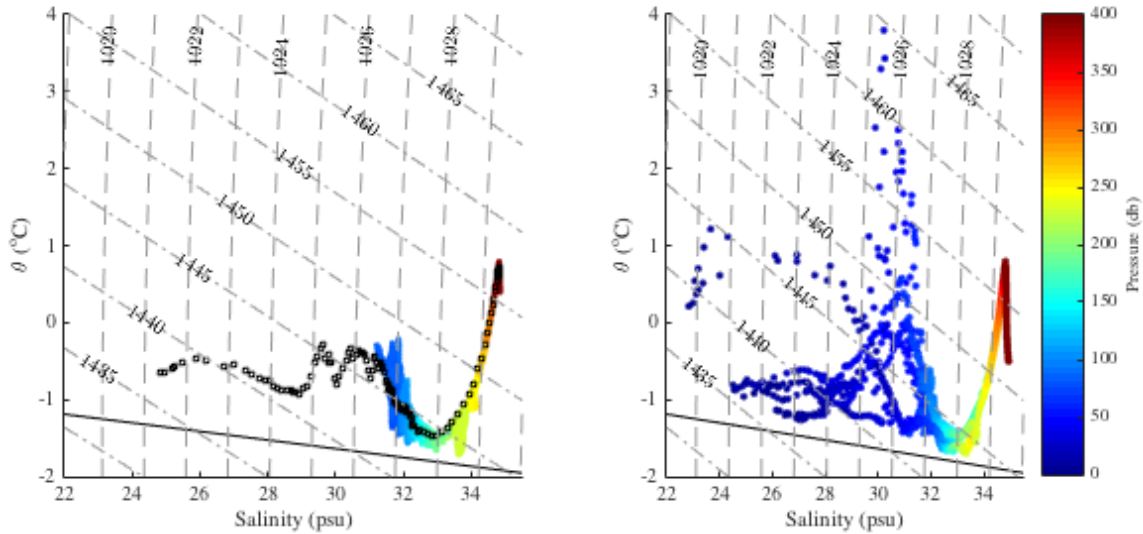
Values derived from the DVLA are shown with circles. Average profiles derived from 3 CTD casts made in the vicinity of the DVLA are shown with dashed lines. Analysis methods used to produce these figures are adapted from Colosi et al. (2013, 2014).

Figure 2.3. Mean Profiles of Temperature, Salinity, Sound Speed, Buoyancy Frequency, Potential Density, and Potential Sound Speed Gradient.

Relevant to ocean acoustics is the vertical structure of the mean sound speed and potential sound speed gradient profiles. With regards to sound speed, the expected upward refracting surface duct formed by the thermocline is seen, but quite unexpectedly there is a local minimum in sound speed at roughly 120-m depth forming a weak subsurface acoustic duct extending roughly from 75-m to 225-m depth. Sound energy trapped in this duct would experience limited loss because it does not interact with the ocean surface. Furthermore, the potential sound speed gradient in this subsurface duct is quite small, meaning that internal-wave-induced sound speed fluctuations are diminished (eq. 2.1). Thus, there is the potential for unprecedented long range, stable propagation in the Arctic.

It is worth pointing out that the shallowest instrument on the DVLA was at 85 m and cannot observe the surface layer or the core of the PSW. Therefore, the temporal variability discussed in this paper will be restricted to PWW, AW, and the pycnocline between them.

At these low temperatures, density is determined primarily by salinity, so relatively large changes in temperature can be dynamically compensated by very small changes in salinity. This fact is evidenced by variations in temperature along the first isopycnal overlaid on the temperature time series in Figure 2.2 (bottom), especially above 200 m. These variations in isopycnal temperature have significance for spicily sound-speed variability, as density-compensating changes in temperature and salinity are reinforcing in sound speed. When plotted on a T-S diagram, the isopycnal sound-speed variability is readily apparent (Figure 2.4). Temperature variations in the salinity range above 33.5 psu lay roughly along the density contours, but result in a change in sound speed of up to 5 m/s at the DVLA (Figure 2.4, left panel) and 25 m/s across the 8 CTDs (Figure 2.4, right panel). The highest variability is associated with Pacific Summer Water.



The color of each data point indicates the depth of the observation. The dashed lines are contours of constant potential density measured in kg/m^3 ; the dot-dashed lines are contours of constant sound measured in m/s ; and the solid line is the freezing temperature as a function of salinity. The average CTD temperature and salinity is plotted as black squares for comparison on the left panel.

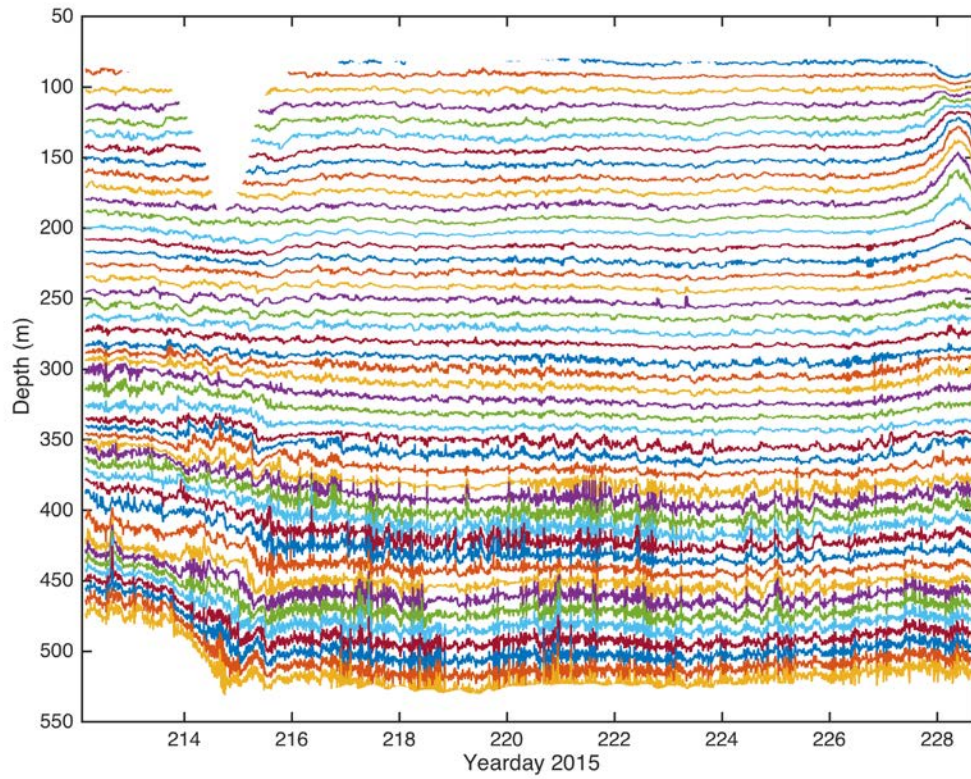
Figure 2.4. Potential Temperature Plotted as a Function of Salinity as Measured by the DVLA Mooring (left) and Ship CTDs (right).

2. Displacement and Spice Analysis

The methods used to analyze isopycnal displacement and spicy sound-speed variability are similar to those used in Colosi et al. (2012, 2013). The description of methods presented here will be terse. The reader is encouraged to review Colosi et al. (2012) for a more thorough discussion.

From the moored CTD observations, potential density referenced to the 300 decibar (dbar) level (Talley et al. 2011) was computed as a function of instrument depth, $z(t)$, and time; we denote this quantity as $\sigma_{300}(z(t), t)$. Instrument depth here is a function of time due to mooring motion. The depths of 45 isopycnals, $z(t, \sigma_{300})$, between 1026.90 and 1029.36 kg/m^3 were tracked using depth-linear interpolation, and the specific isopycnals were chosen to give roughly 10-m vertical separation (Figure 2.5). The advantages and limitations of this technique are discussed in Colosi et al. (2012), and uncertainties associated with this calculation are discussed below. There are several

noteworthy aspects of the isopycnal depth time series shown in Figure 2.5. First are the energetic deep eddy pull-down event early in the record and the appearance of another weaker near surface eddy at the end of the record. The increased high frequency variability at depths below 350 m is an artifact of the non-pumped moored CTD instruments on that section that have a lower sensitivity to changing salinity. The small-amplitude displacement variability is on a super-inertial time scale and falls in the realm of internal waves. A spectral analysis of this variability will be presented in Section C.



Isopycnals are roughly separated by 10-m on average. Analysis methods used to produce these figures are adapted from Colosi et al. (2013, 2014).

Figure 2.5. Depth of 45 Tracked Isopycnals as a Function of Time in the Upper 550 m at the DVLA Mooring.

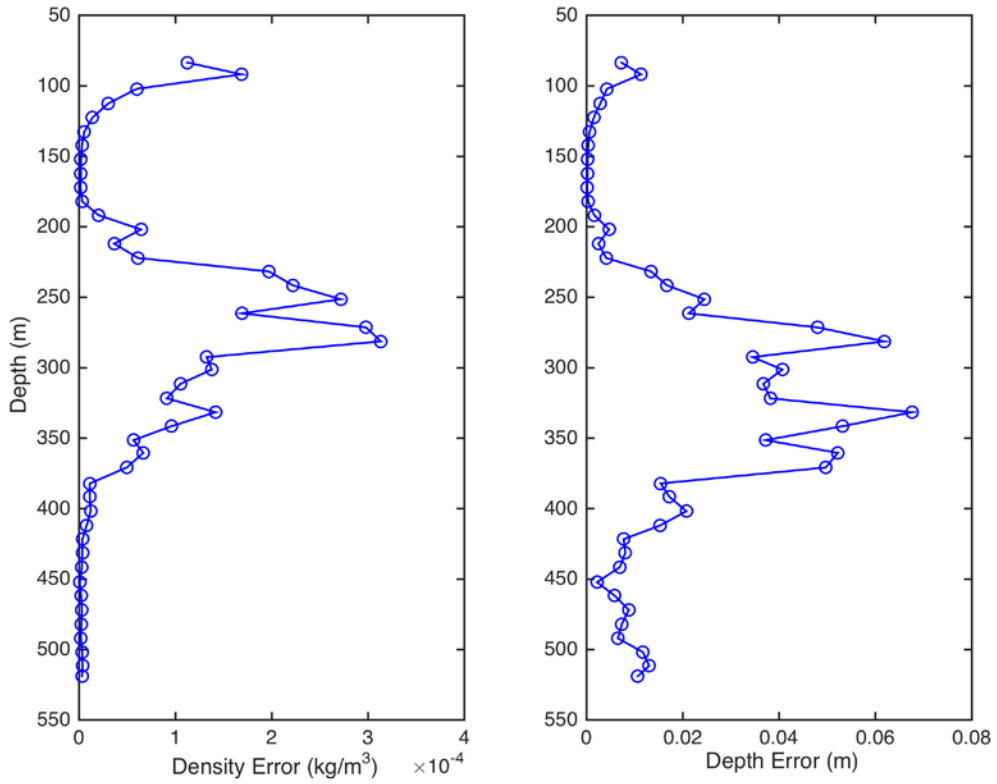
To address the issue of spice, for each isopycnal, potential temperature, θ , and salinity, S , were computed using depth-linear interpolation. The along isopycnal temperature and salinity were then used at the mean isopycnal depth to

compute sound speed, $c(t, \sigma_{300})$. This sound speed field holds the mean profile plus spiciness fluctuations. Sound speed variability caused by the fluctuations in isopycnal vertical displacements, like those caused by internal waves, will be discussed later. To verify the validity of this linear interpolation scheme, the errors in isopycnal tracking were determined by recomputing potential density from the interpolated potential temperature, $\theta_{300}(t, \sigma_{300})$, and salinity, $S(t, \sigma_{300})$. The root mean square (RMS) differences between the recomputed and original densities and associated depth errors are listed in Table 2.2, columns 5 and 6 (also Figure 2.6). The errors from using linear interpolation are much smaller than those found in the Philippine Sea (Colosi et al. 2013) and New Jersey Continental Shelf (Colosi et al. 2012) experiments. This is likely due to the relatively quiescent nature of the Beaufort Sea when compared to the more dynamically active regions of those studies. The largest errors in isopycnal tracking are found between 200 and 400 m deep (Figure 2.6.) Thermohaline staircases of order 1 m in vertical height created by double diffusion are often found in this depth range (Padman and Dillon 1987; Timmermans et al. 2008) and may explain the enhanced error in linear interpolation.

Table 2.2. Observed Isopycnal Statistics for Tracked Isopycnals¹

| σ_{300} (kg/m ³) | $\langle z \rangle$ (m) | $\langle \theta_{300} \rangle$ (°C) | $\langle S \rangle$ (psu) | $\delta\sigma_{300}$ (x10 ⁻⁶ kg/m ³) | $\delta\sigma_{300} \left(\frac{\delta\sigma_{300}}{dz} \right)$ (x10 ⁻⁴ m) | $\delta\theta_{rms}$ (x10 ⁻⁵ °C) | δS_{rms} (x10 ⁻⁷ psu) | δc_{rms} (x10 ⁻⁴ m/s) |
|--|----------------------------|--|------------------------------|--|--|--|---|---|
| 1027.058 | 91.8 | -0.90 | 31.87 | 168 | 113 | 219 | 56 | 504 |
| 1027.324 | 112.4 | -1.22 | 32.19 | 30 | 29 | 121 | 25 | 282 |
| 1027.507 | 132.7 | -1.32 | 32.41 | 5 | 7 | 29 | 6 | 67 |
| 1027.673 | 152.1 | -1.39 | 32.61 | 2 | 2 | 19 | 4 | 43 |
| 1027.829 | 172.1 | -1.45 | 32.8 | 2 | 2 | 18 | 4 | 43 |
| 1028.010 | 191.7 | -1.48 | 33.02 | 20 | 16 | 18 | 4 | 42 |
| 1028.296 | 212.0 | -1.36 | 33.38 | 36 | 25 | 32 | 7 | 74 |
| 1028.594 | 231.7 | -1.17 | 33.76 | 197 | 134 | 103 | 27 | 239 |
| 1028.872 | 251.4 | -0.80 | 34.13 | 272 | 245 | 38 | 14 | 86 |
| 1029.031 | 271.3 | -0.43 | 34.35 | 298 | 479 | 5 | 3 | 11 |
| 1029.136 | 292.5 | -0.11 | 34.50 | 132 | 345 | 4 | 3 | 9 |
| 1029.186 | 311.4 | 0.09 | 34.58 | 105 | 367 | 3 | 2 | 6 |
| 1029.235 | 331.6 | 0.29 | 34.66 | 142 | 676 | 2 | 1 | 3 |
| 1029.276 | 351.4 | 0.48 | 34.72 | 57 | 372 | 3 | 2 | 6 |
| 1029.296 | 370.8 | 0.59 | 34.76 | 50 | 497 | 5 | 4 | 12 |
| 1029.311 | 391.6 | 0.67 | 34.78 | 11 | 172 | 6 | 4 | 12 |
| 1029.320 | 412.0 | 0.71 | 34.80 | 8 | 152 | 6 | 4 | 13 |
| 1029.329 | 431.4 | 0.75 | 34.81 | 3 | 81 | 2 | 2 | 5 |
| 1029.339 | 452.2 | 0.76 | 34.83 | 1 | 22 | 1 | 1 | 3 |
| 1029.345 | 471.8 | 0.74 | 34.83 | 3 | 88 | 1 | 1 | 2 |
| 1029.350 | 492.0 | 0.72 | 34.84 | 2 | 65 | 1 | 1 | 2 |

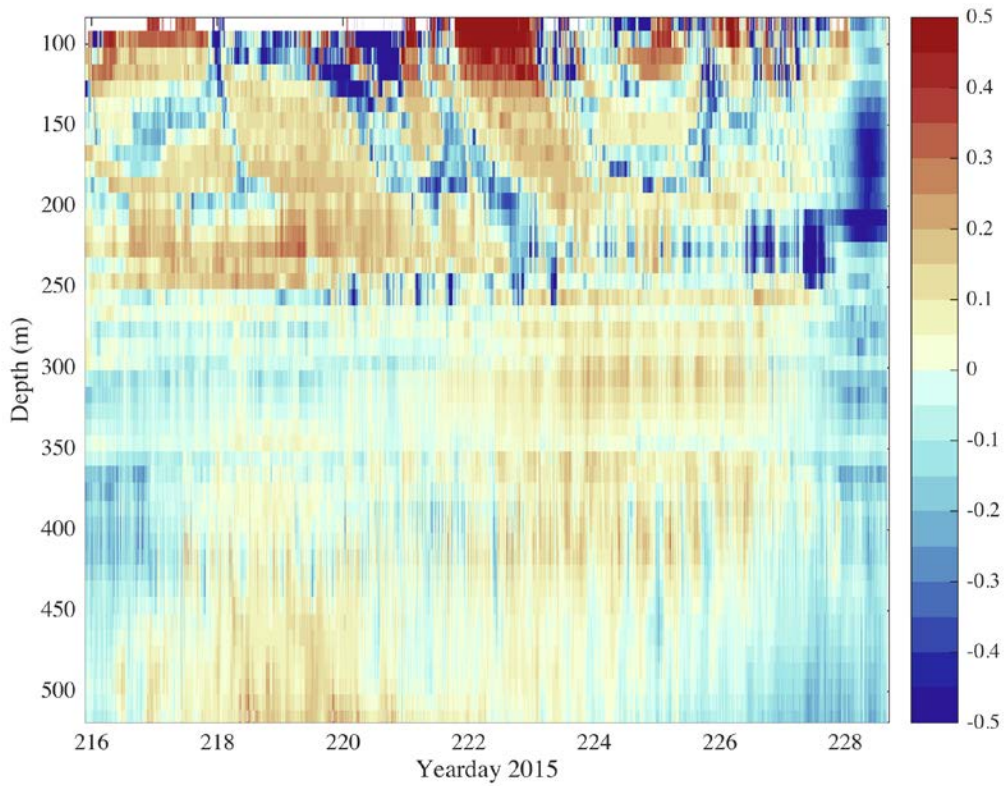
¹Selected isopycnal densities are listed in the first column, and the second, third, and fourth columns list the mean isopycnal depth, potential temperature, and salinity. The fifth and six columns list the RMS errors in isopycnal density and depth tracking (see text for discussion). The seventh, eighth, and ninth columns list the RMS spicy sound speed variations along the selected isopycnals for temperature, salinity, and sound speed. These last three statistics only include contributions from frequencies between the Coriolis frequency, f, and a typical value of buoyancy frequency, N. For brevity, only every other isopycnal is displayed here.



Analysis methods used to produce these figures are adapted from Colosi et al. (2013, 2014).

Figure 2.6. Root Mean Square Error in Tracking Isopycnal Density (left) and Depth (right).

The time-mean sound speed profile was subtracted from the sound speed field, $c(t, \sigma_{300})$, to give the spicy sound speed fluctuations (Figure 2.7). Variations of over 1 m/s were observed in the upper 250 m, with the strongest variations in the upper 150 m. The advection pattern of the passive spicy features past the mooring is complicated showing both large and small-scale variability. The spice is seen to weaken considerably below 250 m, which coincides with the local maximum in buoyancy frequency.



Spicy isopycnal sound speed anomalies, measured in m/s, are plotted as a function of depth and time, as measured at the DVLA mooring.

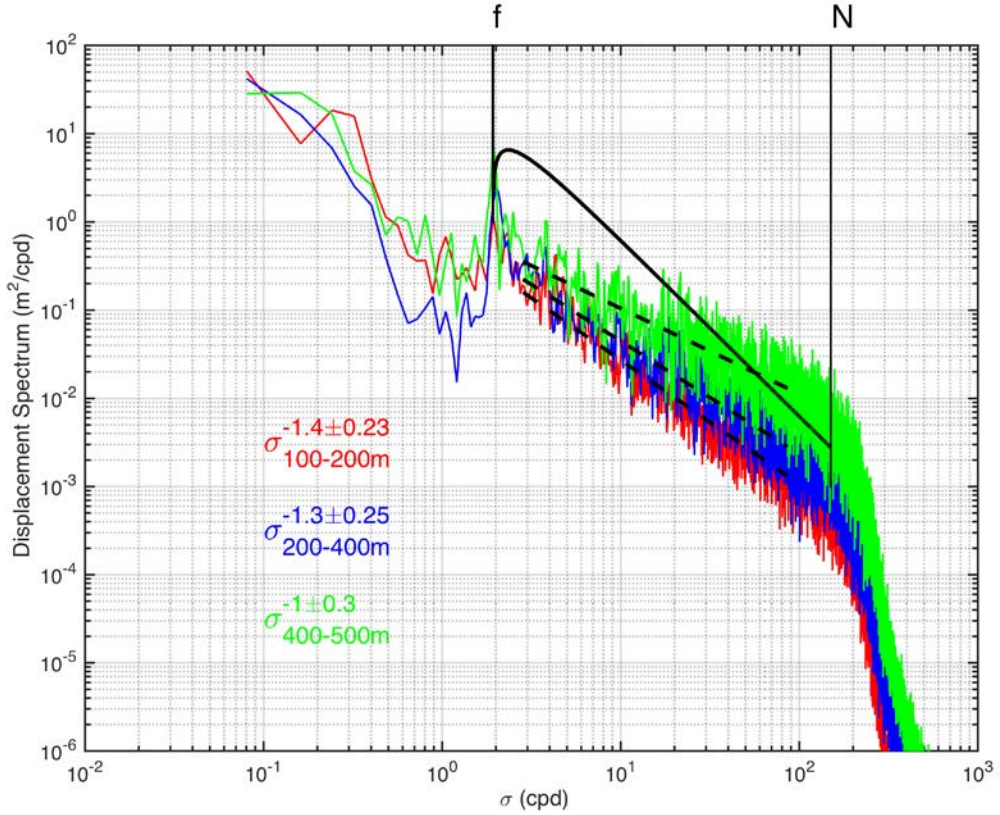
Figure 2.7. Depth-Time Series of Spicy Isopycnal Sound Speed Anomalies.

C. FREQUENCY SPECTRA AND ANALYSIS OF VARIANCE

In this section, frequency spectra of displacement and spice variability will be analyzed as a function of depth. Spectral shape and depth inhomogeneity of internal wave and spice induced sound speed fluctuations play a major role in acoustic scattering theory (Colosi 2016). For internal waves the GM spectrum has played a major role in bringing together theory and observation for many mid-latitude experiments, but the acoustics community lacks a similar canonical model for spice

1. Internal Waves

The time series of isopycnal displacements were filtered with a 4-pole Butterworth digital filter prior to spectral analysis to remove signals with frequencies over 20 cph. The full record length of just over 17 days was reduced to 12.4 days to remove data from the mooring pull-down event and to produce a record length of 24 cycles of the M_2 tides. After applying a Hanning window, power spectral density (PSD) estimates were computed for each tracked isopycnal, denoted by $S_\xi(\omega, \bar{z}(\sigma_{300}))$, where $\bar{z}(\sigma_{300})$ is the mean depth of the isopycnal, σ_{300} . Figure 2.8 shows the depth-averaged PSD estimates for displacements in three depth bands: shallow (100-200 m), mid (200-400 m), and deep (400-500 m). There is decreased energy just below the inertial frequency, followed by increasing low frequency energy associated with the eddy field (spectral gap). At the highest frequencies energy drops off rapidly above the buoyancy frequency cutoff (mostly due to the filter). A spectral peak exists near the inertial frequency. This peak is associated with the nearby M_2 and S_2 internal tides evident in the horizontal current spectra (not shown). In the continuum band between roughly 3 to 40 cycles per day (cpd), a power law shape is seen with spectral slopes of $p = -1.4 \pm 0.23$ for the depth band of 100–200m, $p = -1.3 \pm 0.25$ for 200–400m, and $p = -1.0 \pm 0.30$ for 400–500m. The deepest spectra show noise problems at high frequency due to the non-pumped sensors. However, in general the observed spectra have a much flatter shape than the GM spectrum, which goes as frequency to the minus two power. Levine et al. (1987) observed internal wave spectra in the Beaufort Sea under pack ice with slope closer to -1.

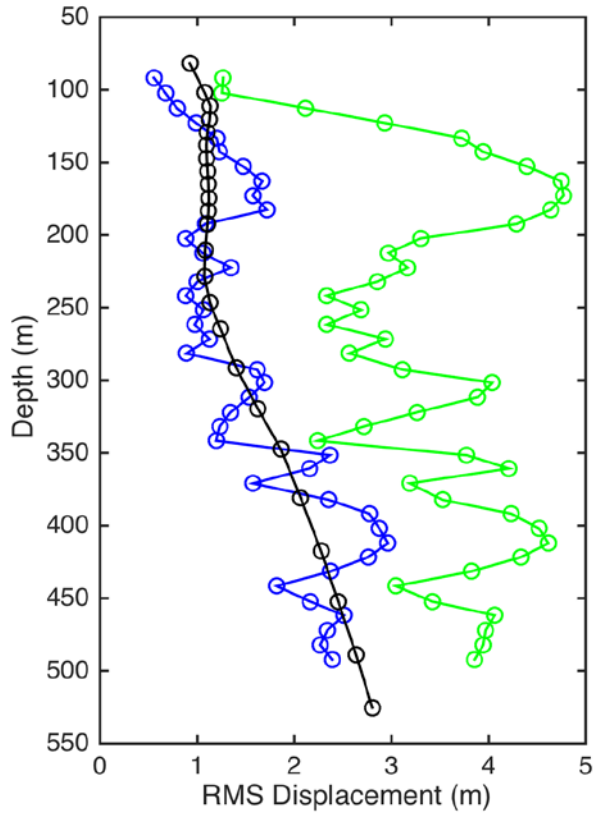


The three depth bands are 100–200 m (red), 200–400 m (blue), and 400–500 m (green.) The Coriolis frequency, f , and typical buoyancy frequency, N , are indicated with solid vertical lines. Power-law fits (dashed lines) to the random internal wave band of frequencies give the exponents listed. For comparison, the thick black line depicts the GM spectrum at standard energy. Analysis methods used to produce these figures are adapted from Colosi et al. (2013, 2014).

Figure 2.8. Frequency Spectra of Displacement Averaged in Three Depth Bands.

The strength of internal wave displacement fluctuations depends on depth; in particular, it depends on the stratification, $N(z)$. Here we will use RMS displacement to quantify the isopycnal depth fluctuations (Figure 2.9). Vertical covariances and spectra will be discussed in Section D. The RMS displacement in the internal wave band is seen to be between 1 and 3 m, increasing with depth. This result is consistent with the Wentzel-Kramers-Brilloiun (WKB) depth scaling relation $\langle \xi^2 \rangle^{1/2} = \xi_o \sqrt{\left(N_o / N(z) \right)}$ (Munk 1981) using a reference internal wave displacement $\xi_o = 1.5$ m, $N_o = 3$ cph, and the

mean $N(z)$ from the mooring (see Figure 2.3.) The observed internal wave reference displacement is roughly 20% of the standard GM level of $\xi_0 = 7.3$ m. The effectiveness of the WKB relation implies that there is a rich internal wave vertical spectrum, and that the field is not dominated by a few low order modes. The one eddy event at the end of the record contributes a significant amount of variability to the total RMS displacement. (Note our analysis does not include the large eddy event at the beginning of the record.)

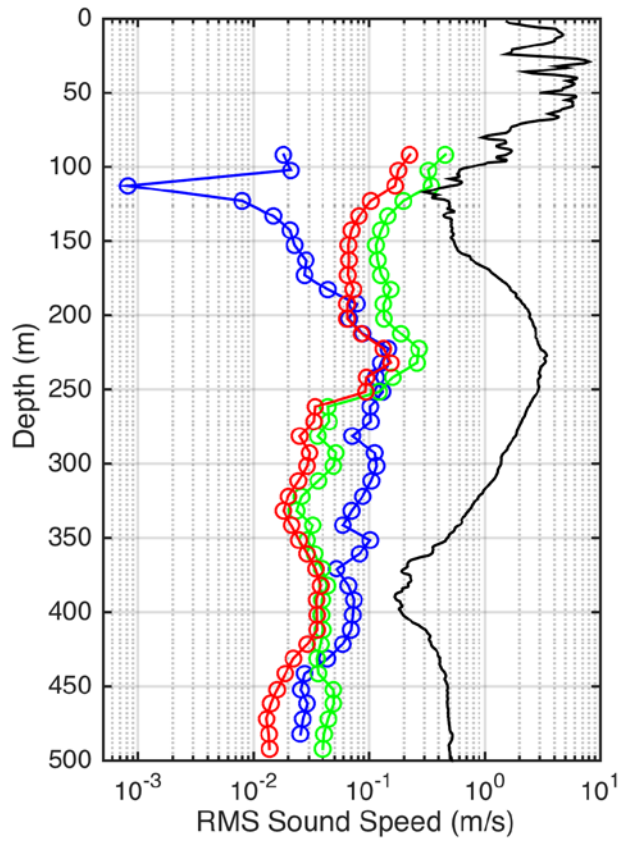


The total RMS displacement is plotted in green, RMS displacement in the internal wave frequency band (f to N) is drawn in blue, and the WKB estimate using a reference internal wave displacement ξ_0 of 1.5 m is drawn in black. Analysis methods used to produce these figures are adapted from Colosi et al. (2013, 2014).

Figure 2.9. RMS Displacement of Isopycnals Versus Depth. Sound Speed Variability and Spice

2. Spice

The mean sound speed profile shown in Figure 2.3 is continuously perturbed by isopycnal displacement as well as spicy sound-speed variability. Vertical isopycnal displacements cause sound-speed perturbations by vertically advecting the background sound speed structure. Using Eq. 2.1, the RMS sound speed perturbations can be approximated by multiplying the potential sound speed gradient (Figure 2.3, bottom left) by the RMS displacement of isopycnals (Figure 2.9). The total and internal-wave band RMS sound speed fluctuation from spice are computed from the observations in Figure 2.7, and the result is shown in Figure 2.10. Spice is indeed seen to drop off markedly below 250-m depth. Spice is expected to be the larger contributor to sound speed variability from the surface to 200-m depth, while internal waves provide the larger contribution below 200 m. Both the internal wave and spice sound speed fluctuations are small compared to mid-latitude observations (Colosi et al. 2012; Colosi et al. 2013). These variations are all small compared to the differences observed between CTD locations. Plotted in black in Figure 2.10, the RMS differences between the eight CTDs are roughly an order of magnitude larger than the temporal variations observed at the mooring, and the largest variations are found in the upper 100 m. The ship CTD RMS is clearly large because it includes the energetic eddy field in addition to spice and internal waves.

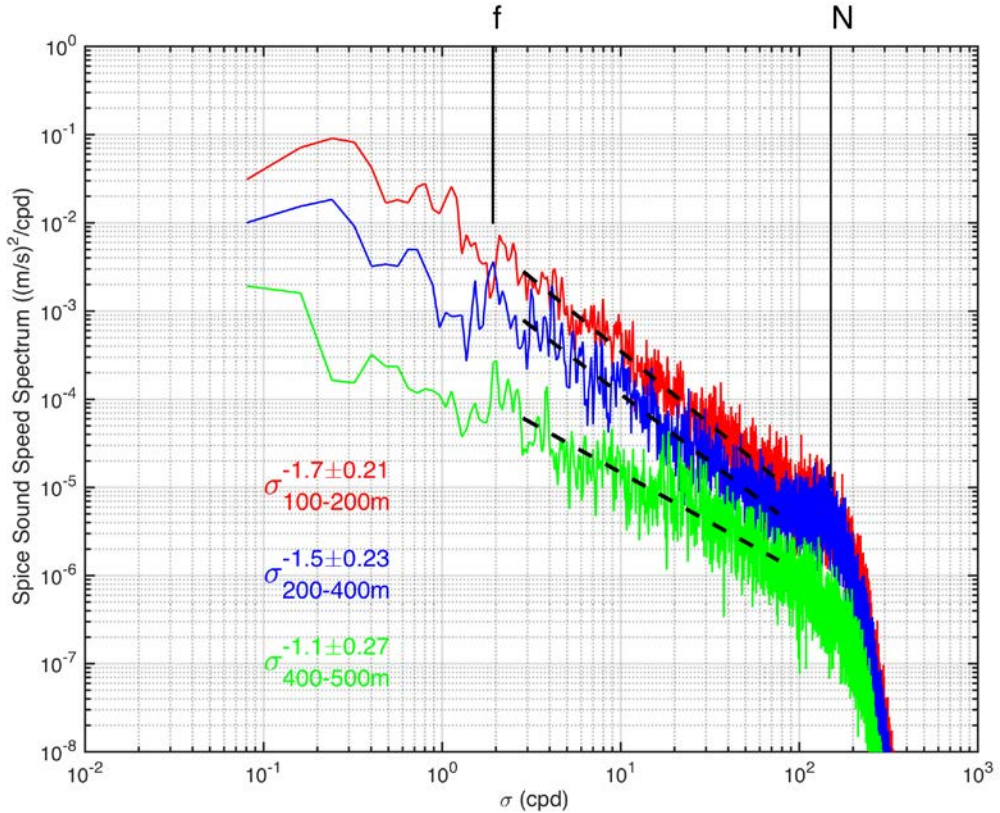


Total sound-speed fluctuations are plotted in green, fluctuations due to spice in the internal wave band are plotted in red, and fluctuations due to internal wave displacements are plotted in blue. The RMS sound speed variation among CTD locations is plotted in black. Note the sound speed axis is a logarithmic scale. Analysis methods used to produce these figures are adapted from Colosi et al. (2013, 2014).

Figure 2.10. Root Mean Square Sound Speed Fluctuations Versus Depth.

Spectra of spice sound-speed fluctuations were computed using the same methodology as the displacement spectra, and the depth-averaged results are shown in Figure 2.11. These spectra do not show a peak near the inertial/semi-diurnal frequencies. Power-law fits in the frequency band between 3 and 40 cpd result in exponents of -1.4 ± 0.21 for 100 - 200 m, -1.5 ± 0.23 for 200 - 400 m, and -1.1 ± 0.27 for 400 - 500 m. These results are similar to what was found in the Philippine Sea and New Jersey shelf experiments (Colosi et al. 2012; Colosi et al. 2013), including the decrease in spectral energy with depth, but in these mid-latitude cases the spectral slopes were larger. The

relative similarity of the spice spectral slopes to the internal wave slopes is an indication that internal wave currents are a source of spice advection. The higher slopes in the shallower depth band indicate front-like features, which have a slope of -2 (Ferrari and Rudnick 2000), and the spectra flatten with depth to be more noise-like, though these deep variations are likely at the threshold of our measuring ability, especially with the non-pumped instruments.



The three depth bands are 100–200 m (red), 200–400 m (blue), and 400–500 m (green). Power law fits to the spectra in the frequency range of 3 to 40 cpd are shown (dash). The Coriolis frequency, f , and a typical buoyancy frequency, N , are indicated for reference. Analysis methods used to produce these figures are adapted from Colosi et al. (2013, 2014).

Figure 2.11. Frequency Spectra of Sound Speed Fluctuations along Isopycnals (Spice) Averaged Over Three Depth Bands.

D. VERTICAL SCALES OF VARIABILITY

The vertical spatial variability of internal waves and spice is now addressed. For internal waves both correlation functions and WKB stretched vertical wave number spectra are presented. For spice there is no method for handling the depth non-stationarity, and so only correlation functions are analyzed.

1. Internal Waves

Figure 2.12 shows the internal-wave displacement depth-covariance matrix normalized by the individual variances at each depth, as well as the depth-averaged correlation function. To remove depth non-stationarity, the displacement observations are WKB stretched and normalized using a reference buoyancy frequency of 3 cph and a reference displacement of $\xi_o = 1.5\text{m}$ (see Figure 2.9). Displacement correlation decreases rapidly with depth lag, with a typical scale of tens of meters, indicating that the vertical mode structure of the internal wave field is rich in high modes. The slight increase in correlation lengths near 250 m indicates that the halocline just above the AW is perturbed without significantly changing shape; i.e., the halocline as a whole is lifted or depressed.

The GM spectrum is of the form $\frac{1}{(j^2 + j_*^2)}$ where j_* is the modal bandwidth parameter, typically 3 for mid-latitude deep ocean conditions (Munk 1981). The vertical wavenumber spectrum can be computed directly from the WKB scaled displacements (Figure 2.13). The spectrum shows some deviations from the GM form with a modal bandwidth factor, j_* , close to 6 but with a steeper slope.

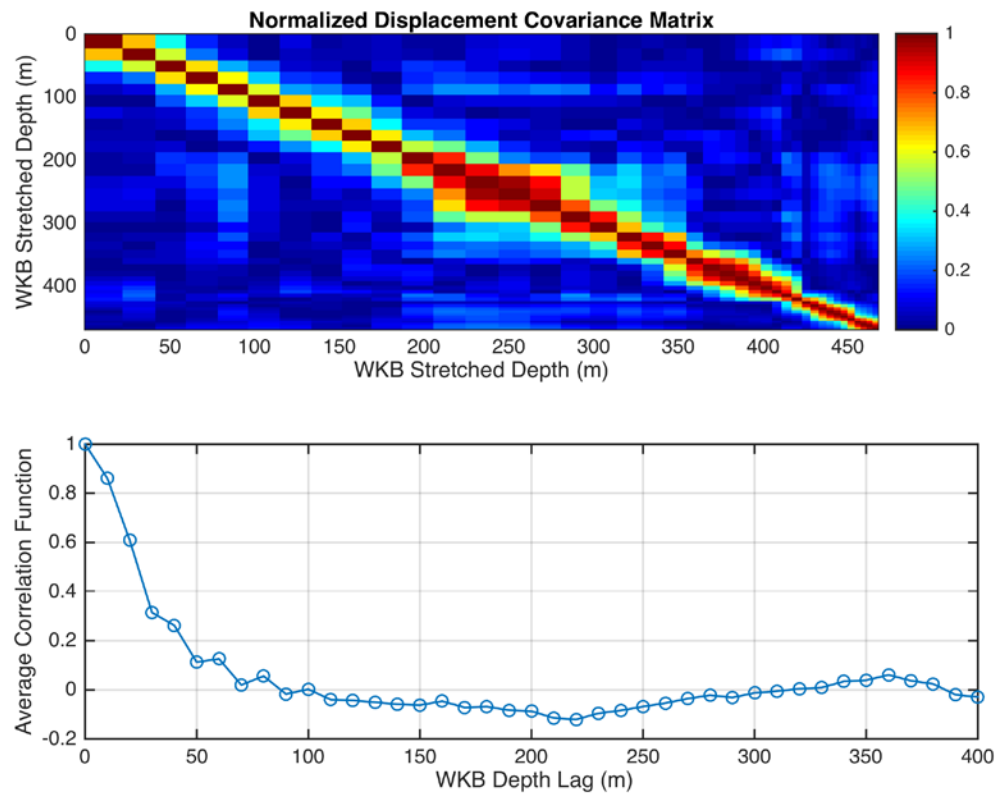
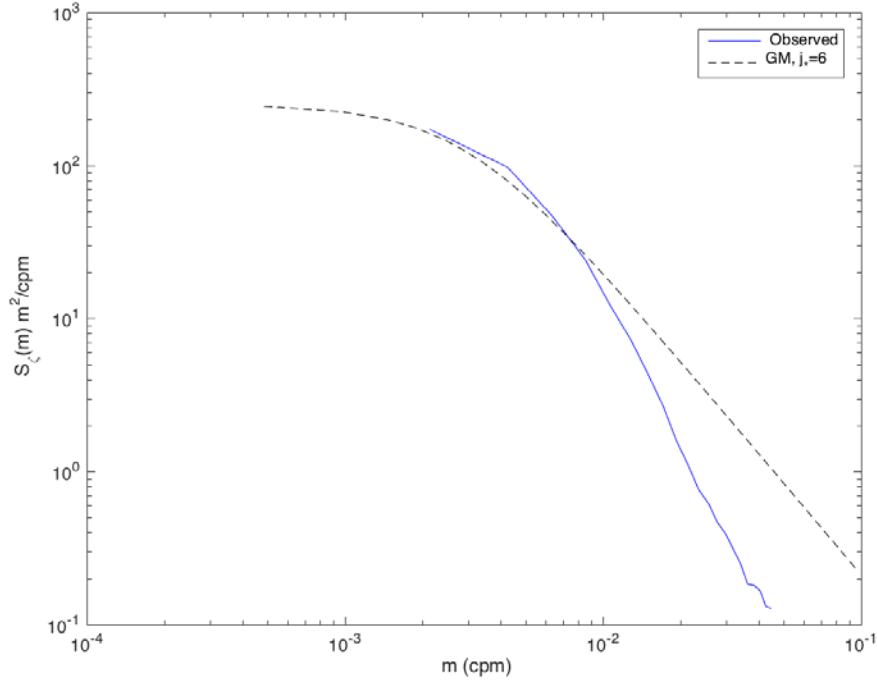


Figure 2.12. Normalized Covariance Matrix for the Internal Wave Displacements (Top), and Depth-Averaged Correlation Function as a Function of WKB Depth Lag (Bottom).



WKB stretched displacement vertical wavenumber spectrum, and the GM spectrum with $j_* = 6$.

Figure 2.13. Vertical Wavenumber Spectrum.

2. Spice

The covariance analysis discussed in the previous paragraph is applied to the spicy sound speed structure, but no WKB depth scaling is applied. The normalized spice covariance matrix and average correlation function are shown in Figure 2.14. Spice is seen to decorrelate in depth somewhat more rapidly than the internal waves, a result of the common front-like structure of spice (Ferrari and Rudnick 2000; Dzieciuch et al. 2004). The larger correlation lengths seen at the deeper depths are likely not significant because spice is so weak in these areas.

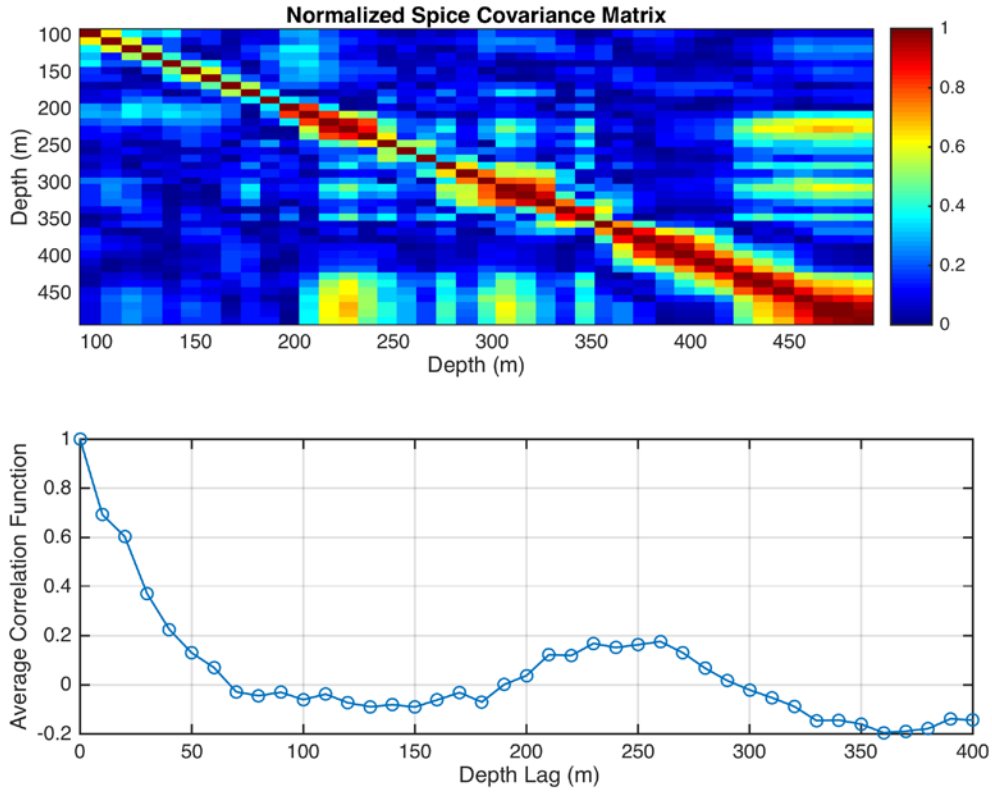


Figure 2.14. Normalized Covariance Matrix for Spicy Sound Speed Fluctuations (Top), and Average Correlation Function as a Function of Depth Lag (Bottom).

E. SUMMARY AND CONCLUSIONS

In this work the temporal and vertical scales of sound-speed fluctuations caused by internal waves and spicy thermohaline structure in the southern Beaufort Sea during the summer of 2015 have been quantified by tracking the vertical displacement of isopycnals and fluctuations of temperature and salinity along them. Large variations in temperature, especially in the upper 150 m, were observed that produce strong spicy isopycnal sound-speed anomalies. The spectral shapes of isopycnal displacements were flatter than predicted by GM theory, with power law slopes of -1.0 to -1.4. An internal wave reference displacement of 1.5 m was observed, which is roughly 20% of the GM level. Analysis of the vertical structure of internal waves showed a modal bandwidth parameter, j_* , value of 6 to 10 as opposed to the typical value of 3 for mid-latitudes. Spicy sound speed variability is also low, but accounts for significant sound speed variations in

the upper 200 m. A noteworthy feature of the vertical structure of spice is that spice features appear to be strongest near the surface and slump downwards in time (Figure 2.7). In the marginal ice zone, these spice features could be generated locally at the surface by episodic wind forcing events, or they may be advected from upstream, neither of which can be determined from this data set.

Although horizontal sampling by ship-borne CTDs was limited, a sound-speed minimum consistently appears in the PWW layer. Therefore, it is likely that some acoustic energy could become trapped in this sub-surface sound channel and suffer less attenuation due to surface scattering and absorption by sea ice. However, strong differences are found in the thermohaline and sound-speed structures between CTDs spaced less than 100 km apart, and significant temporal variability was observed in this depth range. These strong variations in vertical and horizontal sound-speed structure will have significant impacts on acoustic applications, especially in the realm of communications and sensor performance predictions. The results of this oceanographic analysis will be used to analyze and understand the acoustic data collected during the same experiment.

F. ACKNOWLEDGMENTS

This work was supported by the Office of Naval Research. The authors would also like to extend a deep gratitude to the crew of the *R/V Sikuliaq* and embarked scientists and engineers who tirelessly worked to enable this experiment.

THIS PAGE INTENTIONALLY LEFT BLANK

III. EVALUATION AND SENSITIVITY OF CLIMATE MODEL SKILL AT REPRESENTING UPPER ARCTIC OCEAN HYDROGRAPHY

This chapter was submitted to the *Journal of Climate* for publication. Except for the figure numbering, the formatting has been retained as submitted. As the main author of the work, I made the major contributions to the research and writing. Co-authors include W. Maslowski¹, R. Osinski², A. Roberts¹, and J. Clement Kinney¹.

INTRODUCTION

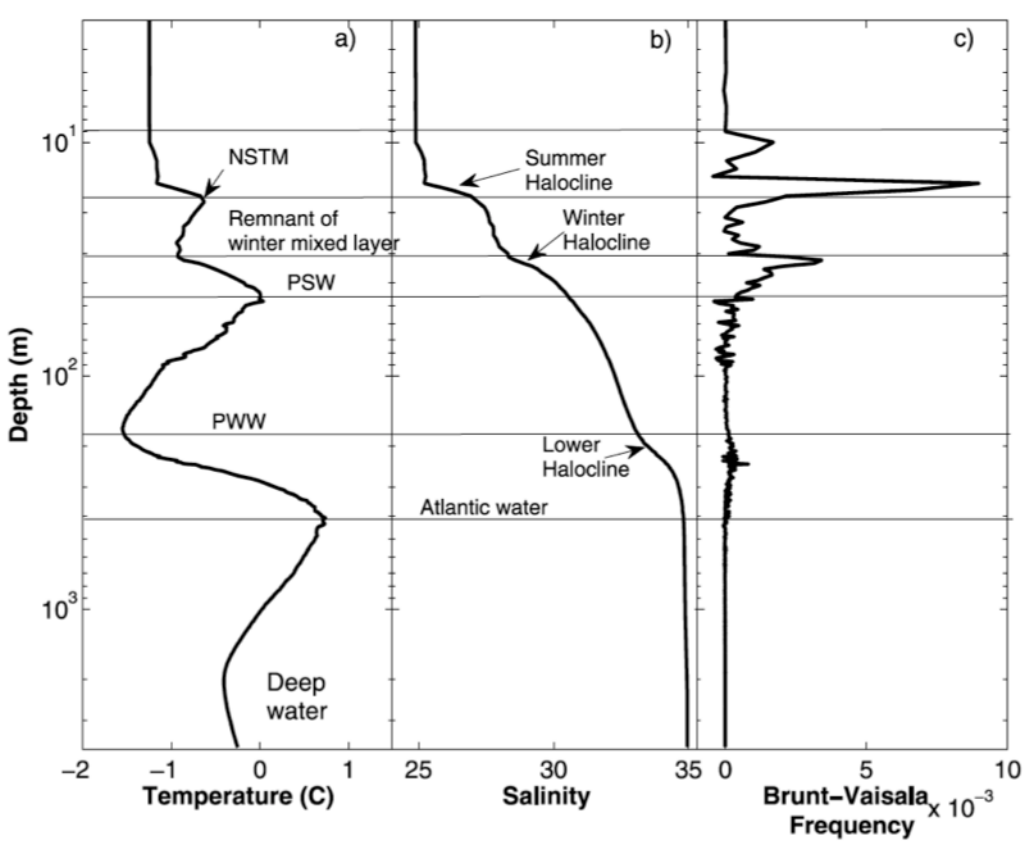
Arctic sea ice has undergone significant change in recent years. Since 1979 through 2016 the September minimum ice extent has decreased by about 13.3% per decade and reached a record minimum of 3.41 million square kilometers in 2012, almost half of the 1979–2000 average (National Snow and Ice Data Center 2016). Winter sea ice thickness decreased by 1.75 m between 1980 and 2008 (Kwok and Rothrock 2009), and satellite-derived sea ice volume decreased at a rate of around a thousand cubic kilometers per year from 1996 to 2008 (Kwok and Cunningham 2008). Model based estimates of sea ice volume have decreased at a rate of around three thousand cubic kilometers per decade since 1979, with a much steeper decline of over eleven thousand cubic kilometers per decade from the mid-1990s (Schweiger et al. 2011, Maslowski et al. 2012). Atmospheric heating may account for less than 50% of the sea ice loss (Francis et al. 2005, Deser and Teng 2008, Tseng 2010). Therefore, the role of oceanic forcing in the recent sea ice decline may be significant, especially since ocean heat content has significantly risen globally since 1979 (Intergovernmental Panel on Climate Change (IPCC) 2013).

The upper Arctic Ocean is characterized by strong vertical gradients of temperature and salinity. This leads to highly stratified layers and a complex vertical thermohaline structure. Surface waters in the central Arctic Ocean are quite fresh compared to those at lower latitudes, and their properties undergo strong seasonal

¹Department of Oceanography, Naval Postgraduate School

²Institute of Oceanology, Polish Academy of Sciences, Sopot, Poland

variability under the influence of sea-ice growth and melt, river run-off, solar and longwave radiation (clouds), and seasonally varying atmospheric and oceanic advection (Rudels et al. 1996). At intermediate depth lies the Atlantic Water (AW), which can be found throughout the central Arctic basin with temperatures above 0°C and salinities above 34.5 psu (Steele et al. 1998, Rudels et al. 2004, Rudels 2012). In the Eurasian Basin, the AW is separated from the surface waters by a strong halocline and thermocline. In the central Canada Basin, however, intruding Pacific waters fill the depths between the surface waters and the AW. Figure 3.1 (from Jackson et al. 2010) displays the hydrography of the Canada Basin. There are two major layers of Pacific water in the Canada Basin which Coachman and Barnes (1961) named Pacific summer water (PSW) and Pacific winter water (PWW). PSW is characterized as having a temperature maximum greater than -1.0°C with salinities of 31–33 psu (Shimada et al. 2001, Steele et al. 2004). Timmermans et al. (2014) have shown that the PSW has increased in heat content and freshwater content in recent years, with potential impacts to stratification and vertical heat fluxes. Below PSW is the PWW that is generally found below 150 m and can be identified by a temperature minimum and salinities greater than 33 psu (Coachman and Barnes 1961). PWW is believed to originate from ice formation on the Chukchi Shelf, especially leads and polynyas common in the region during winter months (Pisareva et al. 2015). Although this water mass seems to be fairly consistent in its properties, Steele et al. (1998) found that its lateral extent may be variable in time. The cumulative effect of these layered water masses is a highly stratified upper ocean, with strong density gradients and high Brunt-Väisällä frequencies, especially at the transitions between water masses. Changes in these water masses on time scales from seasonal to multi-decadal period are of fundamental interest to a broad spectrum of arctic and climate scientists.



“Note the depth axis is log scale. In summer, there are up to three temperature maximums (the near-surface temperature maximum (NSTM), Pacific Summer Water (PSW), and Atlantic water), two temperature minimums (the remnant of the previous winter’s surface mixed layer and Pacific Winter Water (PWW)), and three haloclines (the summer halocline, the winter halocline, and the lower halocline). The strongest stratification is associated with the NSTM. Profiles are from a station located at 75°N, 150°W, occupied on 29 August 2006.” (Source: Jackson et al. 2010)

Figure 3.1. Water Mass Structure of the Canada Basin as Characterized by (a) Temperature, (b) Salinity, and (c) Brunt-Väisälä Frequency Profiles. Source: Jackson et al. 2010)

In order to explore the changes in hydrography and the potential role of ocean heat content in the decline of sea ice and to make reasonable projections of future climate states, climate models must adequately represent ocean hydrography. As pointed out by Holloway et al. (2007), there is a deficiency in many Arctic regional models that tend to produce continuously stratified upper layers rather than the more complex hydrography observed. Several advancements have been made in regional modeling since then, including the implementation of subgrid-scale brine rejection parameterization (Nguyen

et al. 2009, Jin et al. 2012), improved representation of sea-ice physics (Roberts et al. 2016), and increased horizontal resolution (Maslowski et al. 2012). The goal of this study is to objectively compare the skill of both global and regional climate models and to identify the model developments that lead to improved representation of upper ocean thermohaline structure in the central Canada Basin.

B. MODEL DESCRIPTIONS

1. Climate Models

Four Earth-system and global climate models (ESMs and GCMs, hereafter simply CMs), and one regional climate model, the Regional Arctic System Model (RASM), have been selected for inter-comparison and evaluation with observations. These models are the NCAR Community Earth System Model – Large Ensemble² (CESM-LE; Kay et al. 2015), the NOAA Geophysical Fluid Dynamics Laboratory Climate Model version 3 (GFDL-CM3; Griffies et al. 2011), the Met Office Hadley Centre Global Environmental Model version 2 – Carbon Cycle (HadGEM2-CC; Bellouin et al. 2011), and the Max Plank Institute for Meteorology Earth System Model – medium resolution (MPI-ESM-MR; Jungclaus et al. 2006). GFDL-CM3, HadGEM2-CC, and MPI-CC were chosen because they were included as part of the Coupled Model Intercomparison Project Phase 5 (CMIP5; Taylor et al. 2012) and were identified by Massonnet et al. (2012) as the CMIP5 models with the most reasonable sea ice extent. Although CESM-LE was not included in CMIP5 or the Massonnet et al. (2012) analysis, a previous version, CESM version 1, was. There are no significant differences in the ocean and sea ice components of CESM version 1 and CESM-LE. A brief summary of the four climate models used in this paper is included in Table 3.1. Only results from the historical experiments are used in this analysis for the purpose of model evaluation. No output from those models beyond 2005 (i.e., the end of historical simulations) are considered.

² Ensemble member number one is used in this comparison. A single ensemble member is preferred over the ensemble mean, as the mean would smooth out variability and structure.

Table 3.1. Earth System and Global Climate Models Compared in this Study.

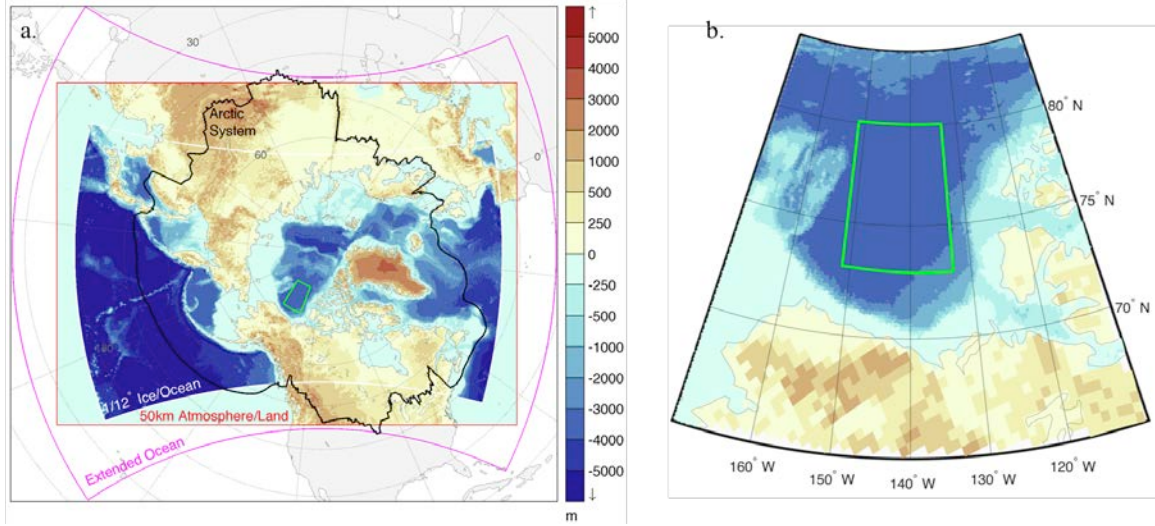
| Model Name | Institution | Main reference | Atmosphere component name and resolution | Ocean component name and resolution | Sea Ice component name |
|------------|--|-----------------------|--|--|------------------------|
| CESM-LE | National Center for Atmospheric Research | Kay et al. 2015 | CAM5 30 levels at $\sim 1^\circ$ | POP2 60 levels at $\sim 1^\circ$ | CICE4 |
| GFDL-CM3 | NOAA Geophysical Fluid Dynamics Laboratory | Griffies et al. 2011 | Included 48 levels at 200 km | MOM4.1 50 levels at 1° | SIS |
| HadGEM2-CC | Met Office Hadley Center | Martin et al. 2011 | HadGAM2 60 levels at $\sim 1.6^\circ$ | Included 40 levels at 1.875° | Included |
| MPI-ESM-MR | Max Plank Institute for Meteorology | Jungclaus et al. 2006 | ECHAM6 95 levels at 1.8° | MPIOM 40 levels at 1.5° | Included |

2. Regional Arctic System Model Experiments

The model experiments conducted with the Regional Arctic System Model (RASM) for this dissertation are similar to those conducted for my M.S. thesis in 2014. The following description of RASM is still valid to this dissertation:

RASM is a limited-domain, fully coupled, high-resolution atmosphere, ocean, sea ice, and land model. The primary components are the Weather Research and Forecasting (WRF) model, Los Alamos National Laboratory (LANL) Parallel Ocean Program (POP) and Sea Ice Model (CICE), and the Variable Infiltration Capacity (VIC) land hydrography model. These four components are coupled using the Community Earth System Model (CESM [1.2]) coupler, CPL7. The domain of RASM includes the Arctic Ocean and surrounding marginal seas as well as the sub-Arctic North Pacific and North Atlantic. (DiMaggio 2014)

Figure 3.2, panel a, illustrates the domain of RASM.



(a) The $1/12^\circ$ coupled ice-ocean component is shaded by bathymetry, 50 km atmosphere and land components are outlined in red, and the extended ocean domain is outlined in magenta. The black line outlines the Arctic System defined as the area “north of the boreal mean decadal 10°C sea surface isotherm, the surface air 0°C contour that encircles the North Pole, and the southern limit of terrain that drains into the High Arctic” (Roberts et al. 2010). (b) The area in which model and observational data are analyzed is outlined in green.

Figure 3.2. RASM Domain (a) and Region of Study (b).

For this study, several additional experiments were conducted using the RASM framework. A summary of these configurations is listed in Table 3.2. Again, the description of RASM components from my 2012 thesis are still valid. “[In most configurations,] POP is configured on a rotated spherical coordinate grid with horizontal resolution of $1/12^\circ$ (~ 9 km), has 45 fixed-depth vertical layers, with 8 layers in the upper 50 m, and it is fully coupled with CICE” (DiMaggio 2014). Two exceptions to this are GV-SB and GH-S. In case GV-SB, POP is configured with 60 vertical levels with 10 levels in the upper 50 m and 20 levels in the upper 100 m; in GH-S case, POP is configured with a horizontal resolution of $1/48^\circ$ (~ 2.4 km), still with 45 vertical layers. Case R uses the fully-coupled configuration as previously described; in all other cases the atmospheric and land hydrology components have been replaced by a data model that uses “realistic forcing from the Common Ocean Reference Experiment version two (CORE2) reanalysis from the National Center for Atmospheric Research (NCAR)” (DiMaggio 2014). This reduces computation time and allows for many more experiments

to be run. Each experiment differs only slightly from another, in order to isolate the effects of each change. The model configurations that are being experimented with are: sea-ice physics, vertical mixing, brine parameterization, numerical restoring to climatological temperature and salinity, and horizontal and vertical resolution. The reader is directed to Table 3.2 for a summary of each experiment configuration. For a more detailed discussion on RASM configurations, see Maslowski et al. (2012) and Roberts et al. (2016).

Table 3.2. RASM Experiments Compared in This Study.

| Name | Description | Resolution | Coupling | Spin up | Sea ice treatment | Brine treatment |
|-------|--|---------------------------|---|--|-------------------|-------------------|
| R | Fully-coupled baseline | 45 levels at $1/12^\circ$ | fully coupled | T & S = PHC u & v = 0 62 yr spin-up t_0 = Jan 1948 | EAP, Cf=21.3 | none |
| G | Atmospheric forcing from CORE2 | " | ice-ocn forced with CORE2 | " | " | none |
| G-V | EVP instead of EAP | " | " | " | EVP, Cf=21.3 | none |
| G-S | Ocean restoring during spin-up | " | " | same but with ocean 3-D restoring of T & S to PHC during spin-up | EAP, Cf=21.3 | none |
| G-SB | Brines after Jin et al. 2012 | " | " | " | " | Jin et al. (2012) |
| G-SB1 | Increased ice strength (Cf) | " | " | " | EAP, Cf=34 | Jin et al. (2012) |
| G-SB2 | Lower convective diffusivity and viscosity | " | " | " | " | Jin et al. (2012) |
| G-SBM | Adjusted surface momentum fluxes | " | 0.5*ice-ocn stress 0.75*atm-ice stress 1.5*atm-ocn stress | " | " | Jin et al. (2012) |
| GV-SB | Similar to G-SB with higher vertical resolution | 60 levels at $1/12^\circ$ | same as G-SB | " | EAP, Cf=22 | Jin et al. (2012) |
| GH-S | Similar to G-S with higher horizontal resolution | 45 levels at $1/48^\circ$ | same as G-S | " | EAP, Cf=22 | none |

3. Observational Data for Comparison: PHC and ITP

To evaluate model performance, two observational data sets are used. The Polar Science Center Hydrographic Climatology (PHC) is an oceanographic climatological data set that combines data from the World Ocean Atlas and the Arctic Ocean Atlas

(Steele et al. 2001). This data set includes monthly mean fields of temperature and salinity at 33 vertical levels, on a $1^{\circ} \times 1^{\circ}$ lat/long grid. The PHC data were interpolated onto the RASM grid for the comparisons presented in this paper. Ice-tethered profilers (ITPs) have been collecting hydrological data in the Arctic since 2005 (Krishfield et al. 2008) and provide a time-varying data set to which RASM hind-casts can be compared.

4. Region of Study

This study will focus on the central Canada Basin (CCB) in the western Arctic Ocean as highlighted in Figure 3.2b. This region contains the layered water masses that have undergone recent changes as described in Section A of this chapter, and has been frequently sampled by the ITP program. The ocean bottom is approximately 3500 meters in depth and is relatively flat. The ice pack in this region has experienced dramatic changes in recent years; summertime ice extent has dramatically decreased, and wintertime multi-year ice has been replaced by first-year ice (Galley et al. 2016).

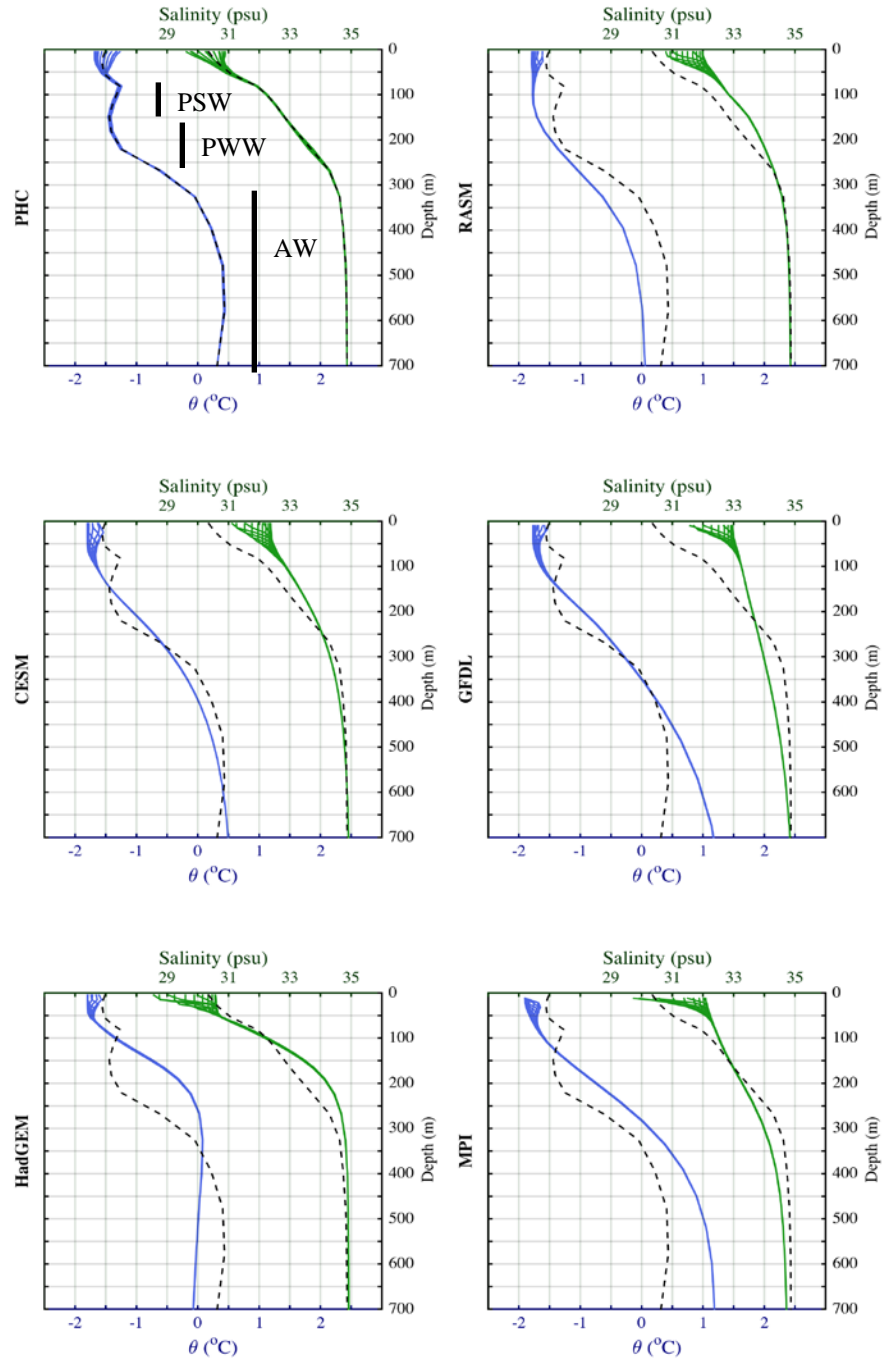
C. CLIMATE MODEL SKILL

Under the framework of CMIP5, the historical experiments contain results up to the year 2005. Therefore, the time frame for comparing CMs to PHC is restricted to the years from 1980 (after the initiation of satellite observations of the Arctic) to 2005. Profiles of ocean temperature, salinity, density, and sound speed of the upper 700 m are compared. This depth range was chosen because it includes all of the waters of Pacific origin, the main thermocline and halocline between the PWW and AW, as well as most of the AW. This depth range also spans the operating depths of ice-tethered profiles, enabling their use in evaluating RASM (Section D). Selected bulk properties such as mixed layer depth, ocean heat content, and freshwater content are also compared later in this section.

1. Profiles

The twenty-six years of monthly-mean model outputs in this analysis are binned by month and area and averaged to create a mean annual cycle for the CCB region. The resulting profiles of potential temperature and salinity are plotted in Figure 3.3. In the

top-left panel, the 12 months of PHC potential temperature and salinity are plotted as a function of depth. There is some seasonal variability near the surface associated with the seasonal mixed layer, but the hydrography of PSW, PWW, and AW is constant. The RASM experiment shown in the second panel is the fully-coupled, $1/12^{\circ}$ horizontal resolution “baseline” configuration R (Table 3.2). Throughout the water column, RASM has a cold bias in potential temperature as compared to PHC (dashed lines). The PSW temperature maximum shown in PHC is missing in RASM, though temperatures remain low down to 150 m. The thermocline above the AW is weaker than in PHC and begins at around 150 m, which is 75 m too shallow. The peak AW temperature in PHC is about 0.5 $^{\circ}\text{C}$ at 550 m, while RASM’s AW temperature only reaches 0.1 $^{\circ}\text{C}$ by 700 m, and appears to have not reached a maximum. There is a high salinity bias in the upper 250 m in RASM. Surface salinities are roughly 1 psu higher than PHC, though the seasonal range of variations are similar. The winter halocline is located near the appropriate depth of around 75 m, but is weaker than PHC climatology. PWW salinity is 0.75 psu higher than climatology, and the lower halocline is also weaker. AW salinities are represented well. There are many potential causes of these discrepancies, and several will be discussed in Section D of this chapter. Overall, however, the baseline RASM configuration is not capturing the strong temperature and salinity gradients in the upper 300 m, and has a cold bias compared to PHC. It is worth to note here, that due to challenges in sampling the Arctic Ocean during the winter, PHC contains a higher proportion of summertime samples and therefore possibly possesses a warm and fresh bias in the upper ocean (Steele et al. 2001).



Each profile represents a single month from the mean annual cycle. The dashed black line is the total mean of all months from PHC, overlaid on each panel for comparison. Climatological depth ranges of PSW, PWW, and AW are indicated with vertical black bars. The shallowest depth represented in MPI is 12 m, and the shallowest depth in GFDL is 10 m. All other models have data starting at 5 m depth.

Figure 3.3. Potential Temperature (Blue) and Salinity (Green) of the Upper 700 m from PHC and Modeled by RASM, CESM, GFDL, HadGEM, and MPI.

The first ensemble member of the CESM-Large Ensemble is shown in the third panel, labeled CESM. The surface temperature, like in RASM, is slightly lower than in PHC, and the PSW temperature maximum is similarly missing. Below the mixed layer, temperatures immediately begin increasing continuously to a depth of 700 m, where the maximum temperature reaches approximately 0.5 °C. Although this maximum temperature value is similar to that of PHC, it is about 200 m too deep. CESM salinities are similar to those of RASM; they are too high from the surface to 300 m.

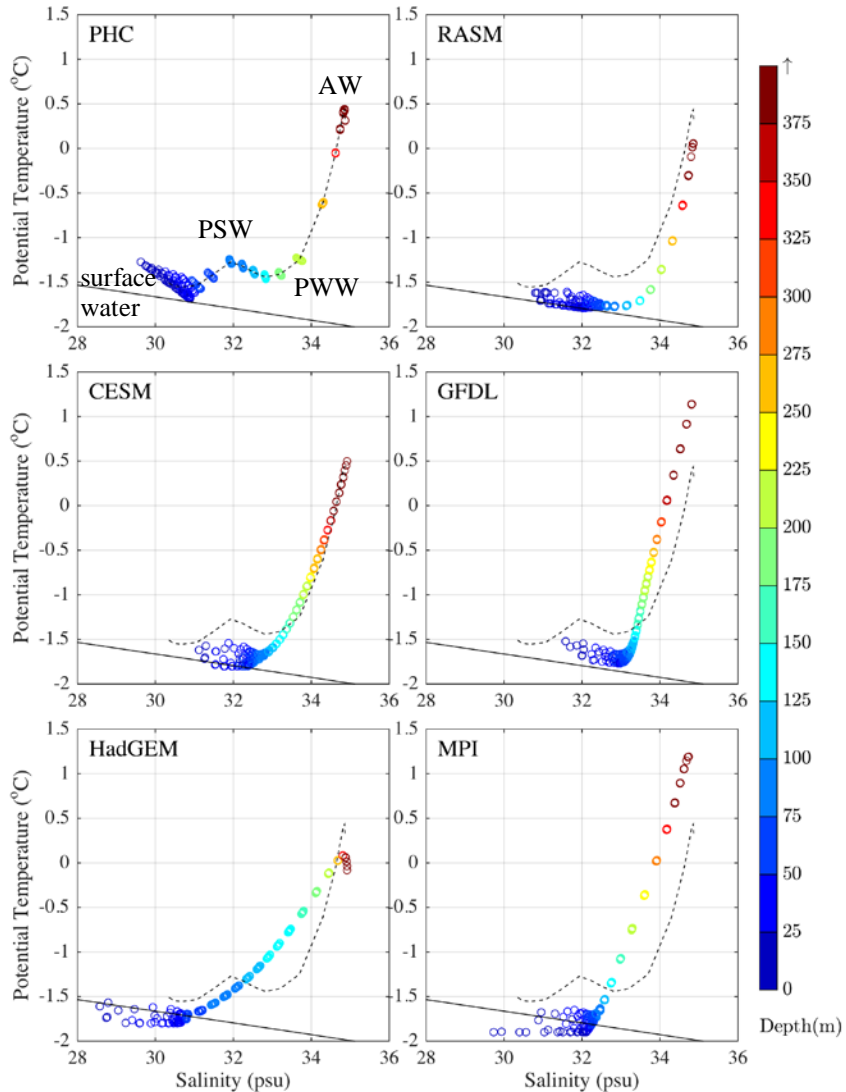
Results from GFDL-CM3 are shown in the fourth panel of Figure 3.3 and are labeled GFDL. As with CESM, temperatures begin rising immediately below the mixed layer and rise continuously to 700 m. The temperature gradient throughout the column remains high all the way past 500 m. Although the GFDL temperatures are similar to PHC in the 250 to 450 m range, GFDL temperature has overshot PHC by almost a full degree in the AW. As with both of the previous models, the salinity of GFDL is too high near the surface. However, the vertical salinity gradient is constant below the mixed layer, resulting in a gradient that is too weak in above the AW and too large in the AW.

The HadGEM2-CC model (fifth panel, Figure 3.3, labeled as HadGEM) has relatively better representation of temperatures and salinities at depth between 50 and 100m. However, it, too, is missing PSW and PWW temperature maxima and minima below the mixed layer, but it does recreate a strong vertical temperature gradient above the AW. Unfortunately, this thermocline is about 100 m too shallow, and the peak temperature is about 0.4 °C too cold and 225 m too shallow. A strong single salinity gradient exists, rather than the two distinct upper and lower haloclines associated with the top of the PSW and top of AW. AW salinities are similar to PHC below 400 m.

The final climate model discussed here is the MPI-ESM-MR, labeled in Figure 3.3 as MPI. As with all other models shown here, the temperature profile is missing the structure associated with the Pacific waters. The AW temperature, however, is much higher than PHC or any other model. Surface salinities are also too high in MPI, and the halocline is too weak. AW salinities are too low, but gradually reach those of PHC by 700 m.

2. T-S Diagrams

Plotting data as temperature-salinity (T-S) diagrams (Figure 3.4), offers another perspective in comparing models' representation of water mass properties. In T-S space, it is easy to identify the major water masses on the panel labeled PHC: AW has high temperature and salinity, PWW has moderate salinity (~33 psu) and low temperature, PSW is slightly warmer than PWW and has a salinity around 32 psu, and the surface mixed layer properties vary seasonally near the freezing line and slightly warmer. RASM generally parallels PHC, but at cooler temperatures. The PSW peak is too small, and temperatures are near freezing above 125 m. CESM possesses a cold bias above 150 m and below freezing surface temperatures, but otherwise matches the shape of PHC. GFDL's AW is too warm, and waters above 125 m are too cold and too salty. In HadGEM, both the AW and surface waters are slightly too cool, but the weak gradients of temperature and salinity result in a too-warm PWW. Additionally, the surface water temperatures drop below the freezing line, indicating unrealistic super-cooled surface waters. MPI, like GFDL, has a too-warm AW and too-cool surface waters, which are also sub-freezing. Sub-freezing temperatures may be produced as a consequence of their coupling to the sea ice component. For example, in some versions of CICE, melting ice adds water to the surface of the ocean at a fixed temperature of -1.8°C . This temperature corresponds to the freezing temperature of sea water at a salinity of 33 psu. For surface waters that are fresher than 33 psu, this parameterization of melt water injection can lead to super-cooled temperatures. RASM does not produce sub-freezing temperatures since it uses CICE5, which allows for melt water to be added to the ocean at a salinity-dependent freezing temperature.



Each colored circle represents a different model-level value and is colored according to depth. The mean PHC T-S curve is plotted as a dashed line, and the freezing temperature is plotted as a solid line on all panels for reference.

Figure 3.4. Potential Temperature as a Function of Salinity of Water Mass Properties from PHC, RASM, and CMs.

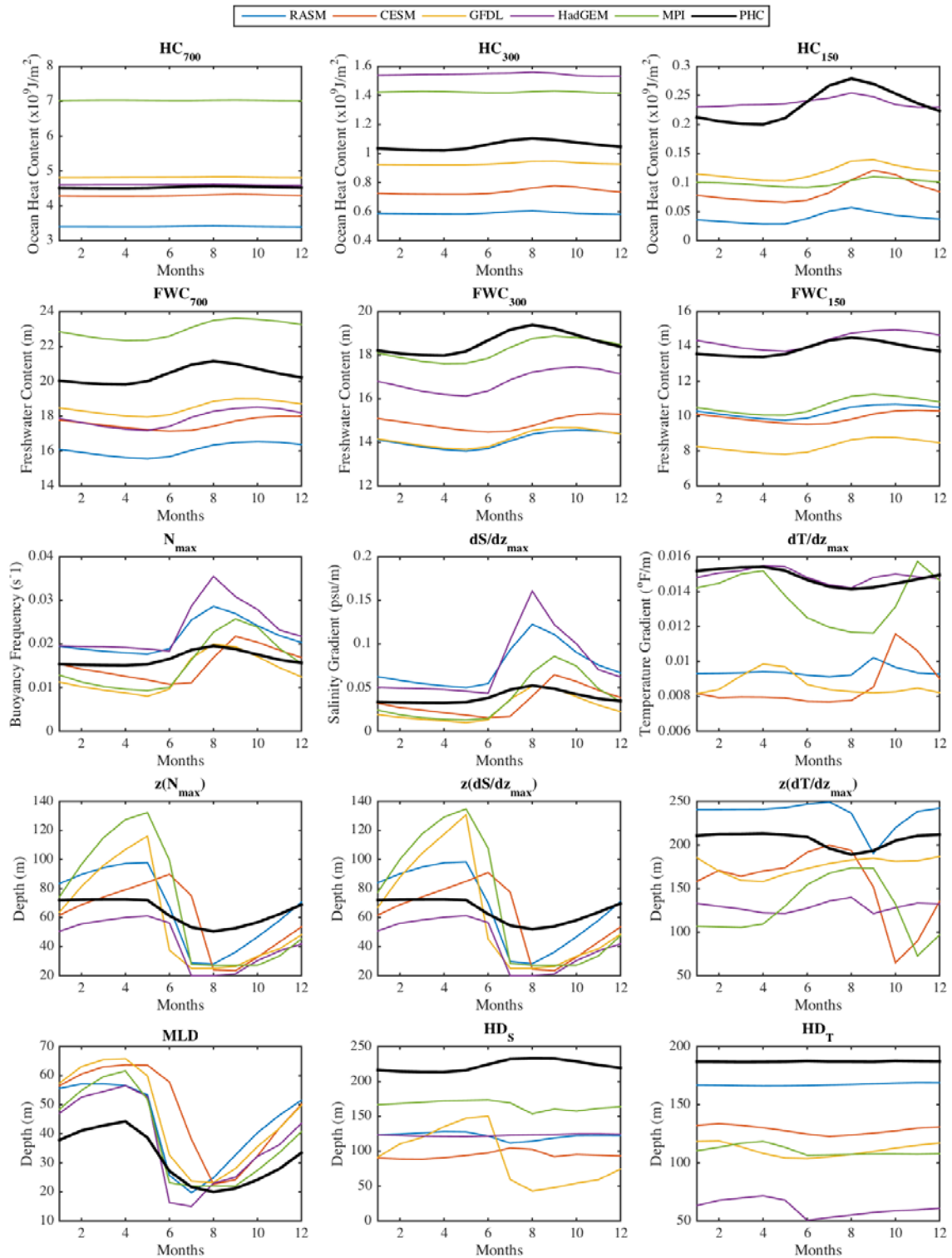
3. Bulk Property Time Series

Errors in ocean temperature and salinity will have an effect on coupled processes like heat and momentum exchange between the atmosphere and ocean. To illustrate and quantify these effects, several bulk properties are derived from the profiles of temperature

and salinity and plotted in Figure 3.5. The properties compared in this section are ocean heat content, freshwater content, maximum Brunt-Väisällä frequency (magnitude and depth), maximum temperature gradient (magnitude and depth), maximum salinity gradient (magnitude and depth), mixed layer depth, and halocline depth. Ocean heat content per area (HC) is computed as follows:

$$HC_D = C \sum_{k=1}^{k=D} \rho_k (T_k - T_{ref}) dz_k \quad (3.1)$$

where C is the heat capacity of water ($4186 \text{ J/kg}\cdot\text{K}$), ρ_k is the density of the k^{th} level of the model's vertical grid, T_k is the temperature of that level, T_{ref} is the reference temperature (chosen as the freezing temperature), dz_k is the thickness of the model level k , and D is the deepest depth included in the sum. Plotted in the top row of Figure 3.5 are the mean annual cycles of HC integrated from the surface to three different depths. HC_{700} includes heat from the surface to 700 m; this range includes surface waters, Pacific waters, the lower halocline, and the core of the AW. The mean annual cycle of HC_{700} in PHC is relatively constant at $4.5 \times 10^9 \text{ J/m}^2$. The CESM, HadGEM, and GFDL models are all within $0.3 \times 10^9 \text{ J/m}^2$ of PHC; RASM's HC_{700} is $1.1 \times 10^9 \text{ J/m}^2$ lower than PHC and MPI's is $2.5 \times 10^9 \text{ J/m}^2$ higher. Because the AW temperatures are so much higher than the other waters, the AW heat content dominates this calculation. Raising the lower depth limit to 300 m excludes the core AW, but retains the lower thermocline. HC_{300} in PHC ranges from $1.02 \times 10^9 \text{ J/m}^2$ in late winter to $1.10 \times 10^9 \text{ J/m}^2$ in late summer. GFDL recreates the closest HC_{300} to PHC at approximately $0.93 \times 10^9 \text{ J/m}^2$. CESM and RASM both have too little heat content in this depth range and HadGEM and MPI have too much. We go even further and eliminate the thermocline by limiting the lower depth to 150 m. The heat in this depth range includes surface mixed layer heat, the near-surface temperature maximum, and PSW. In PHC, HC_{150} ranges from 0.20 to $0.28 \times 10^9 \text{ J/m}^2$ seasonally, and all models, except for HadGEM, under represent this heat. This result is expected, considering none of the models adequately represented the PSW temperature maximum (Figure 3.3). The heat content in the upper 150 m of HadGEM is similar to that of PHC, but it can clearly be seen in Figure 3.3 that this result is a consequence of the much too shallow AW thermocline.



See text for descriptions of each panel

Figure 3.5. Mean Annual Cycles of Fifteen Bulk Water Mass Properties from PHC and Modeled by RASM, and CMs.

Ocean freshwater content per area (FWC), measured as equivalent thickness of fresh water referenced to a chosen salinity, is computed as follows:

$$\text{FWC}_D = \sum_{k=1}^{k=D} (S_{\text{ref}} - S_k) dz_k \quad (3.2)$$

where S_k is the salinity of the model level, and S_{ref} is a reference salinity of 35 psu. The panels of the second row of Figure 3.3 show the mean annual cycles of FWC. The FWC_{700} of PHC shows a seasonal cycle of 19.8 to 21.2 m of FWC_{700} , with more fresh water in the summer. All models except MPI have 2–4 m less FWC_{700} than PHC; MPI's FWC_{700} is 3 m greater. Eliminating the core AW, MPI's FWC_{300} is very close to that of PHC at 18 to 19.5 m. All other models have 1.5 to 4 m lower FWC_{300} . When restricting the FWC calculation to just the upper 150 m, only HadGEM reproduces a similar result to PHC, all others have too little freshwater.

The upper Arctic Ocean exhibits strong stratification. One way to quantify this stratification is by computing the Brunt-Väisällä frequency:

$$N = \frac{-g}{\rho} \frac{d\rho}{dz} \quad (3.3)$$

By computing the maximum Brunt-Väisällä frequency (N_{max}), the strength of stratification can be compared across models. The panel labeled N_{max} in Figure 3.5 shows the mean annual cycles of N_{max} . A weak seasonal cycle exists in the N_{max} of PHC; all models show a similar seasonal cycle, though models show a greater variance. Similarly, the depth of the maximum stratification (Figure 3.5, panel labeled $z(N_{\text{max}})$) varies only between 50 m and 72.6 m in PHC, but the seasonal variations are much stronger in all models. The seasonal cycle of the maximum salinity gradient (dS/dz_{max}) is well correlated with N_{max} , an expected result since density (and therefore density gradient) is strongly dependent on salinity in the Arctic. The depth of the maximum salinity gradient ($z(dS/dz)_{\text{max}}$) is similar to $z(N_{\text{max}})$ in all models; the maximum salinity and density gradients are shallow in the summer and deeper in winter.

The models have a wider spread in representing the temperature gradient. The maximum temperature gradient (dT/dz_{max}) in PHC varies seasonally from 0.017 °C/m in winter to 0.015 °C/m in summer, and the depth of the maximum temperature gradient

$(z(dT/dz)_{\max})$ varies slightly around 206 m, which represents the depth of the AW thermocline. Only HadGEM and MPI reproduce a similar dT/dz_{\max} , although the thermocline depths in those models are on average 77 m shallower. RASM places $z(dT/dz)_{\max}$ slightly deeper than PHC, while other models place it too shallow. In all of the analyzed data sets, there is a second slightly weaker peak in temperature gradient associated with the bottom of the winter mixed layer (not shown) that varies in depth and strength seasonally. In two of the models, MPI and CESM, the mixed layer thermocline becomes stronger than the AW thermocline in October and November, causing $z(dT/dz)_{\max}$ to decrease dramatically.

The MLD is an important diagnostic for evaluating a coupled model. Here, the MLD is defined as the depth at which ρ is at least 0.25 kg/m^3 greater than that of the shallowest level. This density change threshold method is similar to that used by Timmermans et al. (2012). Plotted in the first panel of the bottom row of Figure 3.5 is the mean annual cycle of the MLD. All models produce an MLD seasonal cycle that is well correlated with that found in PHC, but winter MLD's are overestimated in all models by 10 to 25 m. During summer months, most models produce an MLD closer to that of PHC. Because PHC contains a higher proportion of summertime samples, it is reasonable to expect that the wintertime MLD's in PHC are underrepresented (Steele et al. 2001). The MLD depths are well correlated with the depths of maximum salinity and density gradients, $z(dS/dz)_{\max}$, and $z(N_{\max})$, suggesting that they are all tracking the same feature. However, the MLD remains shallower than 70 m in all models, while the $z(dS/dz)_{\max}$ and $z(N_{\max})$ both deepen to over 100 m in some models. In PHC, the $z(dS/dz)_{\max}$ and $z(N_{\max})$ are correlated to the MLD, but are both deeper than the MLD.

The lower halocline, sometimes referred to as the cold halocline, is the strong salinity and temperature gradients that separate the warm and salty AW from the colder and fresher PWW. There have been few methods proposed for quantifying the halocline depth (Bourgain and Gascard 2011; DiMaggio 2014), and any definition would depend on what phenomenon or quantity was being studied. Here we define the halocline depth (HD) in two ways. The first, HD_S , is the depth of the maximum salinity gradient below the MLD. In PHC, the HD_S remains between 213 and 222 m throughout the year (Figure

3.5, panel labeled HD_S). The HD_S produced in all models is shallower than that in PHC. The halocline depths that result from this definition are generally around the same depths as the strong thermocline above the AW. If one were to compute ocean heat content above this depth, the thermocline would contribute a significant amount of heat. Therefore, a second way to define the halocline depth (HD_T) is proposed as the depth of the minimum temperature gradient above the AW, which should correspond to the depth of the PWW temperature minimum. Below the HD_T , temperature increases towards the AW temperature maximum. Ocean heat content above the HD_T consists of heat content of only Pacific and surface waters, which have the greatest potential of affecting sea ice and the surface heat budget. All of the models analyzed have a HD_T that is shallower than that of PHC, though the HD_T in RASM is closest to that in PHC.

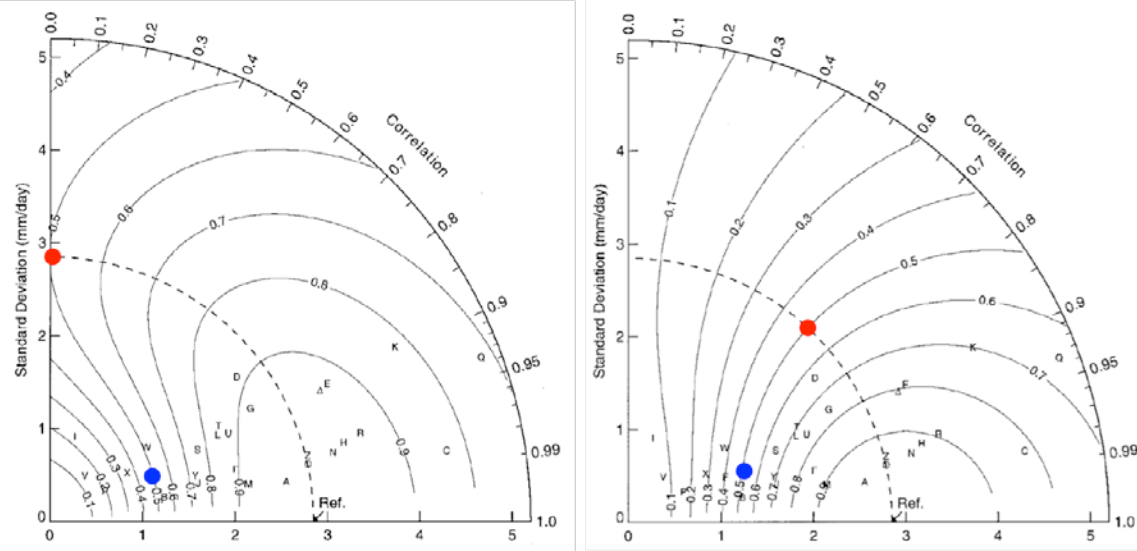
4. Taylor Diagrams and Skill Scores

As a way to compare model performance, Taylor Diagrams (Taylor 2001) are a useful tool, which display multiple sets of statistics on a single plot. The statistics computed are the standard deviation of a set of model results and the correlation between the model results and reference data, often an observational data set. The Taylor Diagram plots a model's standard deviation along the radius and the correlation coefficient as an angle on a polar plot. As a consequence of their geometric relationships, the centered root mean square (RMS) deviations increase with distance from the reference value. Additionally, Taylor (2001) proposed an objective method for comparing model performance with a skill score. The Taylor Skill Score considers a model's ability to reproduce the variance of an observable quantity as well as the correlation between the modeled and a reference data set. That reference data set could be derived from observations or another model. For a given quantity, the skill can be determined by

$$S = \frac{4(1+R)^n}{(\hat{\sigma}_m + 1/\hat{\sigma}_m)^n (1+R_o)^n} \quad (3.4)$$

where $\hat{\sigma}_m$ is the ratio of the standard deviation of model results to the standard deviation of the reference data (i.e. $\hat{\sigma}_m = \sigma_m / \sigma_o$ where m and o subscripts refer to the model and observational data, respectively.) R is the correlation between the model results and the

reference data, R_0 is the maximum correlation attainable (e.g., due to observational uncertainty), and n is a weighting factor. As modeled variance approaches observed variance, and as R approaches R_0 , skill approaches 1. Skill decreases to zero as correlation becomes more negative or as variance decreases to zero or increases to infinity. Because this score accounts for both variance and correlation, models are penalized for too strong or too weak values and if the local maxima are at the wrong time or location. The choice of n may strongly affect the skill score. Taylor (2001) showed that setting $n = 1$ results in a score that allows for very low correlations without strong skill score penalties. Taylor (2001) also considers setting $n = 4$, which increases the penalties for low correlation, but perhaps by too much. Examples of Taylor Diagrams with overlaid contours of Taylor Skill Scores are reproduced from Taylor (2001) in Figure 3.6.



Left panel: Overlaid skill scores use the weighting factor $n = 1$. A hypothetical model (indicated with a red dot) with the same standard deviation as observations could still have a skill score of 0.5 despite having zero correlation. Conversely, a different model (indicated with a blue dot) could have the same skill score despite having a correlation greater than 0.95.

Right panel: Overlaid skill scores use the weighting factor $n = 4$. A hypothetical model (indicated with a red dot) with relatively high correlation of 0.7 and the same standard deviation as observations would only have a skill score of 0.5. Meanwhile, a model with a significantly lower standard deviation earns the same skill because of its high correlation.

Figure 3.6 Example Taylor Diagrams with Overlaid Contours of Taylor Skill Score. Adapted from Taylor 2001.

For the analysis of the CMIP climate models, we use PHC climatology as our reference data set. Because all models are being compared to the same data set, the choice of R_o may be chosen arbitrarily to 1 without qualitatively changing the results. We chose the skill weighting factor $n = 2$, which balances the contributions of error produced by poor variance and correlation; i.e.

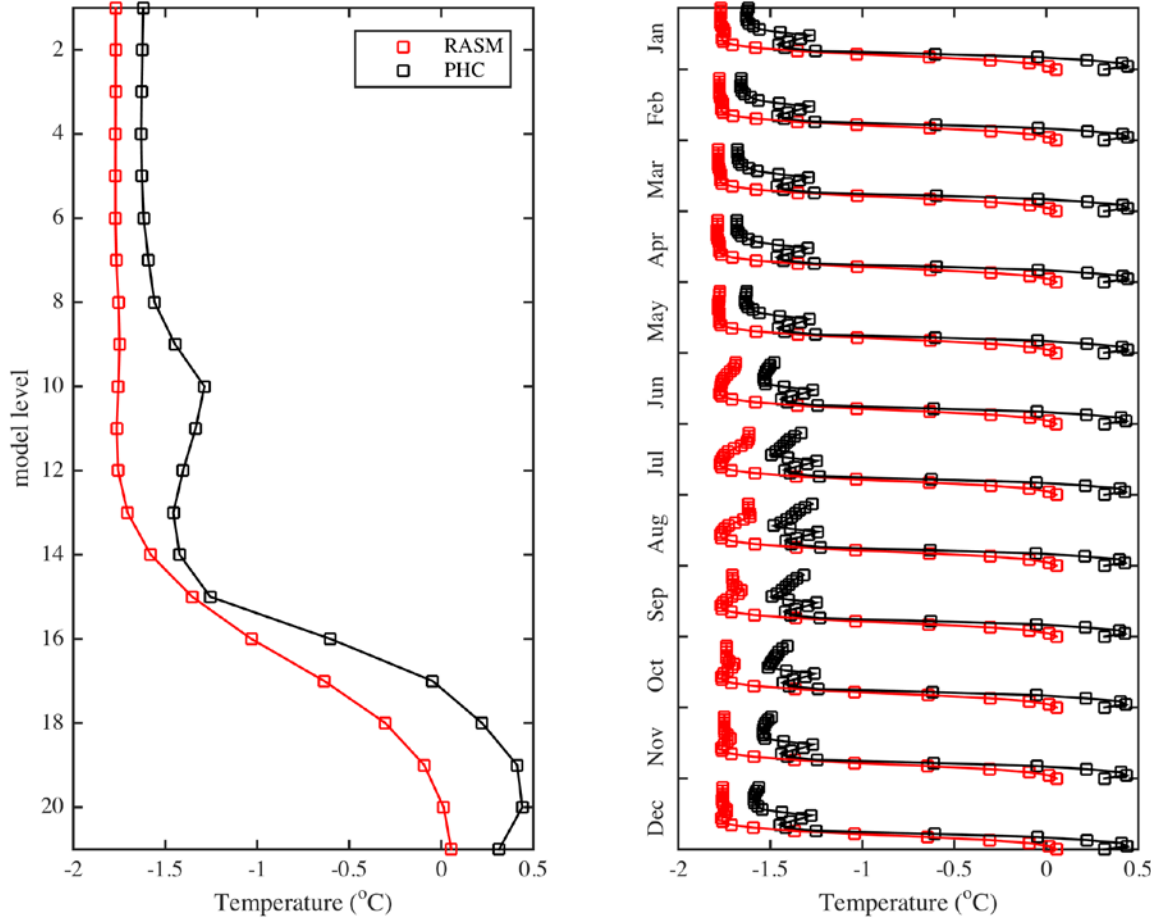
$$S = \frac{4(1+R)^2}{(\hat{\sigma}_f + 1/\hat{\sigma}_f)^2 (1+R_o)^2} \quad (3.5)$$

The computation of the standard deviations and correlations are done using the common methods:

$$\sigma = \sqrt{\frac{1}{N} \sum_{i=1}^N (x_i - \bar{x})^2} \quad (3.6)$$

$$R = \frac{\sum_{i=1}^N (x_i - \bar{x})(y_i - \bar{y})}{\sqrt{\sum_{i=1}^N (x_i - \bar{x})^2 \sum_{i=1}^N (y_i - \bar{y})^2}} \quad (3.7)$$

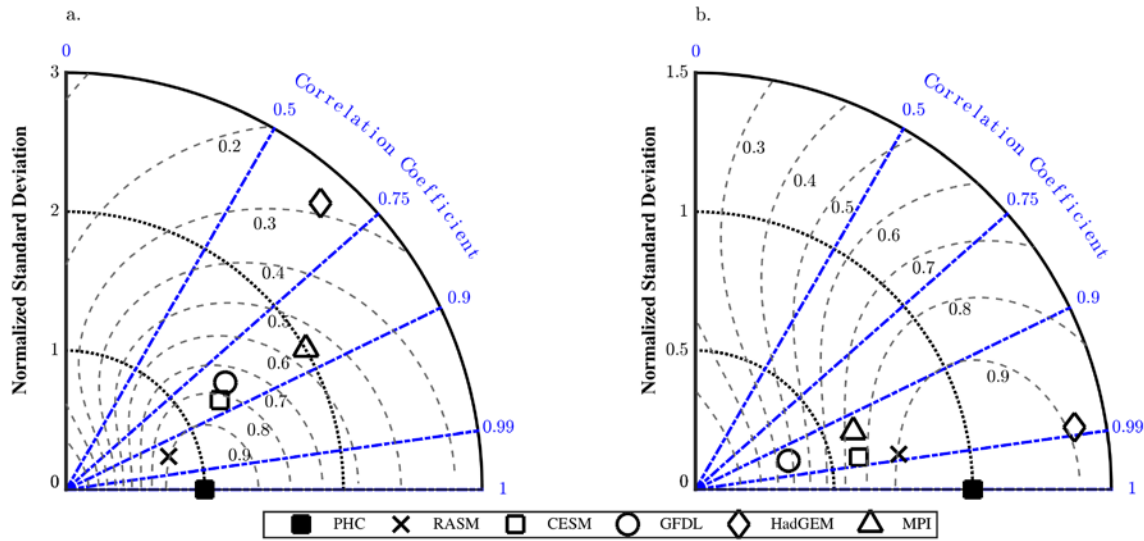
where x_i and y_i represent members of a data set that varies in time only (i.e., $x_i(t)$), or both depth and time (i.e., $x_i(z, t)$); \bar{x} and \bar{y} represent the means of those data sets, and N is the size of that data set. In this way, we are computing spatio-temporal pattern statistics and skill scores. We may evaluate model performance across any interval of z or t ; in the case of climate models, we are comparing seasonal variability against the twelve-month climatology and are choosing three depth intervals: $0 \leq z \leq 700\text{m}$, $0 \leq z \leq 300\text{m}$, $0 \leq z \leq 150\text{m}$ for the depth-varying data sets. For example, Figure 3.7 shows the mean January temperature profile from RASM and PHC as a function of model level in the left panel, and the twelve-month seasonal cycle in the right panel.



The left panel shows data from January; the right panel shows data from all months. The lower depth of RASM model level 21 is 700 m.

Figure 3.7. RASM and PHC Temperature as a Function of Model Level.

Figure 3.8 shows a pair of Taylor Diagrams (Taylor 2001) comparing upper 300 m potential temperature and salinity from the models to PHC. In both temperature and salinity, RASM's statistics are the closest to those of PHC. For temperature, HadGEM has the lowest correlation, and the highest standard deviation of 2.76 times that of PHC. All models have high correlation in salinity. HadGEM has a higher standard deviation than PHC, and all other models have a lower standard deviation. RASM and HadGEM both score near 0.9 in upper 300 m salinity; only RASM scores near 0.9 in upper 300 m temperature.

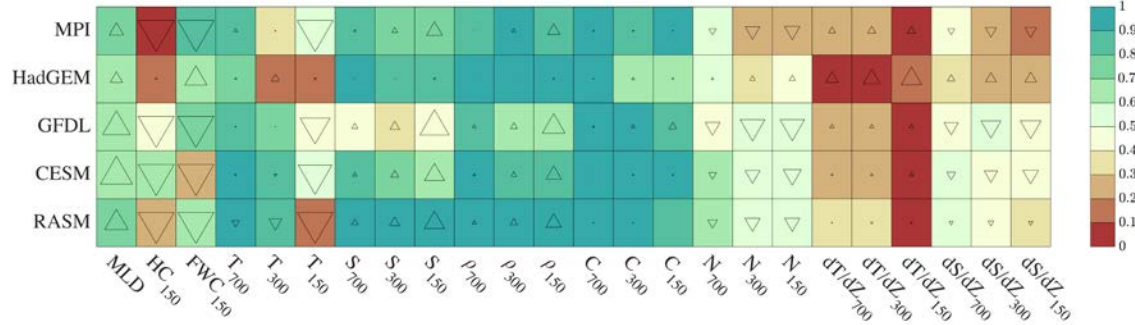


Normalized standard deviation is plotted as a function of correlation coefficient on a polar plot. Skill scores are contoured as grey dashed lines.

Figure 3.8 Taylor Diagrams of Upper 300 m Ocean Potential Temperature (a.) and Salinity (b.) from RASM and Four Climate Models.

Taylor Diagrams could be produced for any number of observables, but a more efficient way of comparing model skill is to simply compute Taylor skill scores (using Equation 3.5) for the chosen observables and display them along with their relative biases in Figure 3.9. Biases are computed as the difference between the means of the model and PHC. Similar information can be obtained by analyzing the time series of Figure 3.5 and profiles of Figure 3.3, but this method allows for a much simpler, quantitative and objective comparison. Each row of Figure 3.9 displays the skills scores for an individual model; each column represents a different observable. The first columns rows show skills for the important near-surface bulk parameters of MLD, HC, and FWC. All models score well at representing the mean annual cycle of MLD, although they all overestimate its depth and have a positive bias. MPI and RASM have the highest skills with relatively low biases. Large negative biases (greater than twice the standard deviation) exist in all models except for HadGEM at representing both upper 150 m heat content (HC_{150}) and fresh water content (FWC_{150}). HadGEM reproduces HC_{150} and FWC_{150} with smaller positive biases but its score for HC_{150} second lowest after MPI. CESM scores the highest

for HC_{150} , but the lowest for FWC_{150} . MPI scores the highest for FWC_{150} , but the lowest for HC_{150} .



Each column is a different observable (see text for descriptions). Scores are displayed in rows of models and columns of observables. The color of each block represents the skill score where 1 is best skill and 0 is worst. The size of the triangle indicates the bias of the model; smaller triangles represent smaller biases, and a triangle that fills its box represents a bias that is more than two standard deviations away from the mean of the observed quantity. An upward (downward) pointing triangle indicates a positive (negative) bias.

Figure 3.9 Taylor Skill Scores for RASM and CMs Evaluated Against PHC.

These first three sets of scores evaluate a model's ability to reproduce a one-dimensional mean annual cycle of a bulk value. The remaining scores evaluate profiles varying in time, and are computed using the pattern skill described above. To score well, a model must reproduce the shape of the profile and its temporal variance. The first three sets of profiles compared are potential temperature from the surface to 700 m (T_{700}), surface to 300 m (T_{300}), and surface to 150 m (T_{150}). All models score well for T_{700} and have small biases. As discussed above, the AW properties dominate this depth range, so one can infer that models perform well at representing the AW. Model performance for T_{300} , which excludes the core AW, is reduced in all models, although HadGEM and MPI have the largest decreases in skill. All models score poorly at representing T_{150} , and all models except for HadGEM have a very large temperature bias. All models score fairly well at representing all three depth-ranges of salinity (S_{700} , S_{300} , and S_{150}), though GFDL's scores are modest. RASM has the highest skill score, and HadGEM produces the smallest biases. Most models have a too-salty bias in S_{150} . Because density is strongly

dependent on salinity, the density skill scores (ρ_{700} , ρ_{300} , and ρ_{150}) mirror the salinity skill scores.

Although these models are not necessarily designed for representing ocean-acoustics processes, a simple diagnostic for the suitability of these models for use in acoustical studies is their ability to represent sound speed. Sound speed, C , is computed by using the UNESCO 1983 polynomial (Fofonoff and Millard 1983), and depends on salinity, temperature, and pressure. All models score very well for representing C_{700} and skills are reduced only slightly for C_{300} and again for C_{150} . CESM scores the highest for all three ranges of C . The mean acoustic fields are fairly well reproduced in these models. However, acoustic propagation depends strongly on small-scale perturbations in C ; the suitability of these models for modeling these small-scale perturbations is beyond the scope of this subject.

The nine remaining skill scores are also for vertical profiles, but represent vertical gradients and scores are categorically lower. In all three depth-ranges, models have moderate scores in representing Brunt-Väisällä frequency as a function of depth (N_{700} , N_{300} , N_{150}). As with so many of the other observables, skill for N is reduced as the depth range narrows. RASM and CESM have the highest scores and smallest biases in all depth ranges. All models score poorly at representing the temperature gradients (dT/dZ_{700} , dT/dZ_{300} , and dT/dZ_{150}). These poor scores capture the essence of the previous discussion; models are unable to represent the temperature extremes of PSW and PWW. RASM scores the highest in the deeper two ranges for dT/dZ , and HadGEM scores the highest in the upper 150 m. Models score slightly better at representing salinity gradients (dS/dZ_{700} , dS/dZ_{300} , and dS/dZ_{150}), though improvements are still warranted.

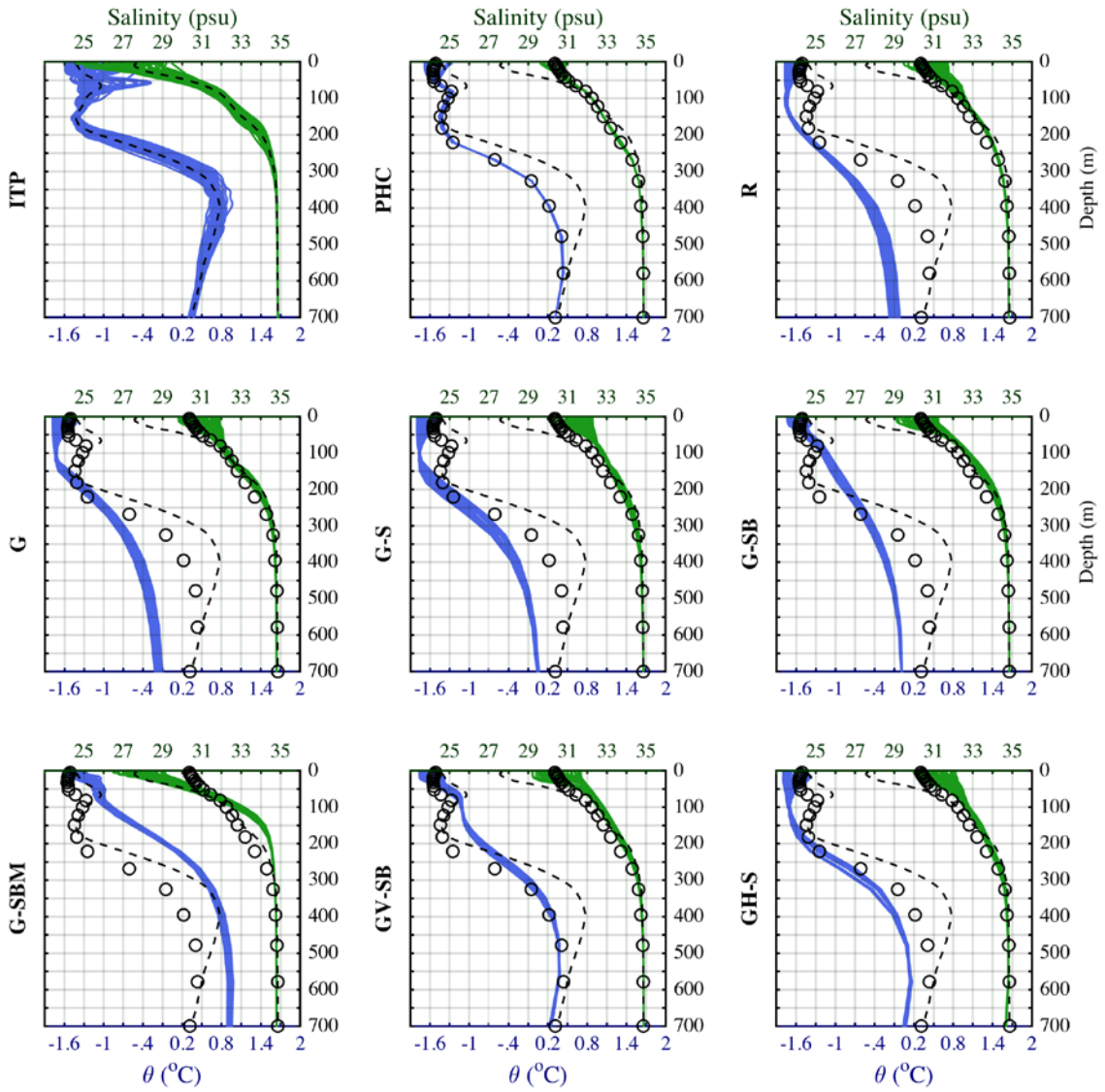
D. SENSITIVITY EXPERIMENTS WITH RASM

In the previous section, four global climate models (CESM, GFDL, HadGEM, and MPI) were evaluated along with RASM against climatology. In this section, results from several experiments using the RASM framework are analyzed in order to identify the configurations, parameterizations, and processes that can improve model representation of Arctic hydrography and lead to the smallest errors and highest skill

scores. In addition to comparing long-term means to climatology as was done in the previous section, model data will also be compared to ITP observations for a time series of 47 months from August 2005 through June 2009. This time period includes the highest quality ITP data available and the most results available from RASM runs. This time period also includes the extreme sea-ice minimum of September 2007, and represents a state of the upper Arctic Ocean that is significantly different from climatology (see e.g., Proshutinsky et al. 2009, Steele et al. 2010, Jackson et al. 2011, and Timmermans et al. 2014).

1. Profiles

Figure 3.10 provides a side-by-side comparison of temperature and salinity in the upper 700 m of the Central Canada Basin as measured by ITPs, recorded in PHC, and simulated by several RASM experiments. To avoid clutter, not all RASM experiments are plotted in Figure 3.10. The first panel shows ITP data. For each month between August 2005 and June 2009, a mean profile was computed for all data available within the bounds depicted in Figure 3.2. The ITP record shows strong variability in the upper 150 m, with surface temperatures varying between -1.6°C and -0.4°C and PSW temperatures varying between -1.3°C and 0°C . The PWW temperature remains very near -1.4°C , and there is some variability of approximately $\pm 0.25^{\circ}\text{C}$ in the thermocline and upper AW temperatures. Salinity variation is strongest near the surface, varying between 24 and 30 psu, but the range of variability decreases to about ± 0.5 psu in the PSW and PWW; there is almost zero variation in the AW salinity. The salinity profiles show two distinct haloclines: the upper halocline is at the base of the mixed layer which varies seasonally, and the permanent lower halocline separates the PWW from the AW (Jackson et al. 2010).



Each profile represents a single month during the period between August 2005 and June 2009. The grand mean of ITP data is plotted as dashed black lines, and PHC is plotted as circles.

Figure 3.10 Monthly Regional Mean Profiles of Potential Temperature (Blue) and Salinity (Green) from ITP Observations, PHC Climatology, and Seven RASM Experiments.

In the second panel, the twelve months of PHC data are plotted against the grand mean of ITP data; significant differences are readily apparent. It is beyond the scope of this paper to completely diagnose the sources of error between PHC and this period of ITP data, yet we must acknowledge the differences and their implications for models that

rely on climatology for initialization or restoration. The mean temperature of PHC (plotted as circles) at the surface is very near the same value of ITP data, but the variance is much lower in PHC. Surface temperatures in PHC vary between -1.7 and -1.2 °C. The PSW is nearly unchanging in PHC. The maximum temperature of PSW in PHC is approximately 0.3 °C colder and 25 m deeper than in ITPs. PWW temperatures are similar, but PHC AW is as much as 0.6 °C colder than in ITP. Surface salinity in PHC is nearly 3 psu higher than in ITPs and also shows much less variability. PHC does capture the two distinct haloclines, although both are much weaker in climatology. The lower halocline is also approximately 50 m deeper than observed.

Several RASM sensitivity experiments have been run as part of this study; Figure 3.10 compares seven of these experiments to climatology and observations. The values plotted here are computed by taking the mean of all model output profiles in the region that have sea ice thickness of at least 1.5 m. By removing the open water and thin ice areas, we can more directly compare model results to the observations made by ITPs, which are typically deployed in thicker ice and have not observed in open water conditions at that time period.

a. Fully coupled baseline (R)

The first experiment, case R, is the same one used for comparison with PHC data in the previous sections and it will be considered the baseline model to which one can compare further experiments. Case R uses the fully-coupled framework to exchange information between the ice, atmosphere, and ocean model components. (See Table 3.2 for RASM experiment summaries.) While its surface temperatures and salinities in Figure 3.10 have the same mean as PHC, they experience greater variance, though not as much variance as observed by ITPs. The surface salinities, like PHC, are on average 3 psu higher than observed by ITPs during the 2005–2009 time period. The upper halocline varies in depth from less than 25 m to around 50 m on a seasonal time scale, and a lower halocline with similar depth and strength as observed by ITPs is present in this experiment. The temperature profiles in case R, however, do not capture the structure of either PHC or ITPs as its seasonally varying surface temperature transitions to a constant

cold layer between 50 and 150 m. This water mass closely resembles PWW, but is too shallow and too fresh to truly represent PWW. No subsurface warm layer, i.e. PSW, is present. Additionally, the thermocline between Pacific and Atlantic waters is weaker than both climatology and ITP observations.

b. Coupled vs. forced (R – G)

The second experiment, case G, is identical in configuration as case R except the atmospheric and land hydrology components have been replaced by realistic atmospheric forcing from the CORE2 reanalysis. This case is much more computationally efficient, and determines the importance of atmospheric coupling on the representation of the upper ocean. Results from cases G and R are similar with only a few differences. Case G surface salinities are approximately 1 psu higher than case R, leading to a weaker upper halocline. Surface temperature variations are smaller in case G, but the lack of a subsurface temperature maximum is still apparent. The differences in the ocean column between the coupled (R) and un-coupled (G) cases are small and restricted to the surface, indicating that the limitations of representing the Pacific waters are not due to the atmosphere model component. Additionally, because case G is more computationally efficient, it can be used to run a greater number of sensitivity experiments.

c. Sea ice rheology (G – G-V)

Case G-V is identical to case G with the exception of changing the sea ice rheology physics scheme. Case G uses the more sophisticated elastic anisotropic plastic (EAP) rheology, while case G-V uses an earlier elastic viscous plastic (EVP) rheology. A more thorough discussion of the implications for these sea ice rheologies is discussed in Roberts et al. (2016). The differences in cases G and G-V are quite small below the surface, which is why G-V results are not included in Figure 3.10. Salinities in case G-V are only slightly higher than both PHC and G, and surface temperatures are lower. Also, or possibly as a consequence of these surface differences, the sub-surface gradients are weaker, and the lower thermocline is deeper. Because the improvements to the ocean are slight, the EAP option is incorporated in all the remaining experiments.

d. Ocean restoring during model spin-up (G – G-S)

Model spin-up may be partially to blame for the lack of a warm PWW. At the beginning of the initial spin-up, RASM is initialized with no sea ice at the surface, and allows ice to grow during model spin-up without any constraints on temperature or salinity. It is possible that the formation of realistic sea ice cover and the subsequent buoyancy input to the ocean model without any restoring to T/S climatology may produce a side effect persisting even after 100+ years of model integration (46-year spin-up plus 58-year production). The result could be increased surface salinities and vertical mixing, which both act to reduce vertical gradients of temperature and salinity. To test this hypothesis, case G-S is run using a 46-year spin-up that incorporates 30-day restoration to climatology of both temperature and salinity at all depths. Other than this new spin-up, case G-S has the same configuration as case G. In the 2000s there is a slight elevation of surface salinity in case G-S over G, and the AW temperature maximum is also slightly higher in case G-S. However, the limited improvement indicates that some other processes are limiting the representation of PSW and PWW.

e. Brine rejection parameterization (G-S – G-SB)

As discussed by Ngyuen et al. (2009) and Jin et al. (2012), different subgrid scale brine-rejection parameterization schemes will have significant consequences to the ocean water column. RASM case G-SB utilizes the brine-rejection scheme as presented in Jin et al. (2012), which produces very similar results to the scheme of Ngyuen et al. (2009), and produces near-surface salinities that are similar to those in PHC, yet not quite as low as observed by ITPs. Temperatures in the 50–350 m range are much warmer than in the previous RASM experiments discussed so far. As discussed by Ngyuen et al. (2009), this parameterization prevents excessive deepening of the MLD, which would act to mix out the warm PSW layer. However, there remains a positive temperature gradient below 100 m, albeit weaker than above 100 m, and this eliminates the previously cool layer found between 100 and 200 m. Ngyuen et al. (2009) also show that combining this brine rejection parameterization with a low background vertical diffusivity of $\nu = 10^{-6} \text{ m}^2 / \text{s}$ works best for their model. RASM uses the same low background vertical diffusivity of

$\nu = 10^{-6} \text{ m}^2 / \text{s}$, yet gradients still weaken over time. It is possible that this parameter may yet be too large, and Ngyuen et al. (2009) did not see significant gradient weakening after only 15 years of model run as compared to RASM's 104 years.

f. Surface momentum fluxes (G-SB – G-SBM)

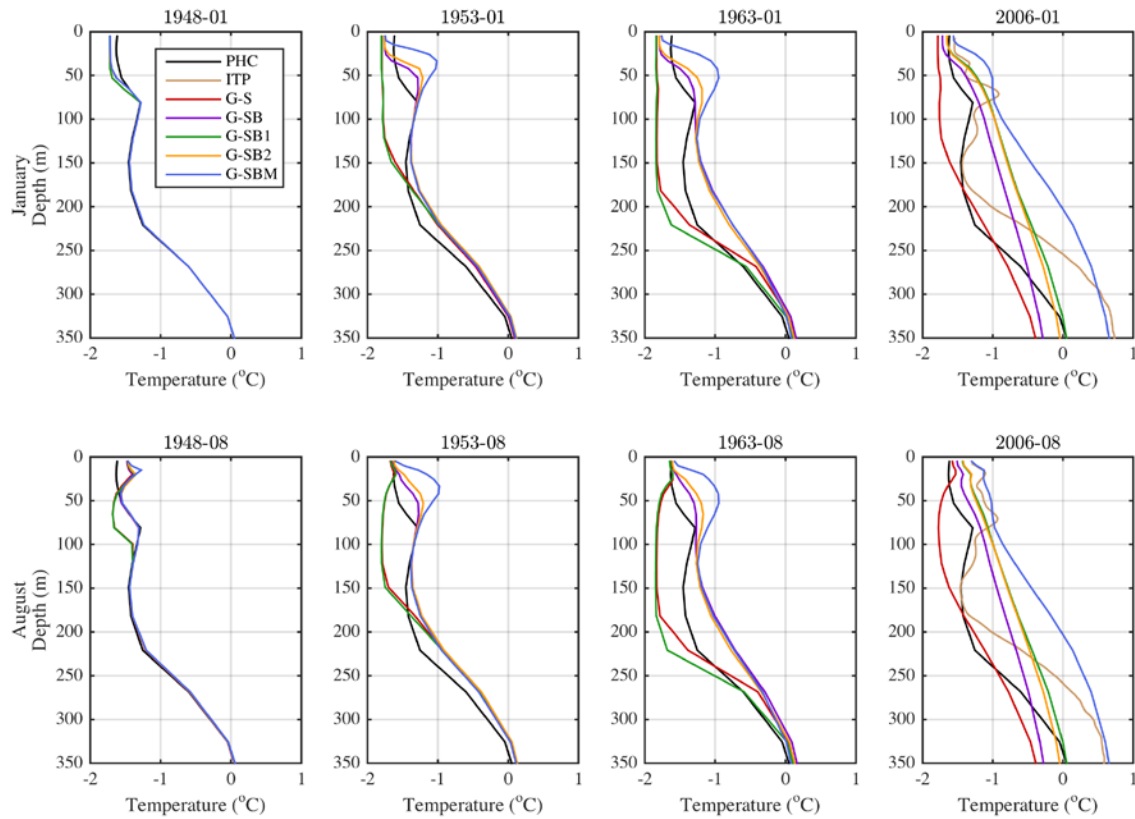
Several further experiments were conducted exploring parameters affecting momentum exchanges between the air-ice, ice-ocean, and air-ocean interfaces. These experiments were originally designed to test the sensitivity of sea ice drift and ocean currents to adjustments in the surface momentum balance; but ocean hydrography was also found to be quite sensitive to these changes.

RASM experiment G-SBM represents the best result of this group with respect to representing the thermohaline structure of the upper 700 m. In this experiment, sea ice strength has been increased, ice-ocean stress has been reduced by 50%, air-ice stress has been decreased by 25%, and the air-ocean stress has been increased 50%. These parameters are prescribed constants for the entire model domain, independent of the physical properties of sea ice such as ice thickness, roughness, or keel depths. By reducing ice-ocean and air-ice stresses we attempt to account for the changing ice properties, and by increasing air-ocean stress we account for a larger marginal ice zone. As a result, the upper 100 m temperatures and salinities are almost identical to the mean ITP values. Temperatures continue to increase in the PWW where they should decrease, though, but the AW temperature of this experiment is the closest to ITP observations. The positive temperature gradient between 100 and 200 m, and the continuous salinity gradient between the surface and 150 m (as opposed to distinct upper and lower haloclines) indicate that some process is yet missing from these experiments. Two likely candidates are lateral advection of Pacific waters from the Chukchi shelf, or simply limited vertical resolution of the model.

g. Time evolution of hydrography

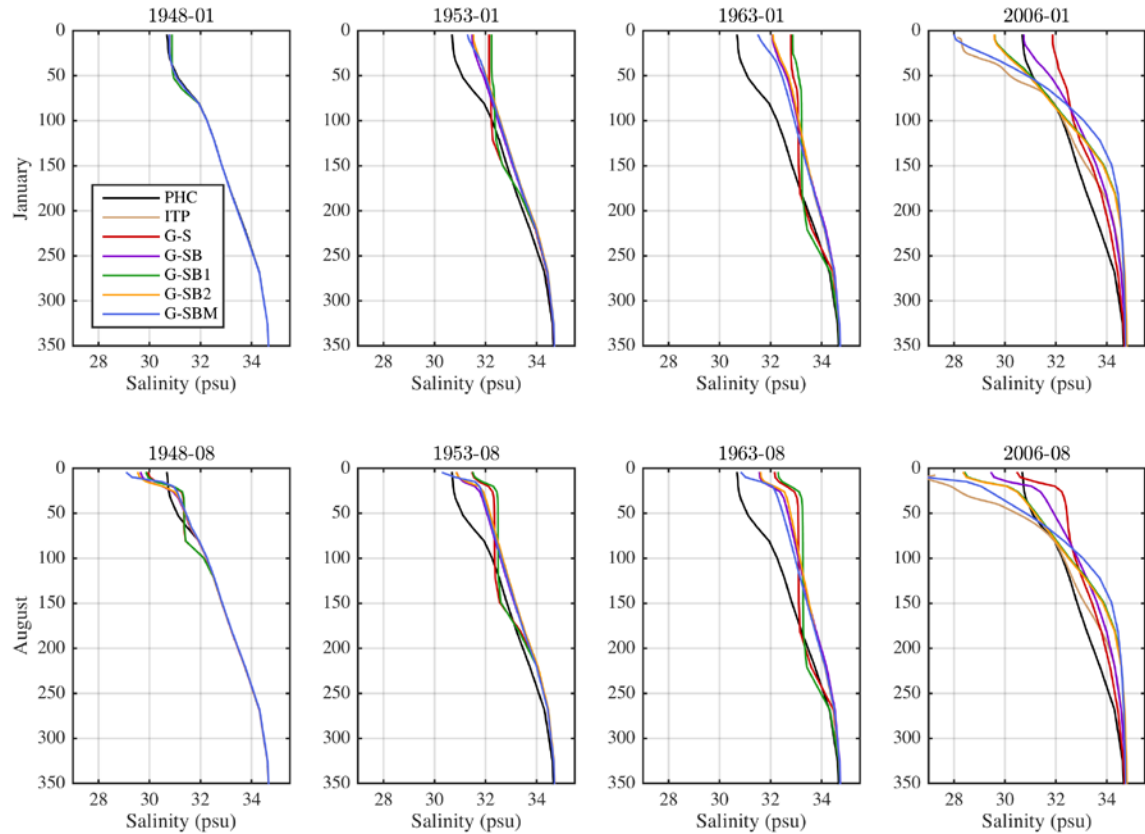
Before discussing the RASM experiments with increased vertical and horizontal resolution, it is worth revisiting the model spin-up. Several new experiments are run in

order to see how certain configurations affect the evolution of the upper ocean's hydrography. These new experiments are G-SB1, which uses a higher ice strength coefficient (C_f), and G-SB2, which reduces the convective diffusion and convective viscosity parameters from the default setting of 10000 in CESM-POP to 1000 originally set in POP. Figures 3.9a and 3.9b show the evolution of temperature and salinity at four times: immediately after model initialization (1948), five years later (1953), fifteen years later (1963), and in 2006 when ITP results are available. All experiments are initialized at January 1948 (Figures 3.11a and 3.11b, 1948–01) following the spin up as in case G-S with values similar to climatology, but by that August (1948–08) G-S and G-SB1 both show a low-temperature bias between 50 and 100 m. The isohaline layer between 25 and 75 m (Figure 3.11b, 1948–08) indicates that excessive mixing has occurred in these two experiments. By January 1953, both G-S and G-SB1 show mixed layers of over 125 m, the result of which is the loss of all heat from the PSW. The other experiments (G-SB, G-SB2, and G-SBM) retain a warm layer near 50 m and a halocline below 25 m. Why do some models suffer from excessive vertical mixing near the surface and others do not? First let's take a look at G-S, which suffers from excessive mixing, and G-SB, which does not. The only difference between these two experiments is that G-SB uses the brine rejection parameterization of Jin et al. (2012) and G-S does not. When the brines created during sea ice formation are more realistically redistributed in the upper water column, surface mixing is limited to more realistic depths and the PSW temperature maximum is retained.



PHC climatology is in black, and the mean ITP profile for that month is in brown (2006 only). The top row is January for each year and the bottom row is August for each year.

Figure 3.11a. Evolution of Temperature Profile After Model Initialization for Several RASM Experiments.



Notation is the same as Figure 3.11a.

Figure 3.11b. Evolution of Salinity Profile After Model Initialization for Several RASM Experiments.

However, G-SB1, which includes the brine rejection parameterization, also suffers from excessive mixing. G-SB1 uses a higher ice strength coefficient (C_f). A consequence of higher ice strength could be an increased salt flux from the ice to the ocean; this is likely caused by greater thermodynamic growth of ice since mechanical growth (e.g., from rafting and ridging) is reduced by the higher ice strength. An additional consequence of higher ice strength is faster ice drift speeds. Because more energy is required to deform the ice, more energy remains for kinetic energy, and ice drifts faster. Increased ice drift speed, combined with increased salt flux from the ice, result in increased vertical mixing in G-SB1.

Another set of parameters that are explored here are the convective diffusivity and convective viscosity. These parameters set the numerical diffusivity and viscosity only when a model grid cell becomes dynamically unstable and it undergoes convective mixing. In the default version of POP, following the CESM setting, these two parameters are set to 10000. By reducing these values by a factor of 10, as is done in G-SB2, and which was originally set in POP, the vertical extent of mixing due to convection is reduced. This is evidenced by the fact that the mixed layer depths are much more realistic in G-SB2 and that the PSW temperature maximum is retained (Figures 3.9a and 3.9b).

Some additional model limitations, e.g., under-representation of eddies, vertical resolution, etc., might accumulate over the multi-decadal integration time resulting in excessive smoothing of T and S profiles. As was discussed previously, the vertical gradients of temperature and salinity are gradually reduced as the model integrates in time. This can be seen in Figure 3.11a as experiments G-SB, G-SB2, and G-SBM all start with a PWW temperature minimum in 1948 and retain it through the next several years; however, by 2006 the PWW temperature minimum is gone. Further experimentation is required to identify which parameters are causing the vertical gradients to weaken over time. One possibility could be that, the horizontal flux of PWW from the Chukchi shelf and its spreading in the western Arctic is under-estimated due to insufficient model spatial resolution, hence the signature of PWW is continuously diminished over longer model integrations. Another factor could relate to insufficient vertical resolution, which is discussed next.

h. Increased vertical resolution (G-SB – GV-SB)

As Steele et al. (2011) point out, representation of the closely separated temperature maximum of PSW and temperature minimum of PWW may be limited due to vertical resolution in the model. Experiment GV-SB uses an expanded vertical grid that increases the number of levels from 45 to 60, with all of the additional levels between 20 and 200 m. Other than this increased vertical resolution, GV-SB is identical to experiment G-SB. Comparing these two panels on Figure 3.10, it can be seen that increased vertical resolution results in a slightly negative temperature gradient in the

PWW. Additionally, the temperature of the AW layer is more similar to PHC, although still lower than ITP observations. While these changes fall short of producing the exact profile found in nature, there is definitely an improvement here.

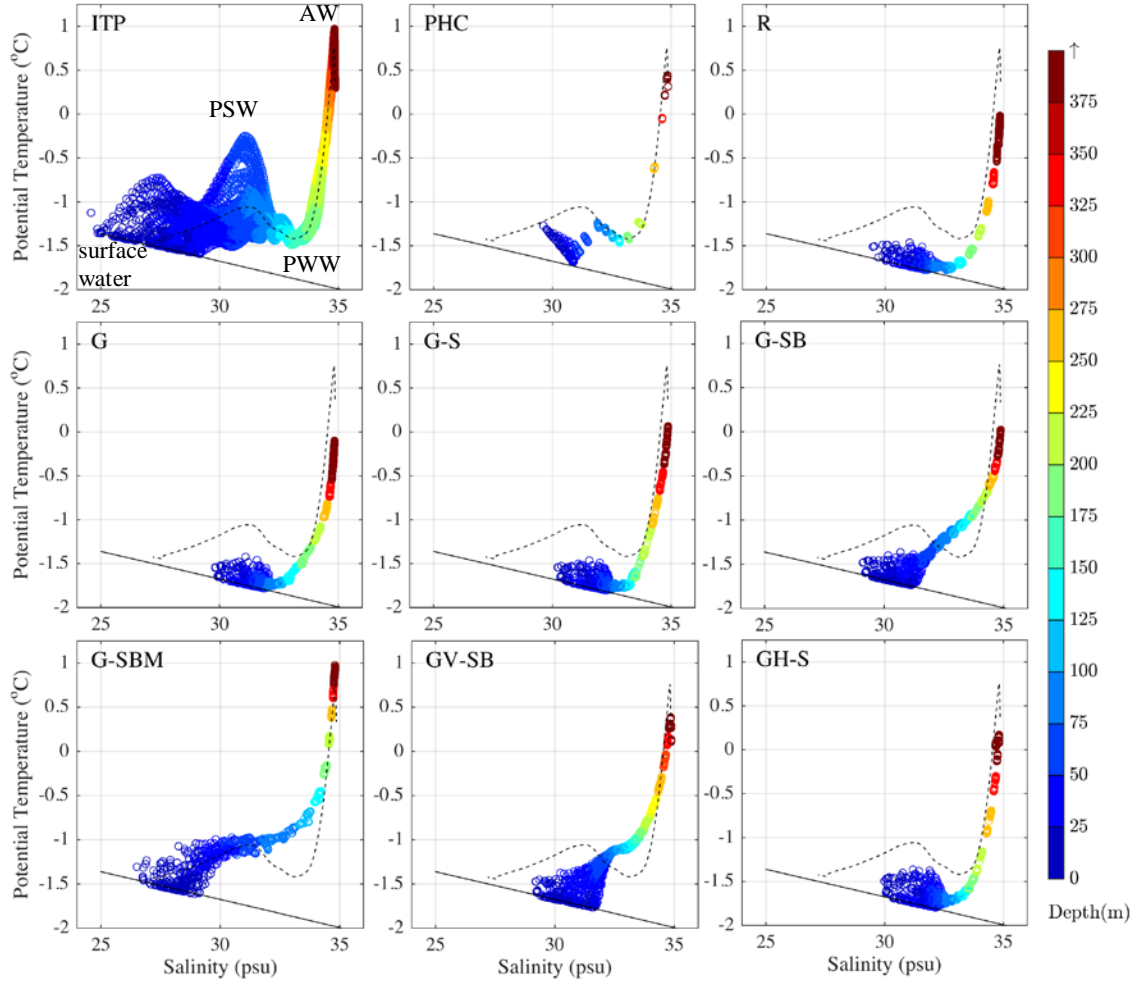
i. Increase horizontal resolution to $1/48^\circ$ (G-S – GH-S)

These experiments have all focused on local processes affecting the vertical water column. However, none of those experiments has appropriately represented both the PSW temperature maximum and the PWW temperature minimum. The next step is to address lateral advection of water-mass properties. In order for Pacific waters to reach the central Canada Basin, they must cross from the Chukchi and Beaufort shelves into the deep basin. It has been shown that mesoscale eddies play a large role in this shelf-basin exchange (Pickart et al. 2005, Spall et al. 2008, Watanabe et al. 2009). The baseline RASM experiment, case R, is configured with a horizontal grid spacing of $1/12^\circ$, or about 9 km in the central Arctic. At this resolution, smaller eddies (with a radius of $O(10\text{km})$) are not resolved. A series of experiments currently performed and evaluated increases the horizontal resolution of RASM to $1/48^\circ$ spacing, or about 2.4 km. This model set-up (here called GH-S) resolves eddies of radius less than 10 km (Maslowski et al. 2014), and is similar to experiment G-S. The thermohaline structure of GH-S is similar to G-S with two slight improvements: the top of the lower thermocline is deeper in GH-S at a more realistic depth of 200 m (as opposed to 150 m in G-S), and the cold temperature bias in the Atlantic water is reduced (Figure 3.10). With the 2.4 km configuration showing encouraging results and based on the guidance of this study, an experiment that incorporates higher horizontal resolution, higher vertical resolution, and a subgrid scale brine rejection parameterization is now under development.

2. T-S Diagrams

Here we discuss the performance of the RASM experiments by comparing their representation of temperature and salinity in T-S space (Figure 3.12). ITP data clearly show the unvarying AW with high salinity and temperature, the relatively consistent PWW with low temperature, and highly variable PSW and surface waters. The freezing temperature as a function of salinity is overlaid on these T-S diagrams, and it can be seen

that ITP data stays above this limit. PHC climatology shows the same basic structure of water masses, yet it does not capture the high variability and low near-surface salinities found in the ITP record. RASM experiments generally do not reproduce the same amount of variability as do the ITP data, but certain modifications do improve results beyond PHC. The water masses in are generally all too cold in the baseline case R, as well as in the G and G-S experiments. By incorporating the subgrid-scale brine rejection parameterization, as was done in case G-SB, a warmer and saltier water mass is retained in the depth range of PSW (50-150 m), though the PWW temperature minimum is not represented. Experiment G-SBM, which uses the adjusted surface momentum fluxes, very nearly recreates the surface, PSW, and AW layers, though still has a too-warm PWW. Experiment GV-SB results in a similar plot as G-SB, and GH-S results are similar to G-S.



Data is color coded by depth, the black dashed line is the mean of ITP data, and the black solid line is the freezing point.

Figure 3.12. T-S Diagrams of the Upper 700 m as Found in ITP, PHC, and RASM Experiments.

3. Bulk Property Time Series

Figure 3.13 shows time series of fifteen bulk properties derived from temperature and salinity results of the RASM experiments compared to PHC and ITP observations between August 2005, and June 2009. The methods of computing these values are the same as described in Section C.3, but instead of mean annual cycles, these results are for all 47 months in the time period of interest. It should be noted that the number of ITP observations in each month varies; in general, there are more observations in winter

months. Neither the heat content (HC_{700} , HC_{300} , HC_{150}), nor the fresh water content (FWC_{700} , FWC_{300} , FWC_{150}) of the upper ocean is observed by ITPs to have strong seasonal variability; though a seasonal cycle is produced in climatology and RASM experiments. HC_{700} includes the bulk of AW, which dominates the magnitude; hence, we should not expect seasonality. We should not expect a strong seasonality to HC_{300} , because the thermocline above the AW remains relatively constant. HC_{150} does show some seasonality, but inter-annual variability at that depth is as large as or larger than the seasonal changes. One would expect there to be strong seasonality to FWC, especially FWC_{150} given the freeze-melt cycle of sea ice. Since the top layer accounts for the bulk of the FWC magnitude, we would expect the seasonality to be present at all depth ranges. However, a seasonal cycle is not observed in ITP observations. This may be because the shallowest ITP observations are made around 5 – 7 m in depth. This is done to prevent the measuring device from colliding with the bottom of the sea ice. However, there may be a significant amount of fresh water that is not measured.

RASM experiments G-SB and GV-SB reproduce heat content values nearest to those of ITPs, though experiment G-SB underestimates HC_{700} . Experiment G-SBM overestimates heat content in all depth ranges, and all other RASM experiments greatly under estimate it. All experiments underestimate freshwater content at all depths.

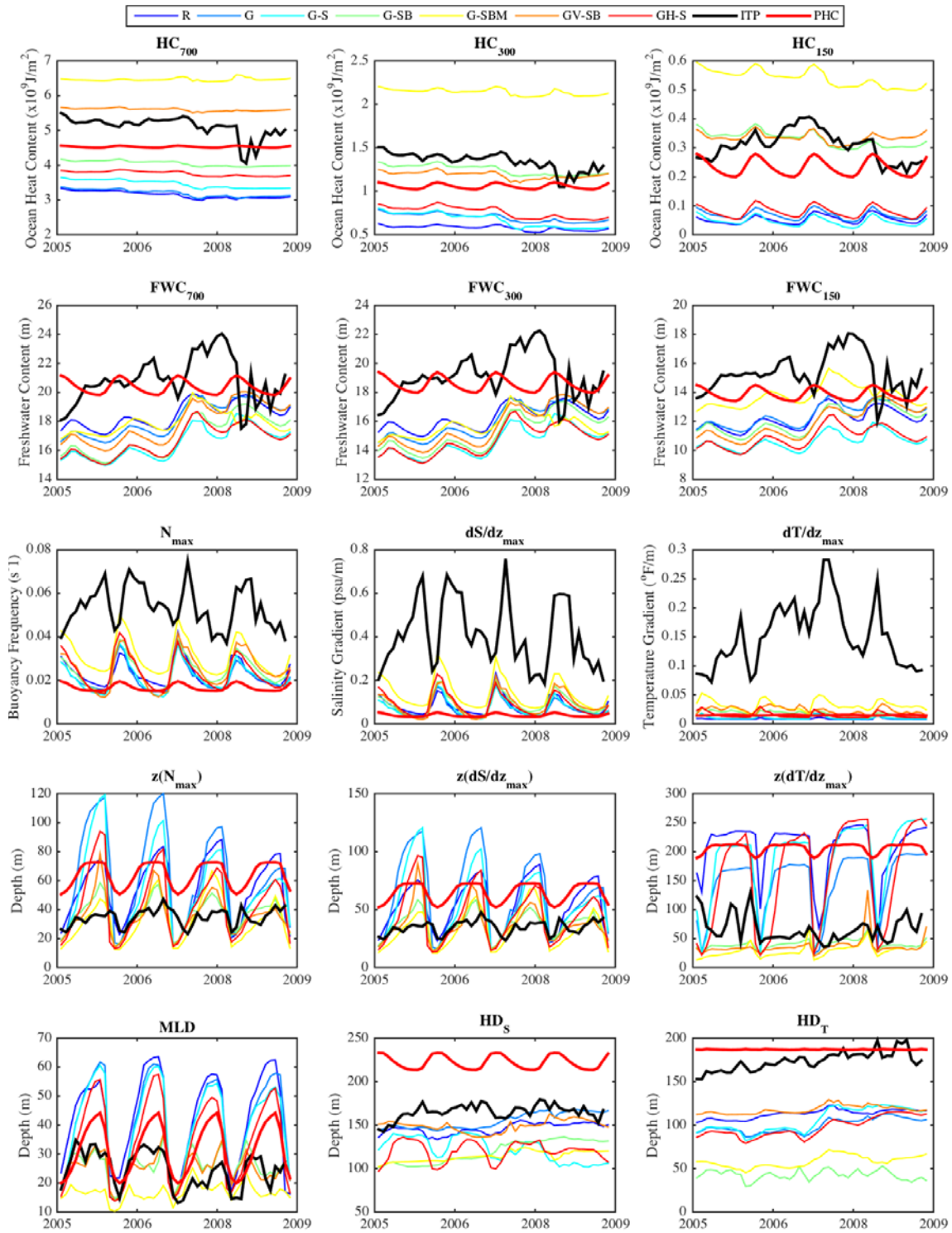


Figure 3.13. Time Series of RASM Experiments Water Mass Properties Compared to ITP Observations Between August 2005 and June 2009.

The amplitudes of maximum vertical gradients (dS/dz_{\max} and dT/dz_{\max}) and Brunt-Väisällä frequency (N_{\max}) are all under predicted by RASM experiments, though RASM does a better job of recreating these peaks than climatology (Figure 3.13).

The depth of maximum N , and the depth of maximum dS/dz , and the MLD are nearly identical in ITP observations, which should be no surprise since they are closely related. These values roughly follow a seasonal cycle between 15 and 35 m (Figure 3.13). Most RASM experiments show a greater variation with wintertime MLDs as deep as 65 m. As was discussed in Section D.1.g, several experiments exhibit excessive surface mixing as the model evolves. Experiments G-SB and GV-SB produce MLDs that are the most similar to those of ITPs, as they did not suffer from excessive surface mixing. Experiment G-SBM underestimates the winter MLD, indicating that this model configuration may not have enough surface mixing.

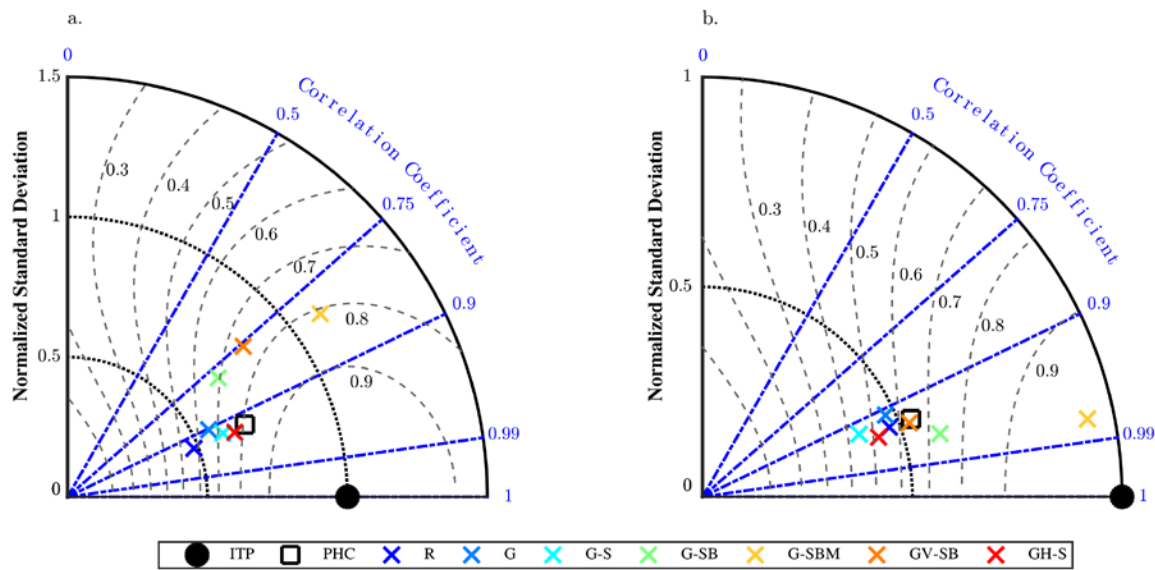
The depth of maximum dT/dz ($z(dT/dz_{\max})$) varies between 40 and 140 m in ITPs with no apparent seasonal cycle (Figure 3.13). The thermocline below the MLD and the thermocline below the PWW are similar in strength, so $z(dT/dz_{\max})$ could identify either feature. PHC places $z(dT/dz_{\max})$ at the depth of the lower thermocline; G-SB, G-SBM, and GV-SB place it at the depth of the MLD thermocline; the remaining experiments place it at different features at different times of year.

The salinity gradient based halocline depth (HD_s) stays near 175 m in ITP data, which is about 50 m shallower than in PHC (Figure 3.13). RASM experiments place the HD_s between 100 and 160 m, with experiments R, G, and GV-SB producing the closest results to ITPs. The good representation of HD_s in R and G is a consequence of the too-deep MLDs in those experiments and not an indication of good overall model performance. The temperature gradient based halocline depth (HD_T) is generally around 180 m in ITP, which is nearly the same as in PHC. All RASM experiments place the HD_T too shallow. This is a consequence of the too weak or missing PWW layer.

4. Taylor Diagrams and Skill Scores

Figure 3.14 displays Taylor Diagrams for T_{300} and S_{300} as represented by the seven discussed RASM experiments and PHC with statistics computed against ITP data. The

upper 300 m temperature representation in RASM experiments R, G, G-S, and GH-S all have a normalized standard deviation of between 0.5 and 0.7, indicating they represent about half as much of the variation of temperature in the vertical as observed by ITPs (Figure 3.14, left panel). However, these models' correlations are relatively high (greater than 0.9), indicating that the temperature extremes are near the correct depths. It is noteworthy that PHC has similar statistics as this group of experiments. The experiments that use the brine rejection parameterization, G-SB, G-SBM, and GV-SB, have standard deviations closer to that of ITPs, though their correlations are lower. These lower correlation scores are due to the lack of a PWW temperature minimum. The two RASM experiments with the highest skill score for upper 300 m temperature are GH-S and G-SBM.



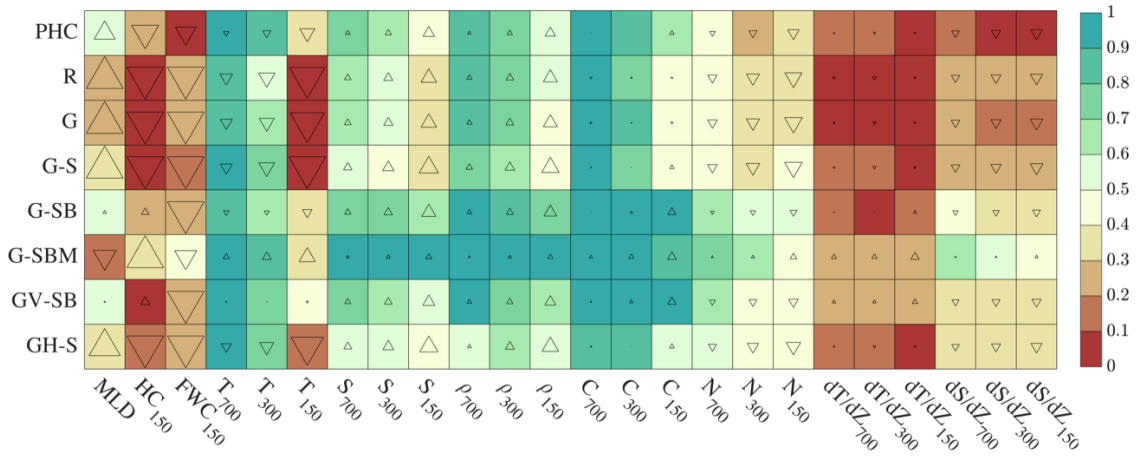
Annotations are the same as in Figure 3.8.

Figure 3.14. Taylor Diagrams For Upper Ocean Potential Temperature (a.) and Salinity (b.) of RASM Experiments Evaluated Against ITPs.

The upper 300 m salinity representation in RASM experiments is tightly clumped along with PHC at a standard deviation of 0.5 and correlations between 0.9 and 0.95. The one exception is experiment G-SBM, which has a high correlation (0.98) and normalized

standard deviation of nearly 1.0. This experiment set up has by far the best representation of upper ocean salinity.

Figure 3.15 presents the skill scores of each RASM experiment evaluated against the ITP record from August 2005 to June 2009 for the central Canada Basin region. For comparison, the PHC skill scores are also presented in Figure 3.15. The skills for the upper ocean properties of MLD, HC₁₅₀, and FWC₁₅₀ in all RASM experiments are poor, and biases are generally large. These same properties, however, are similarly represented poorly by PHC. Two experiments, however, G-SB and GV-SB, have smaller biases for MLD and HC₁₅₀. The low scores for these upper ocean properties are a result of the poor representation of upper 150 m temperatures (T₁₅₀); it is in this depth range that ITPs observe the largest variability. RASM scores are much higher for T₃₀₀ and T₇₀₀. The experiments using both brine rejection parameterization and ocean restoration during spin-up (G-SB, G-SBM, and GV-SB) all perform the best at representing T₁₅₀. These three experiments also score high for representing upper ocean salinity (S₇₀₀, S₃₀₀, S₁₅₀), though scores are slightly reduced for shallower depth ranges. Because density and sound speed both depend strongly on salinity in the Arctic, scores for ρ₇₀₀, ρ₃₀₀, ρ₁₅₀, C₇₀₀, C₃₀₀, and C₁₅₀ mirror those for salinity. As was found with the global climate models (Figure 3.9), skill scores for the vertical gradients (dT/dz, dS/dz, and N) are all low, though experiments G-SB and G-SBM perform slightly better. Most RASM experiments, especially G-SB, G-SBM, and GV-SB, offer substantial improvements of upper ocean hydrography over PHC.



Notation is the same as Figure 3.9.

Figure 3.15. Skill Scores for RASM Experiments and PHC Evaluated Against ITPs for August 2005 to June 2009.

E. SUMMARY AND CONCLUSIONS

Global climate models are important tools for exploring climate change, yet their representation of Arctic sea ice remains unsatisfactory. In this study, we used Taylor skill scores to quantitatively compare multiple model aspects simultaneously. Of the four global climate models that Massonnet et al. (2012) consider to best represent the rate of recent sea-ice decline, CESM, GFDL, HadGEM, and MPI, none reproduce the water mass structure observed in the central Canada Basin. These models represent the sub-surface layer as a gradual thermocline and halocline down to warm and salty AW rather than recreating the warm PSW and cold PWW layers. The high-resolution regional model, RASM, performs somewhat better than the lower-resolution global climate models, but still under-represents the heat content of the PSW layer. Before any of these models can be used to explore the role of ocean heat content in the decline of sea ice, improvements must be made in their representation of the thermohaline structure of the upper ocean.

Several experiments are conducted using the RASM framework in order to identify potential improvements. For a given horizontal and vertical resolution, several

factors were identified as improving the overall representation of PSW and PWW water mass properties. The inclusion of a sub-grid scale brine rejection parameterization such as used by Nguyen et al. (2009) and Jin et al. (2012) prevents excessive surface mixing which would penetrate into the PSW, removing that heat. Similarly, reducing the numerical diffusion and viscosity coefficients that govern convective mixing prevents the erosion of PSW heat. The parameters that determine coupling of horizontal momentum across the atmosphere-sea ice-ocean interface, as well as ice strength, are also identified as having a large effect on the vertical thermohaline structure.

Finally, two experiments were performed which increase horizontal and vertical resolution. By increasing the number of model levels from 45 to 60, some improvement was made in the representation of upper 300 m temperature; and by increasing the horizontal resolution from 1/12th degree to 1/48th degree grid spacing also resulted in slight improvements, likely due to more realistic lateral eddy fluxes. Despite these improvements, vertical gradients of temperature and salinity remain too weak. Therefore, errors exist in the magnitude and location of the PSW and PWW temperature extremes. Further experimentation is needed and ongoing to improve the representation of upper ocean hydrography in order to better understand ocean heat and its role in climate-scale changes in the Arctic region.

F. ACKNOWLEDGEMENTS

The support for this research comes from the U.S. Departments of Energy Regional and Global Climate Modeling (RGCM) program, the Office of Naval Research Arctic and Global Prediction (AGP) program and the National Science Foundation Arctic System Science (ARCSS) program. Computing resources were provided from the U.S. Department of Defense High Performance Computing Modernization Program (HPCMP). The views expressed in written materials or publications, and/or made by speakers, moderators, and presenters, do not necessarily reflect the official policies of the Naval Postgraduate School nor does mention of trade names, commercial practices, or organizations imply endorsement by the U.S. Government.

We acknowledge the World Climate Research Programme's Working Group on Coupled Modelling, which is responsible for CMIP, and we thank the climate modeling groups (listed in Table 3.1 of this paper) for producing and making available their model output. For CMIP the U.S. Department of Energy's Program for Climate Model Diagnosis and Intercomparison provides coordinating support and led development of software infrastructure in partnership with the Global Organization for Earth System Science Portals.

The Ice-Tethered Profiler data were collected and made available by the Ice-Tethered Profiler Program (Toole et al. 2011; Krishfield et al. 2008) based at the Woods Hole Oceanographic Institution (<http://www.whoi.edu/itp>)

IV. CONCLUSIONS

A. SUMMARY OF RESEARCH

The research conducted as part of this dissertation was carried out to: (i) enhance the U. S. Navy's understanding of environmental changes in the Arctic Ocean in response to climate change and (ii) their significance to the acoustic environment, as well as (iii) quantify modeling capabilities to represent them and (iv) guide future improvements needed to reduce uncertainty and advance model skill in prediction of future changes. There were two primary goals: to characterize the present hydrography and sound-speed structure of the western Arctic Ocean, and to evaluate the climate modeling community's ability to represent this hydrography. These goals were met by utilizing observations from, the Canada Basin Acoustic Propagation Experiment (CANAPE) pilot study, in the summer of 2015, and by evaluating the skill of global and regional climate models.

In the CANAPE pilot study, variations in temperature were observed in the upper 500 m that produced strong sound-speed anomalies. These variations were largely due to internal waves and spice variability. Internal waves with amplitudes on the order of 1.5 m were observed between 100 and 500 m depth; yet significant sound-speed variability was still observed in the upper 150 m. Spicy sound speed variability was lower than observed at lower latitudes, but still accounted for more sound speed variations than internal waves in the upper 200 m. The cause of these spicy sound speed variations is still not well understood. The structure of the spice was strongest at shallower depths, so future studies should investigate the source of isopycnal sound-speed anomalies near the surface. Based on the limited CTD data collected during the CANAPE pilot, very large variations in upper 150 m temperature and sound speed were observed at locations less than 100 km apart. The source of this variability is not certain, yet it is likely due to eddies, local surface heat fluxes, or upstream variations in the source waters or their advective pathways. The full CANAPE experiment, to be conducted between summer 2016 and summer 2017, should shed some light on this large-scale variability. Additionally, deploying more ocean-sensing instruments suited for the near-freezing conditions of the

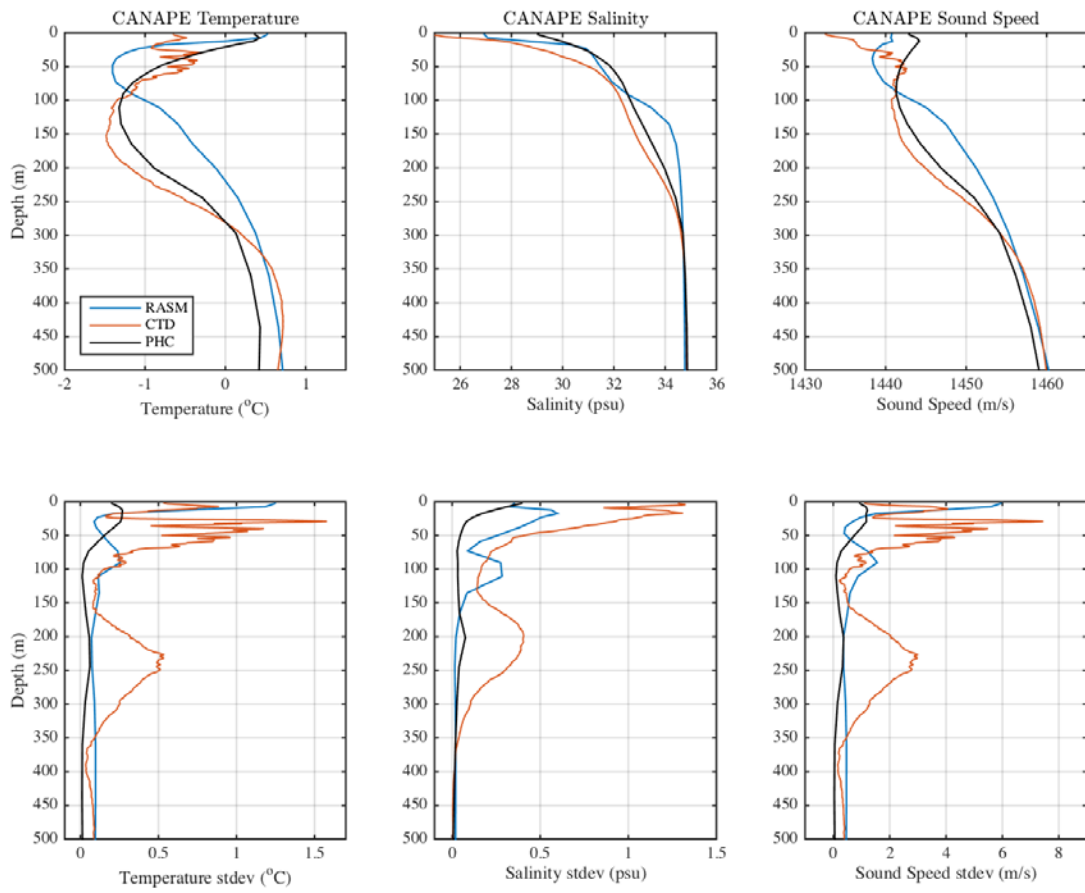
marginal ice zone would provide more evidence for the source of these near-surface sound speed variations.

From a modeling perspective, this dissertation has found that no global climate model, nor any current configuration of RASM, is successful in capturing the mean state of hydrography in the western Arctic Ocean. Improvements have been identified, but more experiments are required in order to utilize coupled models to simulate the small-scale variability in temperature and salinity that give rise to the acoustic variability observed in CANAPE. Based on the promising results of the experiments conducted for this project, several avenues for improvement have been identified. Increasing the number of vertical levels in the ocean model component improved the representation of the upper 150 m temperature and salinity profiles, as did increasing the horizontal resolution. The biggest improvements came from parameterizations that resulted in adequate but not excessive surface mixing. Excessive surface mixing acted to remove heat and add salt to the Pacific Summer Water (PSW) layer, resulting in significant errors in the upper 150 m hydrography. It would be worthwhile to investigate other methods of modeling surface momentum exchange, such as using time/space varying, physics-based, model-predicted ice deformation and form drag. Ongoing developments are underway to incorporate these improvements into the higher resolution versions of RASM, and future experiments are being designed and conducted to improve representation of ocean hydrography.

B. IMPLICATIONS FOR ACOUSTIC PROPAGATION

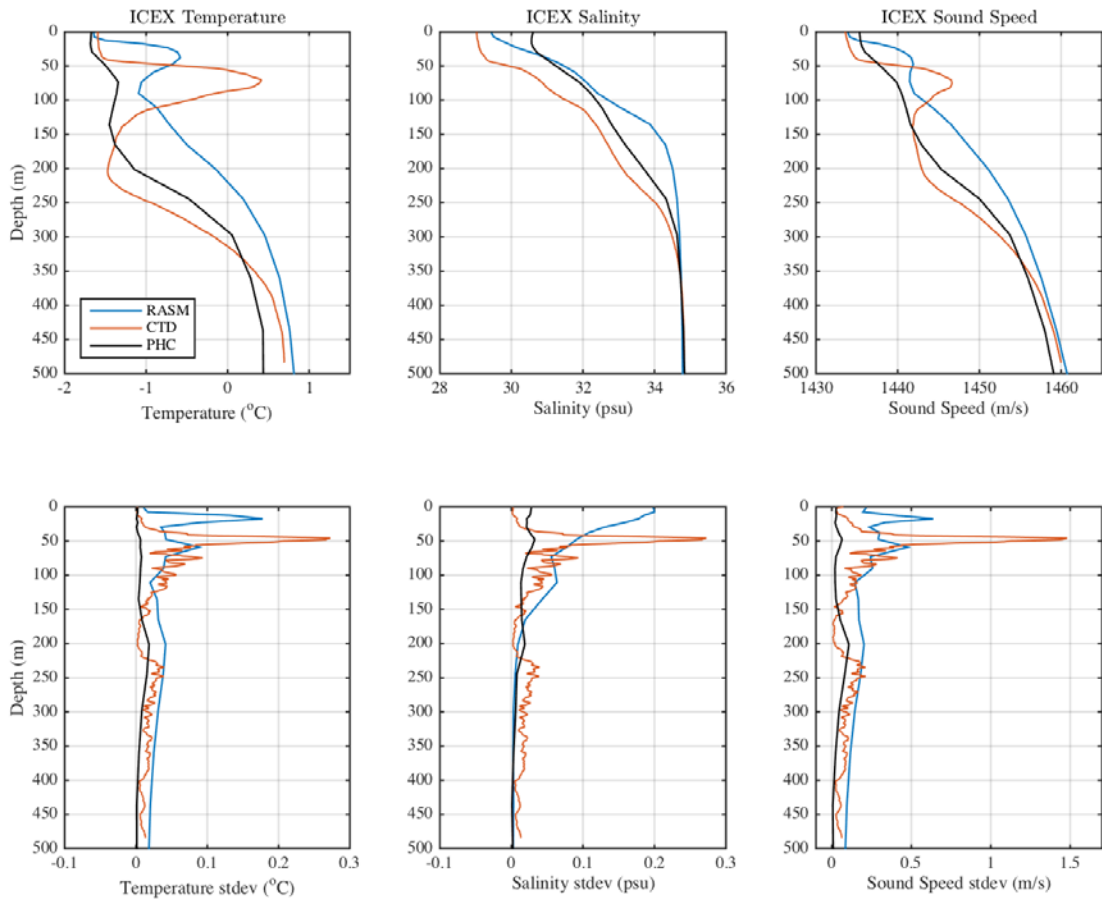
One of the overall goals for this project was to advance the Navy's understanding of the changing Arctic with regards to the acoustic environment. During the CANAPE pilot, observations were made of the sound-speed structure during the summer of 2015 in the marginal ice zone; during the Navy's Ice Exercise (ICEX), similar observations were made winter of 2016 under pack-ice. Theses by Pearson (2016) and Nelson (2016) analyzed the acoustic environment during those two experiments. However, models must be used to make projections for future climate states and their acoustic environments, especially on large spatial scales. Figures 4.1a and 4.1b present a side-by-side comparison of observations and RASM output (experiment G-SBM) for the locations of

CANAPE (figure 4.1a) and ICEX (figure 4.2b). Because at present RASM output is not available for dates beyond 2009, the model months chosen to display are from 2007 and 2008, which had similar ice coverage as observation years 2015 and 2016. In this figure, the model limitations identified in chapter 3 are evident. However, RASM offers substantial improvements over PHC climatology in representing the magnitude of variance of both the hydrography and the sound-speed structure (figure 4.1, bottom row), though modeled variability was still less than observed. The sound-speed profiles of RASM and observations show similar structure, though these differences would certainly be reduced as RASM's representation of upper ocean temperature and salinity are further improved.



Observations are plotted in orange, RASM model output in blue, and climatology in black. CTD data are from the CANAPE pilot study conducted in August 2015; RASM data are from August 2007 in the CANAPE region

Figure 4.1a. Profiles of CANAPE Temperature (top left), Salinity (top middle), and Sound Speed (top right) and Their Standard Deviations (bottom row).

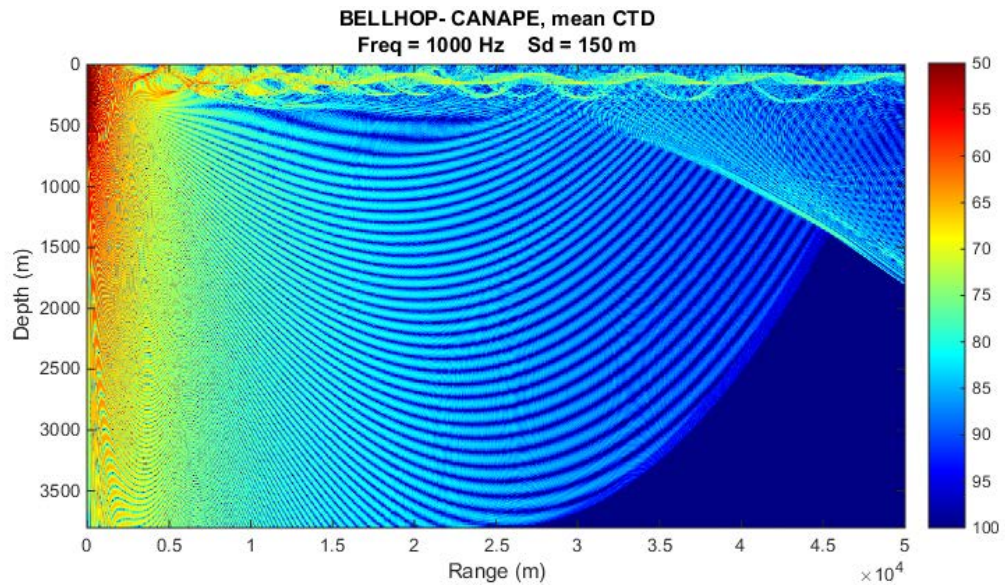


Observations are plotted in orange, RASM model output in blue, and climatology in black. CTD data are from ICEX conducted in March 2016; RASM data are from March 2008 in the ICEX region.

Figure 4.1b. Profiles of ICEX Temperature (top left), Salinity (top middle), and Sound Speed (top right) and Their Standard Deviations (bottom row).

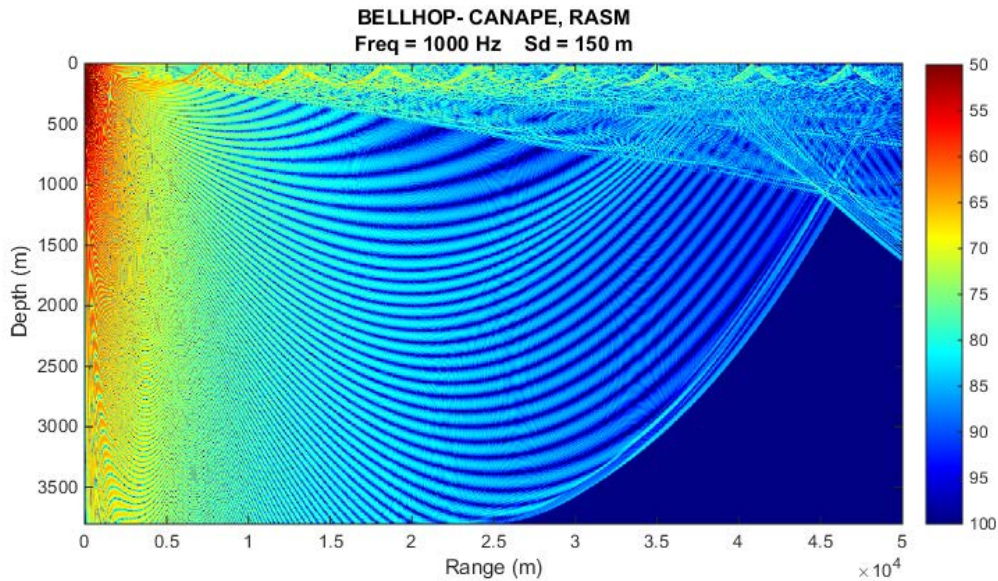
A very important feature was observed in some of the CANAPE and ICEX CTD profiles: a sub-surface sound-channel (Pearson 2016, Nelson 2016). Figures 4.2 and 4.4 show acoustic transmission loss of a 1000 Hz signal, as modeled by the Bellhop acoustic transmission model, when using the observed temperature and salinity to derive a range-independent sound-speed field. Generally, sound speed increases with depth in the Arctic so sound generated at most depths is refracted upwards. The sound would then reflect off the surface and continue a pattern of deep-ocean refraction and surface reflection. The presence of sea ice complicates the surface reflection, introducing significant scattering

and absorption losses. However, a sound-speed maximum, created by the PSW temperature maximum, was observed at around 50–80 m in both CANAPE and ICEX. This sound-speed maximum refracts sound generated below it back down away from the surface. Below this is the cold PWW layer, which forms a sound-speed minimum. The PSW sound-speed maximum above the PWW sound speed-minimum results in an acoustical wave-guide, which would trap sound energy in a so-called “sound channel.” Depending on frequency, sound generated in the PWW sound channel would be refracted about the sound-speed minimum and would not interact with the surface, thereby reducing the surface attenuation. In both field studies, a sub-surface sound-channel reduces transmission loss near 150 m in depth. The sound-speed fields derived from RASM output (Figures 4.3 and 4.5) do not include a sound-channel identical to that observed. However, RASM does possess a weak sound-speed minimum at a shallower depth; when the sound source is placed at this depth, the signal is trapped in a sound channel (Figures 4.6 and 4.7).



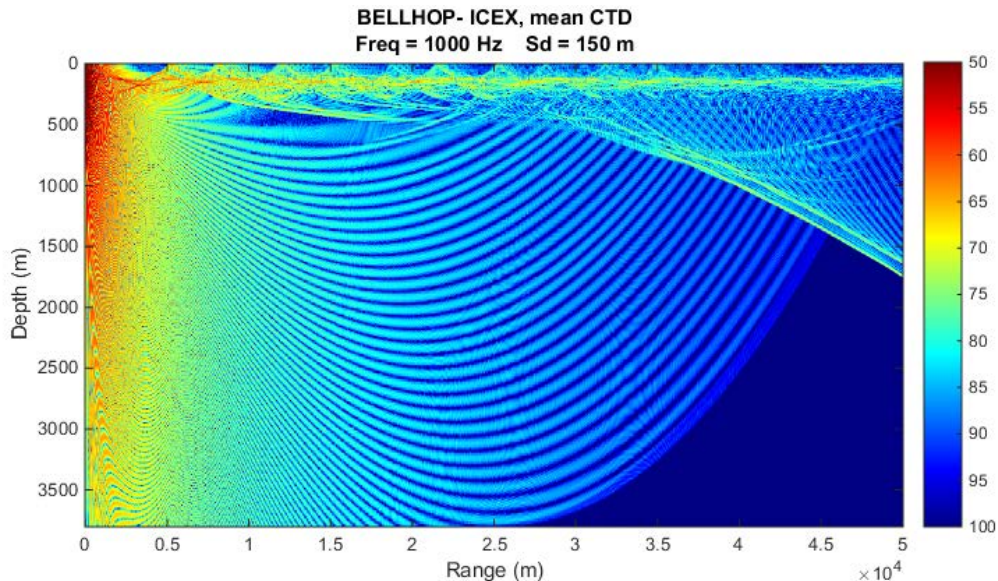
Sound speed field is derived from the mean CTD measurements during the CANAPE pilot study in August 2015. A sound-channel, in which transmission loss is significantly reduced, is located near 150 m depth. A surface duct, in which sound reflects off the surface, is also present.

Figure 4.2. Modeled Transmission Loss for a 1000 Hz Acoustic Source at 150 m Depth During CANAPE using CTD Observations



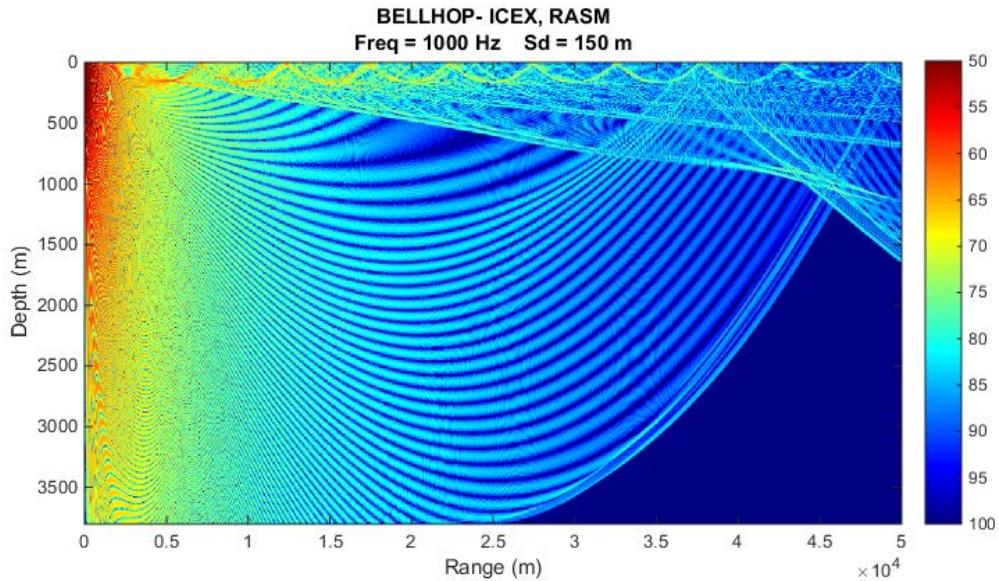
Sound speed field is derived from the mean August 2008 RASM output from the same geographic region as the CANAPE pilot. A surface duct, in which sound reflects off the surface, is present, but not the sub-surface sound-channel that was observed (Figure 4.2).

Figure 4.3. Modeled Transmission Loss for a 1000 Hz Acoustic Source at 150 m Depth During CANAPE using RASM output.



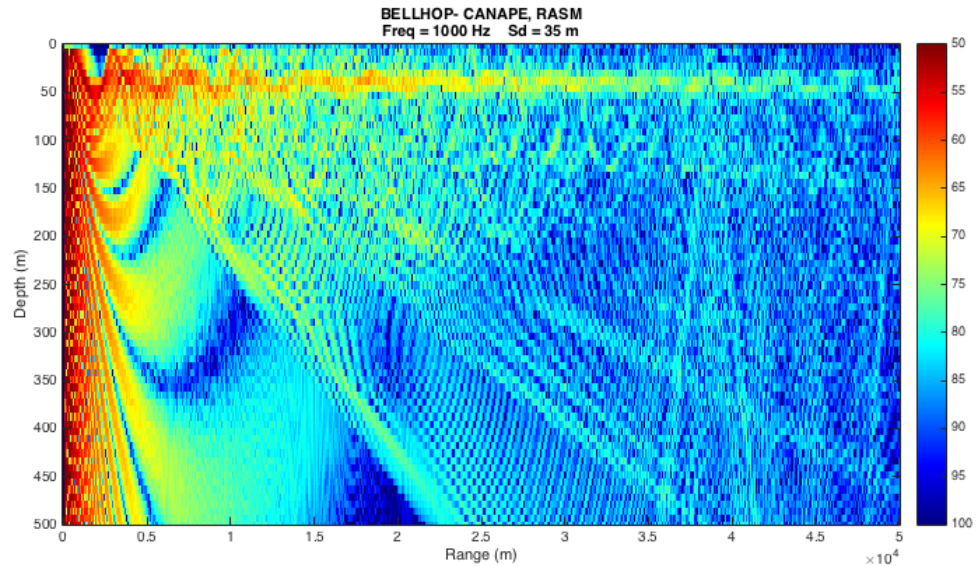
Sound speed field is derived from the mean CTD measurements during the ICEX in March 2016. A sound-channel, in which transmission loss is significantly reduced, is located near 150 m depth. A weak surface duct, in which sound reflects off the surface, is also present

Figure 4.4. Modeled Transmission Loss for a 1000 Hz Acoustic Source at 150 m Depth During ICEX using CTD Observations.



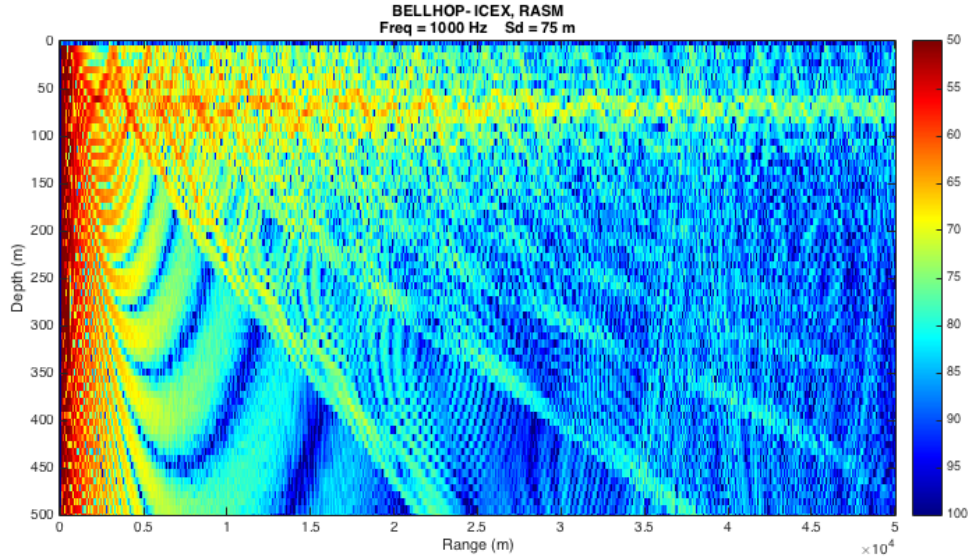
Sound speed field is derived from the mean March 2009 RASM output from the same geographic region as the ICEX. A surface duct, in which sound reflects off the surface, is present, but not the sub-surface sound-channel that was observed (Figure 4.4)

Figure 4.5. Modeled Transmission Loss for a 1000 Hz Acoustic Source at 150 m Depth During ICEX using RASM Output.



Sound generated at a depth of 35 m would be trapped in a sound channel. The range of depths displayed is limited to the upper 500 m to highlight the relevant depth range.

Figure 4.6. Modeled Transmission Loss for Same RASM Output (CANAPE) as Figure 4.3 but with the Source at 35 m.



Sound generated at a depth of 75 m would be trapped in a sound channel. The range of depths displayed is limited to the upper 500 m to highlight the relevant depth range

Figure 4.7. Modeled Transmission Loss for Same RASM Data (ICEX) as Figure 4.5 but with the Source at 75 m.

The PWW sound channel and PSW sound-speed maximum create a unique tactical situation. A sound source near the surface would only be detectable at long ranges in open water or under very smooth sea ice; however, a sound source in the PWW sound channel would be detectable at long ranges regardless of the surface conditions.

The PWW duct is not consistent in time, location, or strength. During ICEX, which was conducted under pack-ice in the winter of 2016, Nelson (2016) found a stable PWW duct with a sound-channel axis at approximately 150 m depth. However, Pearson (2016), during the CANAPE pilot study conducted in the marginal ice zone in the summer of 2015, found that the PSW sound-speed maximum was highly variable and sometimes non-existent. In these conditions, the acoustic propagation conditions would vary substantially in time and space. Undersea forces would need to frequently sample their environment at many locations to make reasonable predictions of sensor performance and acoustic vulnerabilities. High-resolution and more-accurate coupled climate model simulations would allow acoustic operators the ability to know the location, strength, and variability of the acoustic conditions, greatly enhancing their mission success.

C. RECOMMENDATIONS

As the Arctic Ocean continues to change and human activity in the region expands, we should consider the next steps to take in order to safeguard U. S. interests and activities in the region. This dissertation has identified improvements that have been demonstrated in RASM, as well as areas that should be further investigated. The guidance from RASM experiments should be utilized by the climate modeling community to improve global climate and Earth system models, which provide the scientific basis for international policies on climate change. To support modeling efforts, observational studies should target the upper 150 m, especially in the expanding Arctic marginal ice zones, to identify the spatial and temporal variability of ocean hydrography.

The acoustic analysis conducted in this dissertation was based on heuristic models of sound propagation and limited numerical acoustic modeling. To truly understand the significance and variability of the PSW and PWW acoustic features, further in-situ acoustic experiments, such as CANAPE, should be conducted.

This dissertation focused solely on the implications of the background hydrography and resulting sound-speed structure. There are several other important components of the acoustic environment that warrant study. The effects of varying sea ice properties, such as age, on sound attenuation are not yet well known, and a changing ice cover will likely introduce further uncertainty with respect to the ocean-ice acoustic interface. A warming climate has also resulted in overall thinner sea ice, more open water seasonally, more biological activity, and more human activity. All of these are likely to increase the ambient noise environment.

The scientific community is not alone in studying the Arctic. Prior to and during operations, Naval undersea forces in the Arctic should conduct thorough in-situ sampling to determine the strength and variability of the PSW and PWW sound-speed features. The Navy METOC community should also focus efforts on sampling (in-situ and remotely) the marginal ice zone in order to improve battlespace awareness.

LIST OF REFERENCES

Alexander, P., A. Duncan, N. Bose, and D. Smith, 2013: Modelling acoustic transmission loss due to sea ice cover. *Acoustics Australia*, **41**(1), 79–87.

Arctic Council, 2009: *Arctic Marine Shipping Assessment 2009 Report*. Arctic Council, Norwegian Chairmanship, Oslo, Norway, 290 pp.

Bellouin, N., W. J. Collins, I. D. Culverwell, P. R. Halloran, S. C. Hardiman, T. J. Hinton, C. D. Jones, R.E. McDonald, A. J. McLaren, F. M. O'Connor, and M. J. Roberts, 2011: The HadGEM2 family of met office unified model climate configurations. *Geoscientific Model Development*, **4**(3), 723–757.

Berkman, P. A., and O. R. Young, 2009: Governance and environmental change in the Arctic Ocean, *Science*, **324**, 339–340.

Bourgain, P. and J. C. Gascard, 2011: The Arctic Ocean halocline and its interannual variability from 1997 to 2008. *Deep Sea Research Part I: Oceanographic Research Papers*, **58**(7), 745–756.

Buck, B. M., and C. R. Greene, 1964: Arctic deep-water propagation measurements. *J. Acoust. Soc. Am.*, **36**(8), 1526–1533.

Coachman, L. K., and C. A. Barnes, 1961: The contribution of Bering Sea water on the Arctic Ocean, *Arctic*, **14**, 146–161.

Cornuelle, B. D., C. Wunsch, D. Behringer, T. G. Birdsall, M. G. Brown, R. Heinmiller, R. A. Knox, K. Metzger, W. H. Munk, J. L. Spiesberger, R. C. Spindel, D. C. Webb, and P. F. Worcester, 1985: Tomographic maps of the ocean mesoscale. 1 Pure acoustics. *J. Phys. Oceanogr.*, **15**, 133–152.

Colosi, J. A., T.F. Duda, T.T. Lin, J. Lynch, A. Newhall, and B.C. Cornuelle, 2012: “Observations of sound speed fluctuations on the New Jersey continental shelf in the summer of 2006,” *J. Acoust. Soc. Am.*, **131**(2), 1733–1748.

Colosi, J. A., L. J. Van Uffelen, B. D. Cornuelle, M. A. Dzieciuch, P. F. Worcester, B. D. Dushaw, and S. R. Ramp, 2013: Observations of sound-speed fluctuations in the western Philippine Sea in the spring of 2009. *J. Acoust. Soc. Am.*, **134**(4), 3185–3200.

Colosi, J., 2016: *Sound Propagation through the Stochastic Ocean*. Cambridge University Press.

Cornuelle, B. D., C. Wunsch, D. Behringer, T. G. Birdsall, M. G. Brown, R. Heinmiller, R. A. Knox, K. Metzger, W. H. Munk, J. L. Spiesberger, R. C. Spindel, D. C. Webb, and P. F. Worcester, 1985: Tomographic maps of the ocean mesoscale. Part 1: Pure acoustics. *J. Phys. Oceanogr.*, **15**, 133–152.

Cryosphere Today, accessed 2016. [Available online at <http://arctic.atmos.uiuc.edu/cryosphere/>]

Crystal Cruises, cited 2016: Northwest Passage Explorer. [Available online at <http://www.crystalcruises.com/northwest-passage-cruise>].

Department of Environment and Natural Resources, cited 2016: Trends in shipping in the Northwest Passage and the Beaufort Sea. [Available online at <http://www.enr.gov.nt.ca/state-environment/73-trends-shipping-northwest-passage-and-beaufort-sea>].

Department of the Navy, Memorandum for Distribution, 2009: Task Force Climate Change. [Available online at <http://greenfleet.dodlive.mil/files/2010/09/Task-Force-Climate-Change-charter.pdf>].

Deser, C., and H. Teng, 2008: Evolution of Arctic sea ice concentration trends and the role of atmospheric circulation forcing, 1979–2007. *Geophys. Res. Lett.*, **35**, L02504, doi:10.1029/2007GL032023.

DiMaggio, D., 2012: The role and variability of ocean heat content in the Arctic Ocean: 1948–2009. Thesis, Department of Oceanography, Naval Postgraduate School, 196 pp., [Available online at: <http://hdl.handle.net/10945/42611>].

DiMaggio, D., J. Colosi, et al., 2016 (in prep.): Observations of the upper ocean thermohaline structure and variations in the Canada Basin, Summer 2015.

DiMaggio, D., W. Maslowski, et al., 2016 (in prep.): Evaluation and sensitivity of climate model skill at representing upper Arctic Ocean hydrography.

DiNapoli, F. R., and R. H. Mellen, 1985: Low frequency attenuation in the Arctic Ocean. Office of Naval Research Technical Memo TM-851130, 22 pp.

Dosser, H. V., and L. Rainville, 2016: Dynamics of the changing near-inertial internal wave field in the Arctic Ocean. *J. Phys. Oceanogr.*, **46**(2), 395–415.

Dushaw, B. D., B. D. Cornuelle, P. F. Worcester, B. M. Howe, and D. S. Luther, 1995: Barotropic and baroclinic tides in the central North Pacific Ocean determined from long-range reciprocal acoustic transmission. *J. Phys. Oceanogr.*, **25**(4), 631–647.

Dushaw, B. D., P. F. Worcester, and M. A. Dzieciuch, 2011: On the predictability of mode-1 internal tides. *Deep Sea Res. I*, **58**, 677–698.

DuVivier, A. K., and J. J. Cassano, 2013: Evaluation of WRF model resolution on simulated mesoscale winds and surface fluxes near Greenland. *Mon. Wea. Rev.*, **141**, 941–963.

Dzieciuch, M. A., W. H. Munk, and D. Rudnick, 2004: Propagation of sound through a spicy ocean, the sofar overture. *J. Acoust. Soc. Am.*, **116**(3), 1447–1462.

Executive Intelligence Review, 2016: U.S./Russian Military Focus on the Arctic, EIRNS Press Release. [Available online at http://www.larouchepub.com/pr/2016/161021_arctic_strategy.html].

Ferarri, R., and D. L. Rudnick, 2000: Thermohaline variability in the upper ocean. *J. Geophys. Res.*, **105**, 16857–16883, doi:10.1029/2000JC900057.

Flatte, S. M., R. Dashen, W. Munk, K. Watson, and F. Zachariasen, 1979: *Sound Transmission Through a Fluctuating Ocean*. Cambridge University Press. 295 pp.

Fofonoff, P. and R. C. Millard, Jr., 1983: Algorithms for computation of fundamental properties of seawater, 1983. *Unesco Technical Paper in Marine Science*, No. **44**, 53 pp.

Francis, J. A., E. Hunter, J. R. Key, and X. Wang, 2005: Clues to variability in Arctic minimum sea ice extent. *Geophys. Res. Lett.*, **32**, L21501, doi:10.1029/2005GL024376.

Gallaher, S. G., T. P. Stanton, W. J. Shaw, S. T. Cole, J. M. Toole, J. P. Wilkinson, T. Maksym, and B. Hwang, 2016: Evolution of a Canada Basin ice-ocean boundary layer and mixed layer across a developing thermodynamically forced marginal ice zone, *J. Geophys. Res. Oceans*, **121**, 6223–6250, doi:10.1002/2016JC011778.

Galley, R. J., D. Babb, M. Ogi, B. G. T. Else, N.-X. Geilfus, O. Crabeck, D. G. Barber, and S. Rysgaard, 2016: Replacement of multiyear sea ice and changes in the open water season duration in the Beaufort Sea since 2004, *J. Geophys. Res. Oceans*, **121**, 1806–1823, doi:10.1002/2015JC011583.

Garrett, C., and W. Munk, 1971: Internal wave spectra in the presence of fine-structure. *J. Phys. Oceanogr.*, **1**, 196–202.

Gavrilov, A. N., and P. N. Mikhalevsky 2002: Recent results of the ACOUS (Arctic Climate Observations using Underwater Sound) Program. *Acta Acustica united with Acustica*. **88**, 783–791.

Gavrilov, A. N., and P. N. Mikhalevsky 2006: Low-frequency acoustic propagation loss in the Arctic Ocean: results of the Arctic climate observations using underwater sound experiment. *J. Acoust. Soc. Am.*, **119**(6), 3694–3706.

Griffies, S. M., M. Winton, L. J. Donner, L. W. Horowitz, S. M. Downes, R. Farneti, A. Gnanadesikan, W. J. Hurlin, H. C. Lee, Z. Liang, and J. B. Palter, 2011: The GFDL CM3 coupled climate model: characteristics of the ocean and sea ice simulations. *Journal of Climate*, **24**(13), 3520–3544.

Guthrie, J. D., J. H. Morison, and I. Fer, 2013: Revisiting internal waves and mixing in the Arctic Ocean. *J. Geophys. Res.*, **118**, 3966–3977, doi:10.1002/jgrc.20294.

Holloway, G., F. Dupont, E. Golubeva, S. Häkkinen, E. Hunke, M. Jin, M. Karcher, F. Kauker, M. Maltrud, M. A. Morales Maqueda, W. Maslowski, G. Platov, D. Stark, M. Steele, T. Suzuki, J. Wang, and J. Zhang, 2007: Water properties and circulation in Arctic Ocean models. *J. Geophys. Res.*, **112**, C04S03, doi: 10.1029/2006JC003642.

Humpert, M., and A. Raspotnik, 2012: The future of Arctic shipping along the Transpolar Sea Route, *The Arctic Yearbook 2012*, 281–307. [Available online at <http://www.arcticyearbook.com>].

International Boundaries Research Unit (IBRU): The Center for Borders Research ad Durham University, 2016: Maritime jurisdiction and boundaries in the Arctic region. [Available online at <http://www.durham.ac.uk/ibru/resources/arctic>].

IPCC, 2013: *Climate Change 2013: The Physical Science Basis: Contribution of Working Group I to the Fifth Assessment Report of the Intergovernmental Panel on Climate Change*, edited by T. F. Stocker, D. Qin, G.-K. Plattner, M. Tignor, S. K. Allen, J. Boschung, A. Nauels, Y. Xia, V. Bex, and P. M. Midgley, Cambridge University Press.

Jackson, J. M., E. C. Carmack, F. A. McLaughlin, S. E. Allen, and R. G. Ingram, 2010: Identification, characterization, and change of the near-surface temperature maximum in the Canada Basin, 1993–2008. *J. Geophys. Res.*, **115**, C05021, doi:10.1029/2009JC005265.

Jackson, J. M., S. E. Allen, F. A. McLaughlin, R. A. Woodgate, and E. C. Carmack, 2011: Changes to the near-surface waters in the Canada Basin, Arctic Ocean from 1993–2009: A basin in transition. *J. Geophys. Res.*, **116**, C10008, doi:10.1029/2011JC007069.

Jakobsson, M., L. A. Mayer, B. Coakley, J. A. Dowdeswell, S. Forbes, B. Fridman, H. Hodnesdal, R. Noormets, R. Pedersen, M. Rebesco, H.-W. Schenke, Y. Zarayskaya A, D. Accettella, A. Armstrong, R. M. Anderson, P. Bienhoff, A. Camerlenghi, I. Church, M. Edwards, J. V. Gardner, J. K. Hall, B. Hell, O. B. Hestvik, Y. Kristoffersen, C. Marcussen, R. Mohammad, D. Mosher, S. V. Nghiem, M. T. Pedrosa, P. G. Travaglini, and P. Weatherall, 2012: The International Bathymetric Chart of the Arctic Ocean (IBCAO) Version 3.0, *Geophysical Res. Lett.*, doi: 10.1029/2012GL052219.

Jin, M., J. Hutchings, Y. Kawaguchi, and T. Kikuchi, 2012: Ocean mixing with lead-dependent subgrid scale brine rejection parameterization in a climate model. *J. Ocean Univ. China*, **11**, 473–480, doi: 10.1007/s11802-12-2094-4.

Joint World Meteorological Organization-Intergovernmental Oceanographic Commission Technical Commission for Oceanography and Marine Meteorology (JCOMM), cited 2016: World Meteorological Organization (WMO) Publication No. 259 Sea Ice Nomenclature. [Available online at http://www.jcomm.info/index.php?option=com_oe&task=viewDocumentRecord&docID=4438].

Jungclaus, J.H., N. Keenlyside, M. Botzet, H. Haak, J. J. Luo, M. Latif, J. Marotzke, U. Mikolajewicz, and E. Roeckner, 2006: Ocean circulation and tropical variability in the coupled model ECHAM5/MPI-OM. *Journal of climate*, **19**(16), 3952–3972.

Kay, J. E., C. Deser, A. Phillips, A. Mai, C. Hannay, G. Strand, J. M. Arblaster, S. C. Bates, G. Danabasoglu, J. Edwards, M. Holland, P. Kushner, J.-F. Lamarque, D. Lawrence, K. Lindsay, A. Middleton, E. Munoz, R. Neale, K. Oleson, L. Polvani, and M. Vertenstein, 2015: The Community Earth System Model (CESM) Large Ensemble Project. *Bulletin of the American Meteorological Society*, **96**(8), 1333–1349.

Koivurova, T., and E. J. Molenaar, 2009: International Governance and Regulation of the Marine Arctic Overview and Gap Analysis. WWF International Arctic Program, Oslo, Norway, pp 44.

Krishfield, R., J. Toole, A. Proshutinsky, and M.-L. Timmermans, 2008: Automated ice-tethered profilers for seawater observations under pack ice in all seasons. *J. Atmos. Oceanic Technol.*, **25**, 2091–2105.

Kutschale, H. 1961: Long-range sound transmission in the Arctic Ocean. *J. Geophys. Res.*, **66**(7), 2189–2198.

Kuperman, W. A., 2001: Deep Ocean Acoustics. *Encyclopedia of Ocean Sciences*, J. H. Steele, K. K. Turekian, and S. A. Thorpe, Ed., Academic Press, 61–72.

Kwok, R., G. F. Cunningham, H. J. Zwally, and D. Yi, 2007: Ice, Cloud, and land Elevation Satellite (ICESat) over Arctic sea ice: Retrieval of freeboard, *J. Geophys. Res.*, **112**, C12013, doi:10.1029/2006JC003978

Kwok R., and D. A. Rothrock. 2009: Decline in Arctic sea ice thickness from submarine and ICESat records: 1958–2008. *Geophys. Res. Lett.* **36**:L15501

Langen, P. L., and V. A. Alexeev, 2007: Polar amplification as a preferred response in an idealized aquaplanet GCM. *Climate Dynamics*, **29**, 305–317. doi:10.1007/S00382-006-0221-X

Levine, M. D., C. A. Paulson, and J. H. Morison, 1985: Internal waves in the Arctic Ocean: comparison with lower-latitude observations. *J. Phys. Oceanogr.*, **15**, 800–809.

Levine, M. D., C. A. Paulson, and J. H. Morison, 1987: Observations of internal gravity waves under the Arctic pack ice. *J. Phys. Oceanogr.*, **92**, 779–782.

Lecomte, O., T. Fichefet, M. Vancoppenolle, F. Domine, F. Massonnet, P. Mathiot, S. Morin, and P. Y. Barriat, 2013: On the formulation of snow thermal conductivity in large-scale sea ice models. *Journal of Advances in Modeling Earth Systems*, **5**, 542–557. doi:10.1002/jame.20039

Lique, C., and M. Steele, 2013: Seasonal to decadal variability of Arctic Ocean heat content: A model-based analysis and implications for autonomous observing systems, *J. Geophys. Res. Oceans*, **118**, 1673–1695, doi:10.1002/jgrc.20127.

Logerwell, L., 2008: Cruise Report for the 2008 Beaufort Sea Survey. NOAA, U.S. Department of Commerce, National Marine Fisheries Service, Alaska Fisheries Science Center.

Marsh, H. W., and R. H. Mellen, 1963: Underwater sound propagation in the Arctic Ocean, *J. Acous. Soc. Am.*, **35**(4), 552–563.

Maslowski, W., J. Clement Kinney, and J. Jakacki, 2007: Toward prediction of environmental and Arctic change, *Comp. in Sci. & Eng.*, **9**(6), 29–34.

Maslowski, W., J. L. Clement Kinney, M. E. Higgins, and A. Roberts, 2012: Future of Arctic sea ice, *Annual Review of Earth and Planetary Sciences*, **40**, 625–654.

Maslowski, W., 2013: Understanding the Arctic Climate System. *International Innovation*, pp 70–72, February 2013, Research Media, UK, ISSN 2051–8528.

Maslowski, W., J. L. Clement Kinney, D. C. Marble, and J. Jakacki, 2013: Towards eddy-resolving models of the Arctic Ocean. *Ocean modeling in an eddying regime*, *Geophys. Monogr. Ser.*, Vol 177, edited by M. W. Hecht and H. Hasumi, Ameri. Geophys. Union, Washington, D. C. doi: 10.1029/177GM16

Maslowski, W., J. L. Clement Kinney, S. R. Okkonen, R. Osinski, A. F. Roberts, W. Williams, 2014: The large scale ocean circulation and physical processes controlling Pacific-Arctic interaction. *The Pacific Arctic Region*, J. M. Grebmeier and W. Maslowski, Ed., Springer, p. 101–132.

Massonnet, F., T. Fichefet, H. Goosse, C. M. Bitz, G. Philippon-Berthier, M. M. Holland, and P. Y. Barriat, 2012: Constraining projections of summer Arctic sea ice. *The Cryosphere*, **6**(6), 1383–1394.

McGeehan, T., and W. Maslowski, 2011: Impact of shelf-basin freshwater transport on deep convection in the western Labrador Sea, *J. Phys. Ocean.*, **41**, 2187–2210.

McPhee, M., 2008: *Air-Ice-Ocean Interaction: Turbulent Ocean Boundary Layer Exchange Processes*. Springer, 215 pp

Mikhalevsky, P. N., A. N. Gavrillov, and A. B. Baggeroer, 1999: The Transarctic Acoustic Propagation Experiment and climate monitoring in the Arctic. *IEEE J. Oceanic Engineering*, **24**(2), 183–201.

Mikhalevsky, P. N. 2001: Arctic Acoustics. *Encyclopedia of Ocean Sciences*, J. H. Steele, K. K. Turekian, and S. A. Thorpe, Ed., Academic Press, 53–61.

Mills, T., 2012: An evaluation of sea ice deformation and its spatial characteristics from the regional arctic system model. Thesis, Department of Oceanography, Naval Postgraduate School, 196 pp., [Available online at <http://hdl.handle.net/10945/27872>].

Munk, W., 1981: Internal waves and small scale processes. *The Evolution of Physical Oceanography*, B. Warren and C. Wunsch, Ed., Massachusetts Institute of Technology, 264–291.

Munk, W., and C. Wunsch, 1998: Abyssal recipes II: Energetics of tidal and wind mixing. *Deep-Sea Res.*, **45** 1977–2010, doi:10.1016/S0967-0637(98)00070-3.

National Intelligence Council, 2016: Implications for U.S. National Security of Anticipated Climate Change, NIC WP 2016–01. [Available online at https://www.dni.gov/files/documents/Newsroom/Reports%20and%20Pubs/Implications_for_US_National_Security_of_Anticipated_Climate_Change.pdf].

National Research Council, 2012: Seasonal-to-decadal predictions of Arctic sea ice: challenges and strategies. The National Academies Press, Washington, DC, 80 pp.

National Snow and Ice Data Center (NSIDC), cited 2016: State of the Cryosphere. [Available online at http://nsidc.org/cryosphere/sotc/sea_ice.html]

Nelson, M., 2016: Short-range acoustic propagation under Arctic ice cover during ICEX-16. Thesis, Department of Oceanography, Naval Postgraduate School, 55 pp., [Available online at: <http://calhoun.nps.edu/handle/10945/50603>].

Northern Sea Route Information Office (NSRIO), cited 2014: Transit Statistics. [Available online at http://www.arctic-lio.com/nsr_transits].

Nguyen, A. T., D. Menemenlis, and R. Kwok, 2009: Improved modeling of the Arctic halocline with a subgrid-scale brine rejection parameterization. *J. Geophys. Res.*, **114**, C11014, doi:10.1029/2008JC005121.

Nguyen, A. T., R. Kwok, and D. Menemenlis, 2011: Source and pathway of the western Arctic upper halocline in a data-constrained coupled ocean and sea ice model, *J. Phys. Ocean.*, **42**, 802–823.

Office of Naval Research (ONR), cited 2014: Marginal Ice Zone (MIZ) Program. [Available online at <http://www.apl.washington.edu/project/project.php?id=miz>].

Office of the Secretary of Defense (OSD), 2013: Arctic Strategy. [Available online at http://www.defense.gov/pubs.2013_Arctic_Strategy.pdf]

Okkonen, S. R., C. J. Ashjian, R. G. Campbell, W. Maslowski, J. L. Clement-Kinney, and R. Potter, 2009: Intrusion of warm Bering/Chukchi waters onto the shelf in the western Beaufort Sea, *J. Geophys. Res.*, **114**, C00Q11, doi:10.1029/

Osinski, R., W. Maslowski, A. Roberts, J. Clement Kinney, and A. Craig, 2014: On the sensitivity of sea ice states to variable parameter space in the Regional Arctic System Model., *Ann. Glaciol.*, submitted.

Ostreng, W., 2012: Shipping and resources in the Arctic Ocean: a hemispheric perspective, *The Arctic Yearbook 2012.*, 247–280. [Available online at <http://www.arcticyearbook.com>].

Overeem, I., R. S. Anderson, C. W. Wobus, G. D. Clow, F. E. Urban, and N. Matell, 2011: Sea ice loss enhances wave action at the Arctic coast, *Geophys. Res. Lett.*, **38**, L17503, doi:10.1029/2011GL048681.

Padman, L., and T. M. Dillon, 1987: Vertical heat fluxes through the Beaufort Sea thermohaline staircase. *J. Geophys. Res.*, **92**(C10), 10799-10806.

Pearson, A., 2016: An analysis of the Beaufort Sea thermohaline structure and variability, and its effects on acoustic propagation. Thesis, Department of Oceanography, Naval Postgraduate School, 101 pp., [Available online at: <http://hdl.handle.net/10945/49364>].

Perovich, D. K., B. Light, H. Eicken, K. F. Jones, K. Runciman, and S. V. Nghiem, 2007: Increasing solar heating of the Arctic Ocean and adjacent seas, 1979–2005: Attribution and role in the ice-albedo feedback, *Geophys. Res. Lett.*, **34**, L19505, doi:10.1029/2007GL031480.

Perovich, D. K., J. A. Richter-Menge, K. F. Jones, and B. Light, 2008: Sunlight, water, and ice: Extreme Arctic sea ice melt during the summer of 2007. *Geophys. Res. Lett.*, **35**, doi:Artn L11501 Doi 10.1029/2008gl034007

Perovich, D., W. Meier, M. Tschudi, S. Farrel, S. Gerland, and S. Hendricks, 2015: Sea Ice. Accessed 15 September 2016. [Available online at http://www.arctic.noaa.gov/reportcard/sea_ice.html].

Pickart, R. S., T. J. Weingartner, L. J. Pratt, S. Zimmermann, and D. J. Torres, 2005: Flow of winter-transformed Pacific water into the Western Arctic. *Deep Sea Res. Part II*, **52**(24), 3175–3198.

Pisareva, M. N., R. S. Pickart, M. A. Spall, C. Nobre, D. J. Torres, G. W. K. Moore, and T. E. Whitledge, 2015: Flow of Pacific water in the western Chukchi Sea: Results from the 2009 RUSALCA expedition. *Deep-Sea Res. Pt. I*, **105**, 53–73.

Proshutinsky, A., R. Krishfield, M.-L. Timmermans, J. Toole, E. Carmack, F. McLaughlin, W. J. Williams, S. Zimmermann, M. Itoh, and K. Shimada, 2009: Beaufort Gyre freshwater reservoir: State and variability from observations. *J. Geophys. Res.*, **114**(C1), doi:10.1029/2008JC005104.

Rabe, B., M. Karcher, F. Kauker, U. Schauer, J. M. Toole, R. A. Krishfield, S. Pisarev, T. Kikuchi, and J. Su, 2014: Arctic Ocean basin liquid freshwater storage trend 1992–2012, *Geophys. Res. Lett.*, **41**, 961–968, doi:10.1002/2013GL058121.

Rainville, L., and R. A. Woodgate, 2009: Observations of internal wave generation in the seasonally ice-free Arctic, *Geophys. Res. Lett.*, **36**, L23604, doi:10.1029/2009GL041291.

Rajan, S. D. 1993: Determination of compressional wave and shear wave speed profiles in sea ice by crosshole tomography theory and experiment. *J. Acous. Soc. Am.*, **93**(2), 721–738.

Roberts, A. and Coauthors, 2010: A science plan for regional Arctic system modeling. International Arctic Research Center Tech. paper 10–0001, 47 pp. [Available online at www.iarc.uaf.edu/publications/reports/IARCTP10-0001.pdf].

Roberts, A., A. P. Craig, W. Maslowski, R. Osinski, A. DuVivier, M. Hughes, B. Nijssen, J. Cassano, and M. Brunke, 2015: Simulating transient ice-ocean Ekman transport in the Regional Arctic System Model and Community Earth System Model, *Ann. Glaciol.*, **56**(69), 211–228.

Roberts, A., et al. 2016: In Prep.

Rudels, B., L. G. Anderson, and E. P. Jones, 1996: Formation and evolution of the surface mixed layer and halocline of the Arctic Ocean. *J. Geophys. Res.*, **101**, C4, 8807–8821.

Rudels, B., 2001: Arctic Basin Circulation. *Encyclopedia of Ocean Sciences*, J. H. Steele, K. K. Turekian, and S. A. Thorpe, Ed., Academic Press, 177–187.

Rudels, B., E. Jones, U. Schauer, and P Eriksson, 2004: Atlantic sources of the Arctic Ocean surface and halocline waters, *Polar Res.*, **23**, 181–203.

Rudels, B., 2012: Arctic Ocean circulation and variability – advection and external forcing encounter constraints and local processes, *Ocean Sci.*, **8**, 261–286.

Schneider, N., and P. Muller, 1990: The meridional and seasonal structures of the mixed-layer depths and its diurnal amplitude observed during the Hawaii-to-Tahiti Shuttle experiment. *J. Phys. Oceanogr.*, **20**, 1395–1404.

Schweiger, A., R. Lindsay, J. Zhang, M. Steele, H. Stern, and R. Kwok, 2011: Uncertainty in modeled Arctic sea ice volume. *J. Geophys. Res.*, **116**, C00D06, doi:10.1029/2011JC007084.

Screen, J. A., and I. Simmonds, 2010: The central role of diminishing sea ice in recent Arctic temperature amplification. *Nature*, **464**, 1334–1337. doi:Doi 10.1038/Nature09051

Shimada, K., E. Carmack, K. Hatekeyama, and T. Takizawa, 2001: Varieties of shallow temperature maximum waters in the western Canada Basin of the Arctic Ocean, *Geophys. Res. Lett.*, **28**, 2441–2444.

Showstack, R., 2013: Pentagon Strategy Recognizes Need for Increased Research in the Arctic, *Eos*, **94**, 485–486.

Sigler, M., 2009: Climate Change and Arctic Fisheries. *3rd Symposium on the Impact of an Ice-Diminishing Arctic on Naval and Maritime Operations*, Annapolis, MD, U. S. National Ice Center and the U. S. Arctic Research Commission, 1–28.

Simmonds, I., and I. Rudeva, 2012: The great Arctic cyclone of August 2012, *Geophys. Res. Lett.*, **39**, L23709, doi:10.1029/2012GL054259.

Spall, M. A., R. S. Pickart, P. S. Fratantoni, and A. J. Plueddemann, 2008: Western Arctic shelfbreak eddies: Formation and transport. *J. Phys. Ocean.*, **38**(8), 1644–1668.

Steele, M., and T. Boyd, 1998: Retreat of the cold halocline layer in the Arctic Ocean, *J. Geophys. Res.*, **103**, 10,419-10,435.

Steele, M., R. Morley, and W. Ermold, 2001: PHC: a global ocean hydrography with a high-quality Arctic Ocean. *J. Climate*, **14**, 2079–2087, doi: 10.1175/1520-0442(2001)014<2079:PAGOHW>2.0.CO;2.

Steele, M., J. Morison, W. Ermold, I. Rigor, M. Ortmeyer, and K. Shimada, 2004: Circulation of summer Pacific halocline waters in the Arctic Ocean, *J. Geophys. Res.*, **109**, C02027, doi:10.1029/2003JC002009.

Steele, M., J. Zhang, and W. Ermold, 2010: Mechanisms of summertime upper Arctic Ocean warming and the effect on sea ice melt. *J. Geophys. Res.*, **115**(C11), doi: 10.1029/2009JC005849

Steele, M., W. Ermold, and J. Zhang, 2011: Modeling the formation and fate of the near- surface temperature maximum in the Canadian Basin of the Arctic Ocean, *J. Geophys. Res.*, **116**, C11015, doi:10.1029/2010JC006803.

Stevens, B., M. Giorgetta, M. Esch, T. Mauritsen, T. Crueger, S. Rast, M. Salzmann, H. Schmidt, J. Bader, K. Block, R. Brokopf, I. Fast, S. Kinne, L. Kornblueh, U. Lohmann, R. Pincus, T. Reichler, E. Roeckner, 2013: Atmospheric component of the MPI-M Earth System Model: ECHAM6. *Journal of Advances in Modeling Earth Systems*, **5**, 146–172.

Stroeve, J. C., M. C. Serreze., M. M. Holland, J. E. Kay, J. Maslanik, and A. P Barrett, 2012: The Arctic's rapidly shrinking sea ice cover: a research synthesis, *Clim Change*. DOI 10.1007/s10584-011-0101-1

Talley, D. L., G. L. Pickard, W. J. Emery, and J. H. Swift, J. H., 2011: *Descriptive Physical Oceanography: An Introduction*. Elsevier, chapters 1 and 8.

Task Force Climate Change /Chief of Naval Operations, 2014: U.S. Navy Arctic Roadmap 2014 - 2030, 43 pp.

Taylor, K.E., 2001: Summarizing multiple aspects of model performance in a single diagram. *J. Geophys. Res.*, **106**(D7), 7183–7192.

Taylor, K. E., R. J. Stouffer, and G. A. Meehl, 2012: An overview of CMIP5 and the experiment design. *Bulletin of the American Meteorological Society*, **93**(4), 485–498.

Thomson, R. E., and I. V. Fine, 2003: Estimating mixed layer depth from oceanic profile data, *J. Atmos Oceanic Technol.*, **20**, 319–329.

Timmermans, M.-L., J. Toole, R. Krishfield, and P. Winsor, 2008: Ice-tethered profiler observations of the double-diffusive staircase in the Canada Basin thermocline, *J. Geophys. Res.*, **113**, C00A02, doi:10.1029/2008JC004829.

Timmermans, M.-L., S. Cole, and J. Toole, 2012: Horizontal density structure and restratification of the Arctic Ocean surface layer, *J. Phys. Ocean.*, **42**, 659–668.

Timmermans, M.-L., A. Proshutinsky, E. Golubeva, J. M. Jackson, R. Krishfield, M. McCall, G. Platov, J. Toole, W. Williams, T. Kikuchi, and S. Nishino, 2014: Mechanisms of Pacific Summer Water variability in the Arctic's Central Canada Basin, *J. Geophys. Res. Oceans*, **119**, doi:10.1002/2014JC010273.

Toole, J. M., M.-L. Timmermans, D. K. Perovich, R. A. Krishfield, A. Proshutinsky, and J. A. Richter-Menge, 2010: Influences of the ocean surface mixed layer and thermohaline stratification on Arctic Sea ice in the central Canada Basin, *J. Geophys. Res.*, **115**, C10018, doi:10.1029/2009JC005660.

Treat, C. C., and S. Frolking, 2013: Carbon Storage: A permafrost carbon bomb? *Nature Climate Change*, **3**, 865–867. doi:10.1038/nclimate2010

Tseng, H. R., 2010: Toward quantifying the impact of atmospheric forcing on Arctic sea ice variability using the NPS 1/12 degree pan-Arctic coupled ice-ocean model. Thesis, Department of Oceanography, Naval Postgraduate School, 196 pp., [Available online at: <http://hdl.handle.net/10945/5416>].

Turner, J., E. A. Rasmussen, and A. M. Carleton, 2003: Introduction. *Polar Lows - Mesoscale Weather Systems in the Polar Regions*, E. A. Rasmussen and J. Turner, Eds., Cambridge University Press, 1–51.

United Nations Office of Legal Affairs, cited 2016: United Nations Convention on the Law of the Sea of 10 December 1982 Overview and full text. [Available online at http://www.un.org/depts/los/convention_agreements/convention_overview_convention.htm].

United States Coast Guard, cited 2013: United States Coast Guard Arctic strategy [Available online at http://www.uscg.mil/seniorleadership/DOCS/CG_Arctic_Strategy.pdf].

United States Geological Survey (USGS), 2008: Circum-Arctic Resource Appraisal: Estimates of Undiscovered Oil and Gas North of the Arctic Circle. USGS Fact Sheet 2008-3049, 4 pp.

Wadhams, P., 2000: *Ice in the Ocean*. Gordon and Breach Science Publishers, 351 pp.

Wadhams, P., and N. R. Davis, 2000: Further evidence of ice thinning in the Arctic Ocean. *Geophysical Research Letters*, **27**, 3973–3975.

Watanabe, E. and H. Hasumi, 2009: Pacific water transport in the western Arctic Ocean simulated by an eddy-resolving coupled sea ice-ocean model. *J. Phys. Ocean.*, **39**(9), 2194–2211.

Wolfson, M. A., and F. D. Tappert, 2000: Study of horizontal multipath and ray chaos due to ocean mesoscale structure. *J. Acoust. Soc. Am.*, **107**(1), 154–162.

White House, 2010: *National Security Strategy*. [Available online at http://www.whitehouse.gov/sites/default/files/rss_viewer/national_security_strategy.pdf].

White House, 2013: *National Strategy for the Arctic Region*. [Available online at http://www.whitehouse.gov/sites/default/files/docs/nat_arctic_strategy.pdf].

White House, 2014: *Implementation Plan for the National Strategy for the Arctic Region*. [Available online at https://www.whitehouse.gov/sites/default/files/docs/implementation_plan_for_the_national_strategy_for_the_arctic_region_-fi....pdf].

White House, 2015: *National Security Strategy*. [Available online at <http://nssarchive.us/wp-content/uploads/2015/02/2015.pdf>].

Wijesekera, R. W., and M. C. Gregg, 1996: Surface layer response to weak winds, westerly bursts, and rain squalls in the western Pacific warm pool, *J. Geophys. Res.*, **101**, 977–997.

Woods Hole Oceanographic Institution (WHOI), cited 2014: Ice-tethered profiler. [Available online at <http://www.whoi.edu/itp>]

WHOI, cited 2014: Arctic Ocean Circulation. [Available online at <http://www.whoi.edu/main/topic/arctic-ocean-circulation>]

Woodgate, R., K. Aagaard, J. H. Swift, K. K. Falkner, and W. M. Smethie Jr., 2005: Pacific ventilation of the Arctic Ocean's lower halocline by upwelling and diapycnal mixing over the continental margin, *Geophys. Res. Lett.*, **32**, L18609, doi:10.1029/2005/GL023999.

Yew, C. H., and X. Weng, 1987: A study of reflection and refraction of waves at the interface of water and porous sea ice. *J. Acoust. Soc. Am.*, **70**, 841–851.

THIS PAGE INTENTIONALLY LEFT BLANK

INITIAL DISTRIBUTION LIST

1. Defense Technical Information Center
Ft. Belvoir, Virginia
2. Dudley Knox Library
Naval Postgraduate School
Monterey, California